

UNCLASSIFIED

AD

240 709

Reproduced

Armed Services Technical Information Agency

ARLINGTON HALL STATION; ARLINGTON 12 VIRGINIA

NOTICE: WHEN GOVERNMENT OR OTHER DRAWINGS, SPECIFICATIONS OR OTHER DATA ARE USED FOR ANY PURPOSE OTHER THAN IN CONNECTION WITH A DEFINITELY RELATED GOVERNMENT PROCUREMENT OPERATION, THE U. S. GOVERNMENT THEREBY INCURS NO RESPONSIBILITY, NOR ANY OBLIGATION WHATSOEVER; AND THE FACT THAT THE GOVERNMENT MAY HAVE FORMULATED, FURNISHED, OR IN ANY WAY SUPPLIED THE SAID DRAWINGS, SPECIFICATIONS, OR OTHER DATA IS NOT TO BE REGARDED BY IMPLICATION OR OTHERWISE AS IN ANY MANNER LICENSING THE HOLDER OR ANY OTHER PERSON OR CORPORATION, OR CONVEYING ANY RIGHTS OR PERMISSION TO MANUFACTURE, USE OR SELL ANY PATENTED INVENTION THAT MAY IN ANY WAY BE RELATED THERETO.

UNCLASSIFIED

CURTISS



WRIGHT

NOX

FILE COPY

Return to

ASTIA

ARLINGTON HALL STATION
ARLINGTON 12, VIRGINIA

Attn: TISS

CURTISS-WRIGHT CORPORATION
RESEARCH DIVISION
CLIFTON, NEW JERSEY, U.S.A.
QUEHANNA, PA., U.S.A.

Final Report

CWR 700-10

ANALYTICAL AND
EXPERIMENTAL INVESTIGATION
of
COMPACT CHARGE IONIZATION

June 1, 1960

ARPA Order Number 5-58

Task Number 094-~~58~~ 347

Contract Number NOnr 2886 (00)



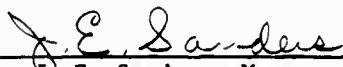
CURTISS-WRIGHT CORPORATION
RESEARCH DIVISION
QUEHANNA, PENNSYLVANIA

ANALYTICAL AND
EXPERIMENTAL INVESTIGATION
of
COMPACT CHARGE IONIZATION

E. N. Petrick, G. K. Hüsman, and
H. W. Szymanowski

The authors are indebted to Dr. E. Mueller, Director, Field Emission Laboratory, Pennsylvania State University, who assisted in the capacity of Principal Scientific Consultant. Credit also is due to Dr. C. Burnett of the Pennsylvania State University and to Messrs. R. Hughes and W. Aker of the Curtiss-Wright Research Division for their assistance in the preparation of this report.

Approved for release by



J. E. Sanders, Manager
Research & Product Development Department

ABSTRACT

The investigations described in this report were conducted at the Quehanna Laboratories, Research Division, Curtiss-Wright Corporation, under ARPA sponsorship. Project officers included Cmdr. F. Hemler, Cmdr. W. L. Miller, and Mr. J. Patton of the Power Branch, Office of Naval Research, which is under the direction of Mr. F. Wiesner. The program at the Quehanna Laboratories was supervised by Dr. E. N. Petrick. The other principal investigators included Dr. O. K. Husmann, applied physicist, and Mr. H. W. Szymanowski, electro-mechanical engineer. Other contributors to the program are cited in the main text corresponding to the area of their principal effort.

The objective of the program was primarily to investigate charge exchange (surface) ionization. Diffusion flow rate tests with inert gases and ionization tests with cesium were conducted using emitters of sintered porous tungsten, electro-formed molybdenum screen, and micro-perforated platinum plate. Excellent correlation was demonstrated between measured ion current and the predicted value based on diffusion data. The effect of surface diffusion flow was shown to be negligible.

Cesium corrosion tests demonstrated the high-temperature long-term suitability of various materials, including tungsten, molybdenum, and aluminum oxide. In regard to fabrication of the ion source, a promising technique of brazing the sintered porous tungsten emitters into a molybdenum holder was developed.

The generation of cesium within the fuel supply system was investigated in order to reduce fuel storage and handling problems. A cesium recovery of 89% of theoretical was measured.

Data are included on the various phases of the investigation described above, and specific recommendations are presented.

C O N T E N T S

ii	ABSTRACT
1	I. INTRODUCTION
3	II. THEORETICAL CONSIDERATIONS
4	A. The Charge Exchange Method
31	B. The RF Ion Source
33	C. The Plasma Arc Source
39	III. TYPES OF CONTACT EMITTERS
40	A. Porous Sintered Tungsten
40	B. Mechanically Perforated Platinum Screen
42	C. Electro-Formed Molybdenum Screen
44	IV. DIFFUSION EXPERIMENTS
77	V. EXPERIMENTAL EVALUATION OF VARIOUS CONTACT EMITTERS
78	A. Ion Gun
85	B. Emitter Evaluation
93	C. Mass Spectrometer
99	VI. BONDING THE EMITTER
100	A. Mechanical Joints
103	B. Brazing
115	C. Welding
115	D. Sintering In Place
118	VII. CORROSION OF MATERIALS BY CESIUM
119	A. Introduction
113	B. Materials
120	C. Test Procedure
124	D. Results Of First And Second Test Series
135	E. Third Test Series
145	F. Conclusions From Corrosion Tests
147	VIII. CESIUM GENERATION IN SITU
156	IX. THE RF ION SOURCE APPARATUS
160	X. THE PLASMA ARC SOURCE, PROPOSED EXPERIMENTS
161	A. Diagnostics
164	B. Ion Extraction
167	XI. RESULTS AND RECOMMENDATIONS
170	REFERENCES

Figures

Page

6	II-1. Efficiency Versus Temperature for Various Ion Propulsion Fuels
7	II-2. Ionization Efficiency of Cesium
8	II-3. Ionization Efficiency of Rubidium
9	II-4. Ionization Efficiency of Potassium
10	II-5. Ionization Efficiency of Sodium
11	II-6. Ionization Efficiency of Lithium
14	II-7. Lifetime on Heated Tungsten Surface
15	II-8. Lifetime on Rb Atom on Tungsten for Various Degrees of Contamination
17	II-9. Saturation Vapor Pressure of Alkali Metals
19	II-10. Mean Free Path
21	II-11. Flow Rate as a Function of Pore Size and Emitter Temperature
22	II-12. Heat Loss by Radiation to Space as a Function of Emitter Temperature and Emissivity, Neglecting Solar Radiation
24	II-13. Effect of Electrode Spacing for Plane Electrodes with Cesium Ions
25	II-14. Effect of Fuel Mass on Current Density
27	II-15. Current-Field Characteristics for Tungsten Covered with K and Cs
29	II-16. Radial Potential Drop in a Cesium Ion Beam
30	II-17. Longitudinal Potential Drop in a Cesium Ion Beam
32	II-18. Breakdown in RF Field with Electrodes Oxidized
34	II-19. Ion Condenser System
35	II-20. Effect of Ion Condenser
36	II-21. Effect of Magnetic Field (Transverse)
41	III-1. Platinum Emitter (Drawing)
43	III-2. Photograph of Molybdenum Screen
46	IV-1. Diffusion Flow Rate Measuring Apparatus
48	IV-2. Cross-Section of F-2 Porous Emitter
49	IV-3. Cross-Section of F-2 Porous Emitter - Parallel to Surface
50	IV-4. Cross-Section of P-1 Porous Emitter
52	IV-5. Proportional Frequency of Void Sizes
54	IV-6. Theoretical Porous Plate Model with Uniform Spherical Grains
55	IV-7. Mean Pore Radius Versus Grain Diameter for Theoretical Model with Uniform Spherical Grain
57	IV-8. Theoretical Flow in Amps per cm^2 in Model Plate as a Function of Pore Radius
58	IV-9. Theoretical Flow in Amps per cm^2 in Model Plate as a Function of Pore Volume
59	IV-10. Molecular Flow Rate through a Bundle of Capillaries as a Function of Molecular Weight

Figures

Page

60	IV-11. Molecular Flow Rate through a Bundle of Capillaries as a Function of Pore Radius
62	IV-12. Experimental and Theoretical Diffusion Flow for Platinum Screen
63	IV-13. Platinum Screen Diffusion Flow as a Function of Screen Temperature
65	IV-14. Flow Rate for Molybdenum Screen
67	IV-15. Experimental and Theoretical Flow Data for P-2 Tungsten Plate
68	IV-16. Flow Data for F-1 Porous Tungsten Plate Showing Aging Effect
69	IV-17. Experimental and Theoretical Flow Data for F-1 Porous Plate
70	IV-18. Helium Flow Rate through Porous Tungsten Emitters as a Function of Plate Temperature (Molecular Flow)
73	IV-19. Experimental and Theoretical Flow Data for C-1 Porous Plate
74	IV-20. Transmission Coefficient Versus Porous Volume for Barium through Porous Plate
79	V-1. Ion Gun
80	V-2. RF Heating of the P-1 Porous Tungsten Emitter
82	V-3. Wiring Diagram for Ion Gun
84	V-4. Ion Gun Current with Residual Gases
86	V-5. Theoretical Dependence of Ion Current on Plate Temperature
87	V-6. Comparison of Measured Ion Currents with Diffusion Flow Rates
88	V-7. Measured Ion Current Density for Various Emitters
90	V-8. Dependence of Ion Current on Fuel Vapor Pressure (Temperature)
94	V-9. Sketch of Mass Spectrometer
95	V-10. Photograph of Mass Spectrometer
97	V-11. Field Strength in Mass Spectrometer
101	VI-1. "L" Cathode
102	VI-2. Powder Seal
104	VI-3. Nickel Brazed Porous Tungsten Plate
106	VI-4. Typical Brazing Set-Up
107	VI-5. First Platinum Braze Configuration
108	VI-6. Photomicrograph of Brazed Emitter Before Test
110	VI-7. Emitter F-1 After 30-Hour Test
112	VI-8. Photograph of Platinum-Bonded Emitter F-1 After Test
114	VI-9. RF Heating Assembly for Joining Ceramic Tube to Porous Tungsten Plate
116	VI-10. Vacuum Arc Weld Apparatus
117	VI-11. Porous Tungsten Plate Sintered Directly into Tungsten Tube

Figures

Page

122	VII-1. Metallic Samples in Glass Vacuum Container
123	VII-2. Test Set-Up for Loading Cesium into Corrosion Containers
129	VII-3. Photomicrograph of Aluminum Sample Exposed to Cesium Vapor at 575°K for 100 hours
130	VII-4. Molybdenum Before and After Second Cesium Corrosion Test
131	VII-5. Niobium Before and After Second Cesium Corrosion Test
132	VII-6. Inconel X Before and After Second Cesium Corrosion Test
133	VII-7. Stainless Steel 308 Before and After Second Corrosion Test
134	VII-8. Iridium Before and After Second Corrosion Test
138	VII-9. Copper 1 Before and After Third Cesium Corrosion Test
139	VII-10. Copper 2 After Third Cesium Corrosion Test
140	VII-11. Platinum 2 Before and After Third Cesium Corrosion Test
141	VII-12. Tungsten 2 Before and After Third Cesium Corrosion Test
142	VII-13. Molybdenum 2 Before and After Third Cesium Corrosion Test
143	VII-14. Nickel 2 Before and After Third Cesium Corrosion Test
144	VII-15. Stainless Steel 410-2 After Third Cesium Corrosion Test
153	VIII-1. Vacuum Chamber for Cesium Generation Experiments
158	IX-1. RF Hydrogen Ion Source in the Manner of Moak, et al.
159	IX-2. RF Ion Source
165	X-1. Magnetically Constricted Plasma-Arc

TABLES

4	II-A	Ionization Potential Of Alkali Metals
5	II-B	Work Function And Melting Point Of Emitter Materials
51	IV-A	Pore Size Count, F-2 Plate
53	IV-B	Mean Pore Diameter, F-2 Plate
56	IV-C	Some Gas Properties
56	IV-D	Platinum Screen Diffusion Results
61	IV-E	Clausing Factor
61	IV-F	Molybdenum Screen Flow Tests
64	IV-G	Flow Test Of F-2 Tungsten Plates
66	IV-H	Flow Data For F-1 Porous Plate
72	IV-I	Flow Data For C-1 Porous Tungsten Plate
75	IV-J	Unitized Diffusion Flow Results
126	VII-A	Effect Of A Cesium Atmosphere On Various Metals
127	VII-B	Effect Of Cesium Atmosphere On Various Non-Metallic Materials
128	VII-C	Second Cesium Corrosion Test With Metals
136	VII-D	Results Of Third Cesium Corrosion Test
151	VIII-A	Physical Properties Of Reactants And Products Considered For Cesium Generation Study
152	VIII-B	Reactants And Products For Cesium Chloride-Calcium Reaction
155	VIII-C	The Colors Of Cesium Oxides

I. INTRODUCTION

The objective of the contract work described herein was to investigate experimentally and optimize a compact ion emitter in order to provide maximum beam current per unit area. The principal investigation involved the use of cesium ionized by the charge exchange (contact) method, with additional limited analytical studies (for comparison purposes) of the RF and plasma-arc methods.

During the course of the experimental work, there were some changes in emphasis as compared to the statement of work presented in the original proposal of Ref. 1. The changes were necessary in order to solve several additional problems to satisfy the contract objective. The additional problems included, for example, cesium corrosion studies, bonding techniques, and cesium generation techniques, none of which were originally proposed.

It should be noted that a useful ion emitter must provide (a) an acceptable efficiency and (b) reliability and long life. Based on those requirements, the program encompassed the following analytical and experimental studies:

(a) For Maximum Efficiency:

- 1) Analytical studies of fuel flow rates, neutral and ion lifetime, ionization efficiency, and overall emitter performance.
- 2) Diffusion experiments to establish the flow regime through the emitter.
- 3) Development of a bonding technique (emitter attachment to vapor source) to eliminate by-pass flow, i.e., fuel leakage. Techniques investigated included powder seal, metallized ceramic joint, arc weld, braze, and sintering in place.
- 4) Tests of various emitters for ionization efficiency, including sintered tungsten plates (40% to 80% density), molybdenum screen (0.003 in. holes), and platinum screen (0.0004 in. holes). Ionization tests were conducted with an ion gun; a mass spectrometer was designed and constructed for precise tests but could not be put into operation before completion of the contract period.

- 5) Comparison with other ionization techniques, including studies of a plasma-seeding method, and of an RF method.

(b) For Reliability and Long Life:

- 1) Corrosion tests to establish the materials least subject to attack by cesium, including emitter materials (tungsten, molybdenum, platinum), structural materials (nickel, stainless steel), electrical conductors (copper), and electrical insulators (aluminum oxide).
- 2) Elimination of fuel handling problems. Test of cesium generation in situ by reduction of a storable cesium salt, thereby eliminating liquid cesium storage in sealed vacuum ampules.

A description of and the results of each of the above phases of the investigation are given in the introduction to each section of the present report. In addition, an overall summary is presented in Section XI, page 167. Specific recommendations for continued experimentation are presented therein.

II. THEORETICAL CONSIDERATIONS

This section is devoted to analytical studies pertaining to techniques of ionization, including the charge exchange, RF, and plasma arc methods. Such factors as fuel flow rates, neutral and ion lifetime, ionization efficiency, and overall emitter performance are discussed.

Dr. O. K. Husmann supervised the studies concerned with charge exchange and RF ionization, assisted by Mr. J. Ross. Dr. C. Burnett prepared the portion dealing with the plasma arc.

II. THEORETICAL CONSIDERATIONS

The principal emphasis in this investigation is on the charge exchange (contact) method of producing ions, by passing an alkali metal vapor through a porous or screen emitter. Other techniques considered include the RF source and the plasma arc source. Each of the methods is described in more detail below.

A. The Charge Exchange Method

In this technique an emitter material with high work function ϕ removes an electron from the alkali atom, which has an ionization potential lower than ϕ . The charge exchange method, under certain conditions which will be discussed later, offers the advantages of a high ionization efficiency when compared with other ionizing methods, and of a relatively low ion velocity distribution.

Ionization efficiency has been discussed recently by Eucken (Ref. 2), Zemel (Ref. 3), and Datz and Taylor (Ref. 4). Previous papers include those of Killian (Ref. 5), Taylor and Langmuir (Ref. 6), Copley and Phipps (Ref. 7), Keuk and Loeb (Ref. 8), and Taylor and Langmuir (Ref. 9). Development of the alkali-ion source from the Kunsman type to the porous plate has been reported by Nordmeyer (Ref. 10) and, in particular, by Koch (Ref. 11). A high ionization efficiency as a principal criterion for ion sources in space travel is discussed by Stuhlinger (Ref. 12), Willinsky and Orr (Ref. 13), Langmuir (Ref. 14), Boden (Ref. 15), and Forrester and Speiser (Ref. 16).

The charge exchange method of ionization is efficient with alkali metals because of their low ionization potentials, as given in TABLE II-A.

TABLE II-A. IONIZATION POTENTIAL OF ALKALI METALS

Li	5.390 volts
Na	5.138
K	4.339
Rb	4.176
Cs	3.893

The ionization efficiency is given by the Saha equation:

$$n_i / (n_i + n_a) = \left\{ 1 + 2 \exp [-(\phi - I) e / kT] \right\}^{-1} \quad (\text{Eq. II-1})$$

where

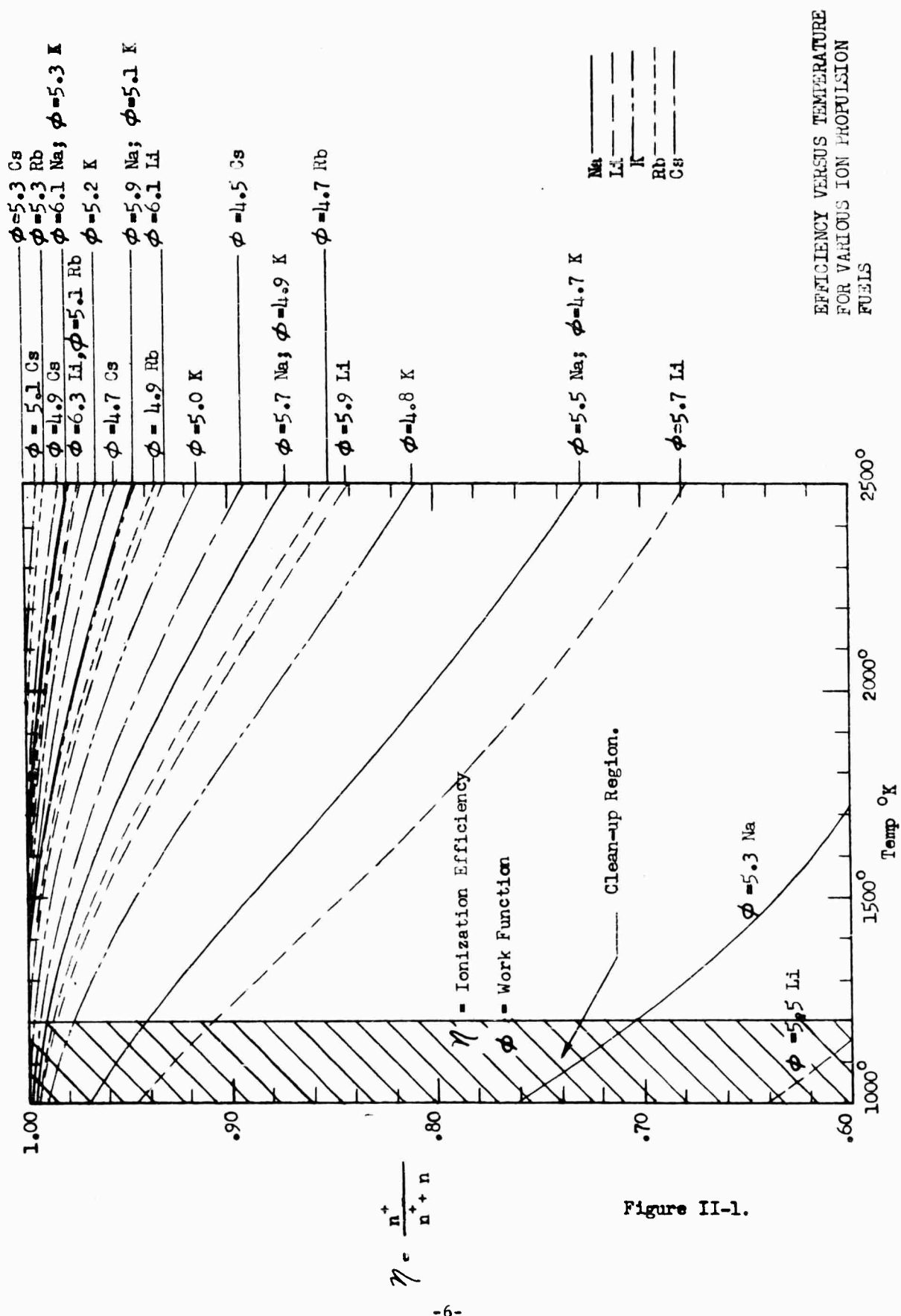
n_i = number of ions
 n_a = number of neutrals
 e = $(1.602) \cdot 10^{-19}$ coul
 ϕ = work function, electron volts
 I = ionization potential, volts
 k = $(1.38) \cdot 10^{-16}$ erg/grad
 T = deg. Kelvin

Figure II-1 presents the ionization efficiency for all the alkali metals as a function of temperature, with work function as the parameter. The curves indicate that the ionization efficiency depends both on the work function and on the ionization potential, and increases as the difference between the two values increases. A work function improvement of 0.1 volt increases the ionization efficiency considerably, as can be noted. Increasing the temperature reduces the ionization efficiency, and the efficiency remains between 99% and 100% efficiency over a wide temperature range only when the difference between work function and the ionization potential is large. The ionization process starts at approximately 1200°K, when the exchange surface starts to clean up by evaporation of low work function alkali films on the emitter surface. Even potassium exhibits high ionization efficiency at reasonable work functions at a temperature of 2000°K. The higher ionization efficiencies at high temperatures for sodium and lithium can be maintained only with high work function materials. Figures II-2 through II-6 illustrate that the work function must be high to maintain a given ionization efficiency as the temperature is raised.

The charge-exchange material is evaluated on the basis of two factors: work function and melting point. Materials which suit this requirement for alkali metal ionization are tungsten, molybdenum, tantalum, niobium, rhenium, and platinum, as illustrated in TABLE II-B.

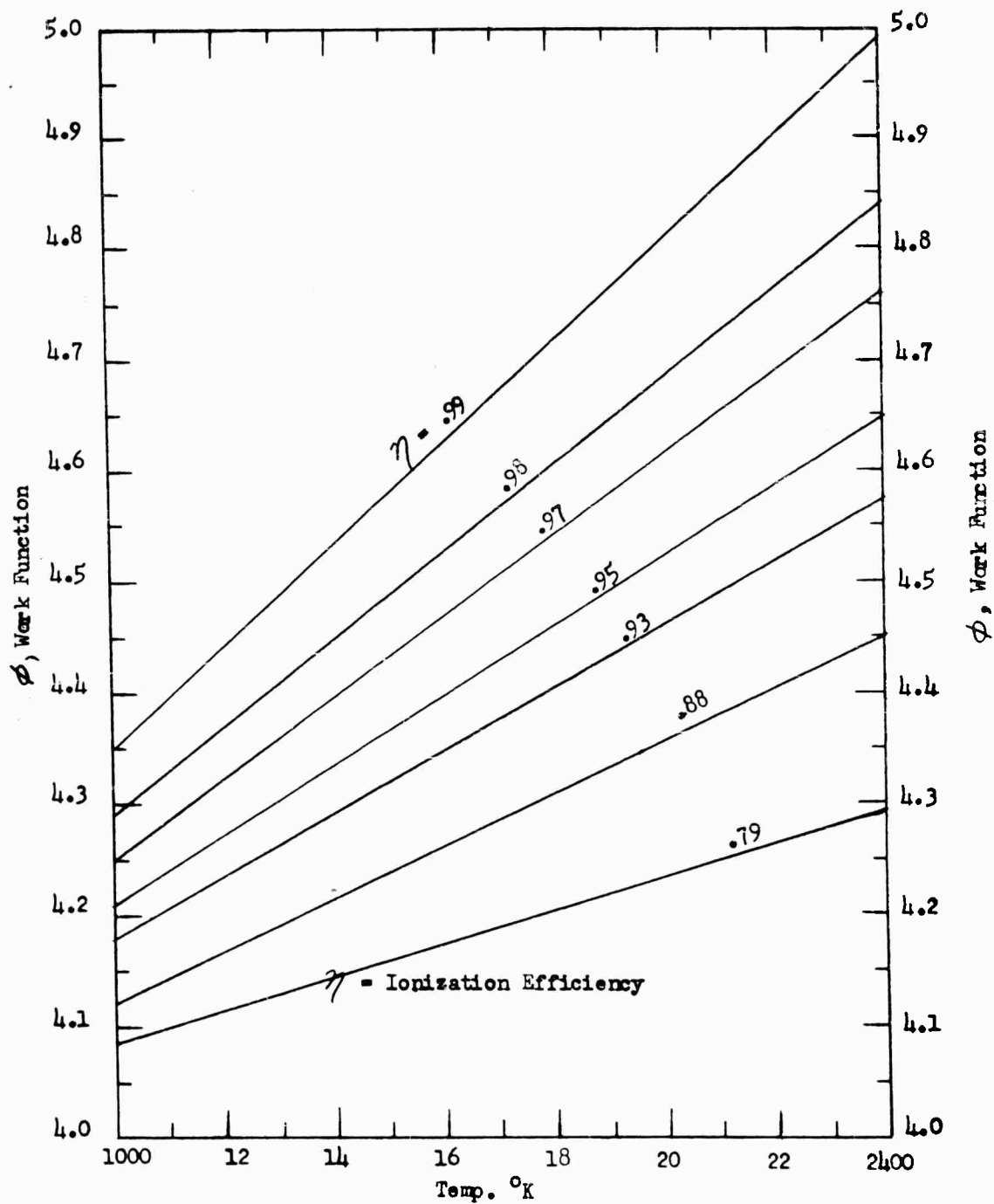
TABLE II-B. WORK FUNCTION AND MELTING POINT OF EMITTER MATERIALS

<u>Material</u>	<u>Electron Work Function</u>	<u>Melting Point</u>
W	4.54 electron volts	3380°C
Mo	4.24	2622
Ta	4.13	2996
Nb	3.99	2410
Pt	5.36 and 6.37	1773
Re	4.97	3172
W Oxide	6.25	3380
Pt Oxide	6.55	1773



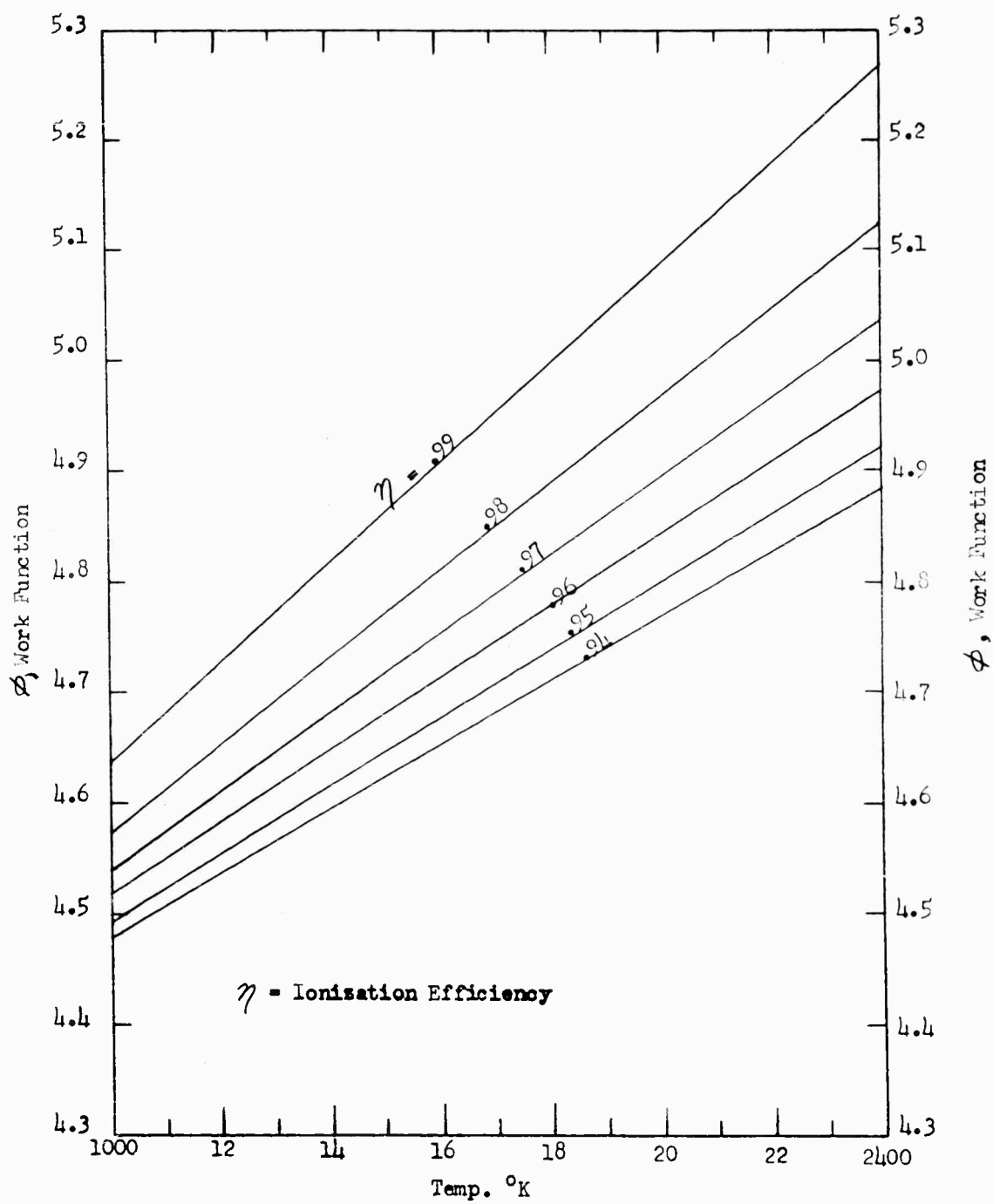
EFFICIENCY VERSUS TEMPERATURE
FOR VARIOUS ION PROPULSION
FUELS

Figure II-1.



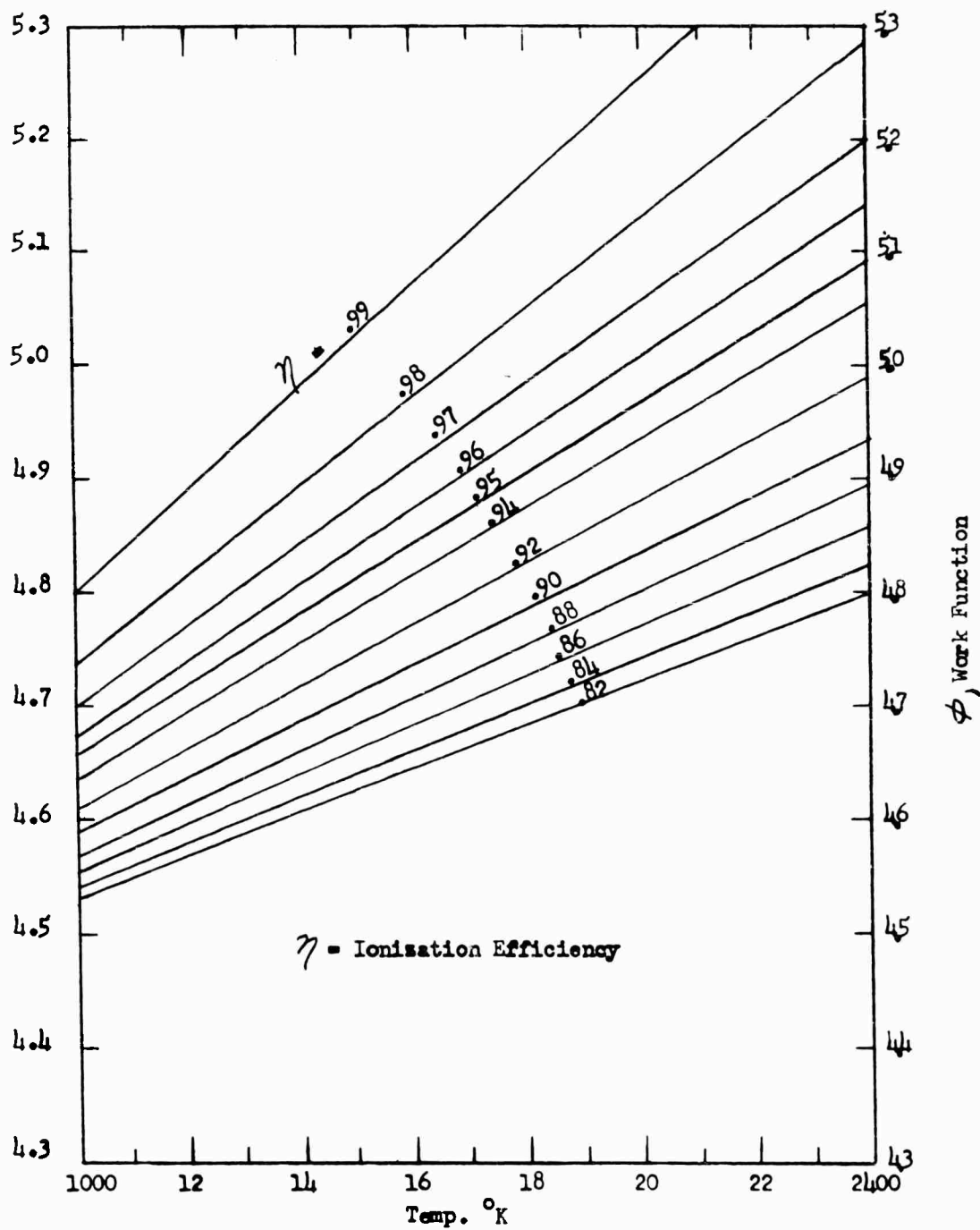
IONIZATION EFFICIENCY OF CESIUM

Figure II-2.



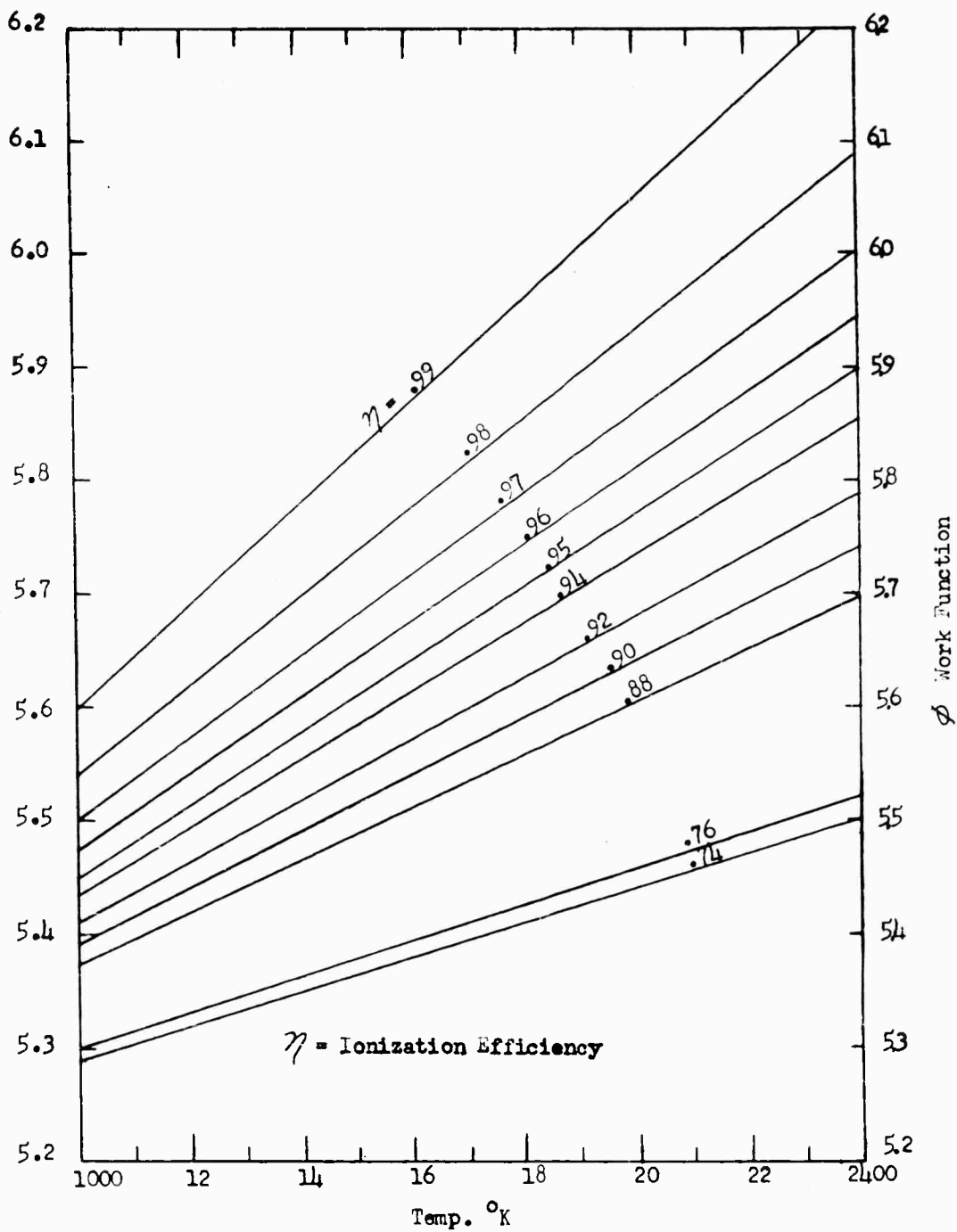
IONIZATION EFFICIENCY OF RUBIDIUM

Figure II-3



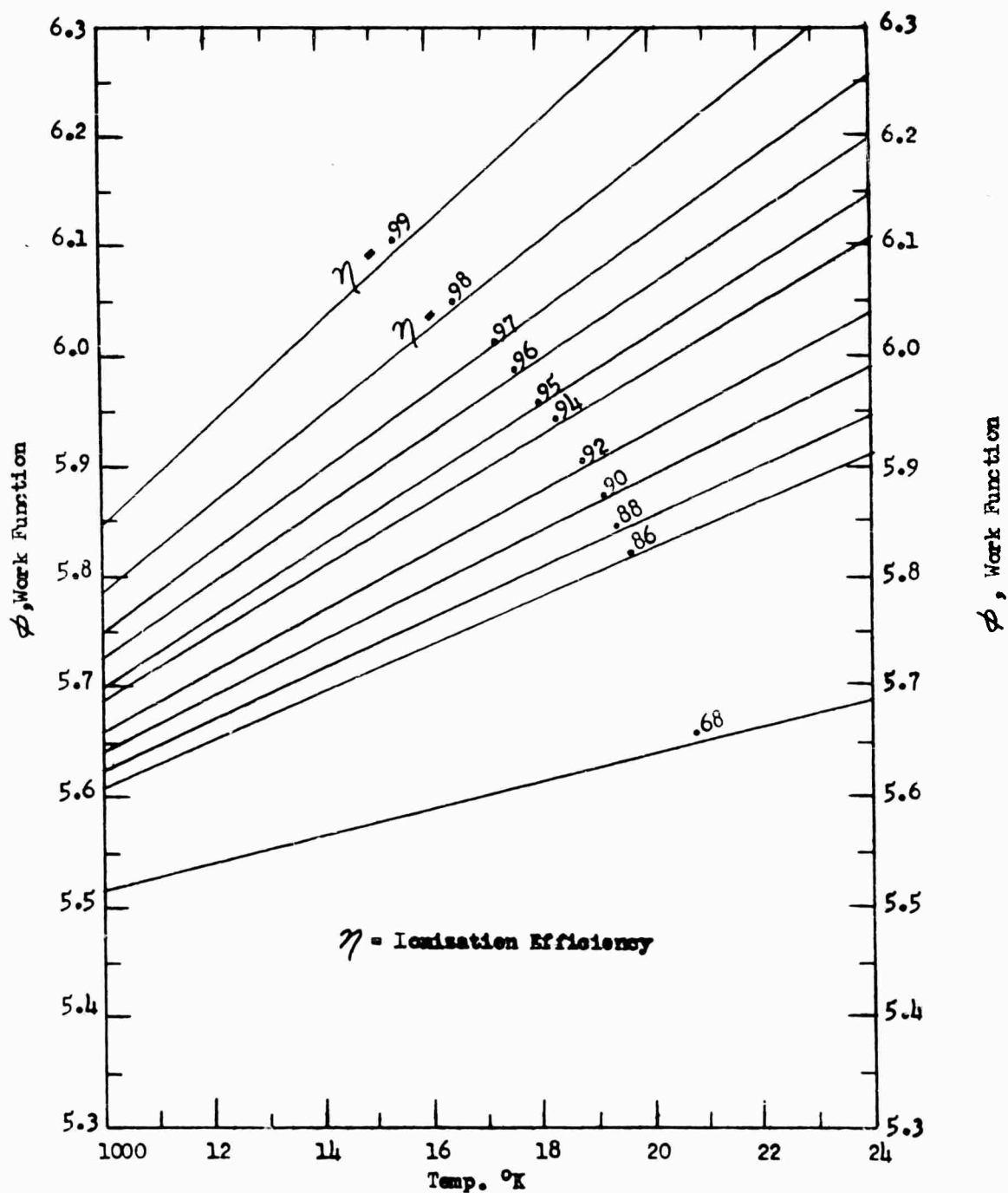
IONIZATION EFFICIENCY OF POTASSIUM

Figure II-4



IONIZATION EFFICIENCY OF SODIUM

Figure II-5



IONIZATION EFFICIENCY OF LITHIUM

Figure II-6

The work functions in TABLE II-B are the electron work functions and do not necessarily dominate in the charge exchange process. For example, two different work functions are reported for platinum. As recent investigations show, the work function is very dependent on the crystallographic index of the emitting surface (Ref. 17). Dependence of the work function on the temperature, as assumed in earlier investigations, may be explained on the basis of this index (Ref. 3). Two commonly used independent methods of measuring the electron work function are the Richardson equation, predominantly, and also the photo-effect. If there are patches of lower work function on the surface, these will strongly influence the electron emission. Thus, the work function given in TABLE II-B may be considered as a lower limit (Ref. 17). The upper limit of work function can be measured with an alkali of sufficiently high ionization potential. In the case of an oxide layer, the work function is increased considerably, as has been measured for W-oxide and Pt-oxide. Unfortunately, the oxide layers have a short lifetime at elevated temperatures; therefore, they are not of interest unless a sufficient amount of oxide can be supplied continuously (Ref. 18). Desorption of oxygen from tungsten takes place in three stages. Bursts of gas are desorbed at about 500°K, 1150°K, and 1750°K. The work function is of the order of 6 volts or more until the second desorption stage is completed, at which time the work function drops to approximately 5.5 volts. A similar desorption occurs for a Pt-oxide layer.

In regard to the crystallographic index, Hughes, et al., investigated W single crystals (Ref. 17). Their results are in good agreement with the data discovered earlier by E. Mueller (Ref. 18). The lowest work function is exhibited by the W-116 plane; for the 011 plane Mueller found values of 5.70 to 5.99 volts. The Hughes group concluded that the thermionic emission is identical for the three crystallographic directions 112, 112, and 110 with a work function of 5.25 ± 0.05 volt. By etching methods they achieved the surfaces on a single crystal wire. If the emitter is not a single crystal, it is impossible to get the same crystallographic plane over the total surface. Because the ionization efficiency on such higher work function patches is considerably higher than on the other areas, they contribute more to the ionization and, therefore, the overall work function must be weighed. The present experimental investigation is limited to tungsten, molybdenum, and platinum, but in the next phase of the investigation porous Re-plates, sintered or welded in Re-tubes, should be tried. The work function and melting point of rhenium are promising and this material seems to be more workable than tungsten or molybdenum.

To obtain an ion source as compact as possible, it is necessary to achieve high current densities. Under optimal conditions, which are described later, the total amount of fuel (alkali metal) evaporated per unit time is dependent on the emitter surface temperature and follows an exponential law.

$$1/t = (\text{const}) \exp (-Q/kT) \quad (\text{Eq. II-2})$$

where

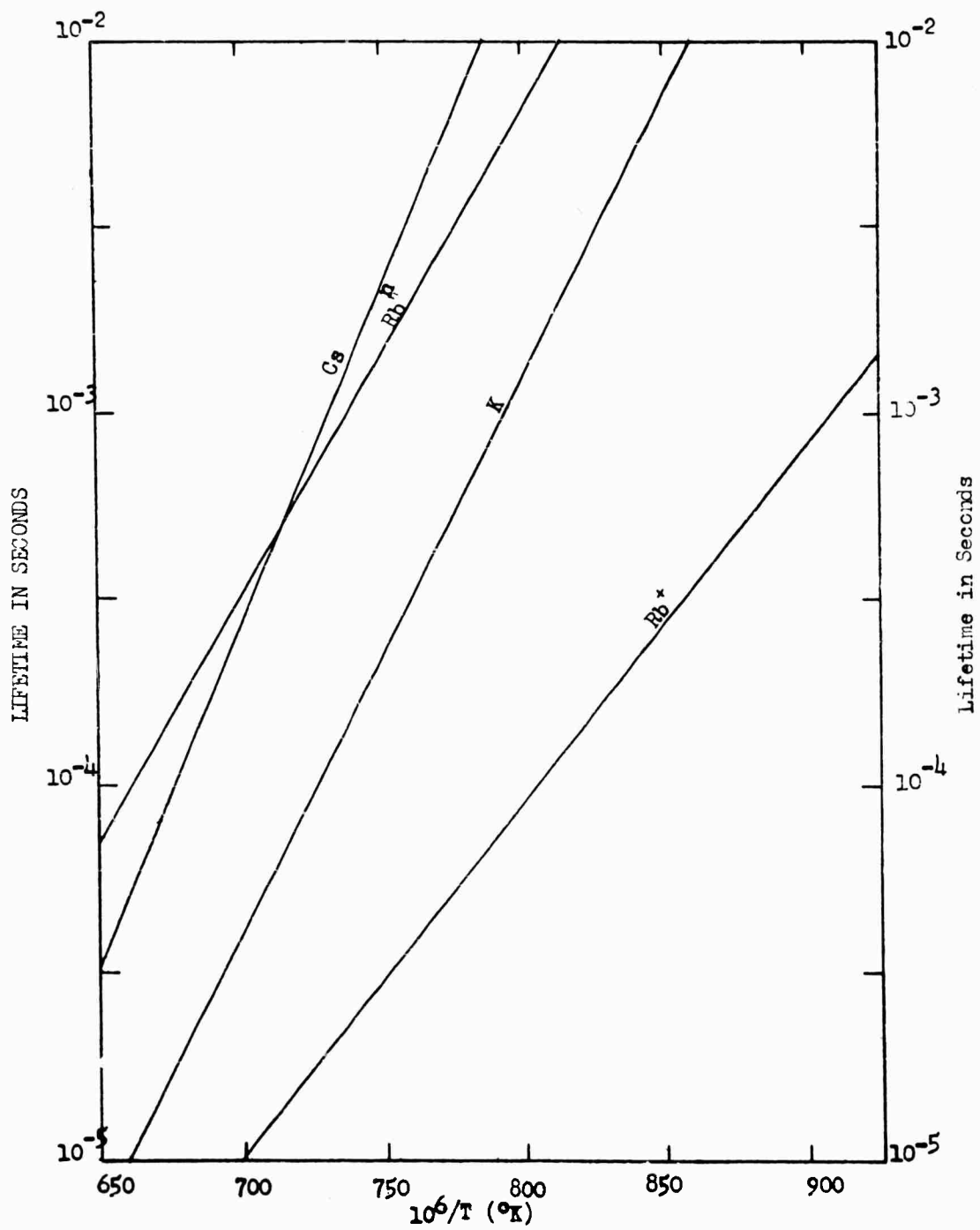
Q = absorption energy
k = $(1.38) 10^{-16}$ erg deg⁻¹
T = deg. Kelvin
t = lifetime on the surface

The lifetime (t) on a clean heated tungsten surface, therefore, decreases exponentially with increasing temperature. As Equation II-2 shows, it increases with the absorption energy. Platinum is less desirable than tungsten and molybdenum; the melting point limits the current density.

The lifetimes for ions are shorter than for the atoms of the same substance. Hughes, et al., report values of both lifetimes for rubidium (Ref. 17). In earlier reports, Knauer (Ref. 19), Bull and Marshall (Ref. 20), and Evans (Ref. 21) reported one lifetime for both. At temperatures of 2000°K the lifetimes are estimated to be between 10^{-5} and 10^{-7} seconds for alkali metals on tungsten. The lifetime is of interest because the emitter saturation current density is inversely proportional to the ion lifetime. Lifetimes for cesium, rubidium, and potassium are shown in Figure II-7 using available data. The effect of surface contamination is illustrated in Figure II-8 (Ref. 17).

To prevent the work function changing from that of the emitter material to that of the fuel, the surface coverage with fuel should be less than 1% of a monatomic layer of the fuel (Ref. 19). The lifetime of the fuel on the emitter surface must be short enough to prevent the build-up of a monatomic layer in excess of approximately 1%; therefore, the diffusion flow rate must be adjusted. In considering a porous emitter, the plate can be thought of as a parallel bundle of many fine capillary tubes. If the surface migration time of the fuel on the emitter surface is not high enough, the fuel concentration will exceed 1% around the ends of the capillaries and, in consequence, the work function will be sharply reduced from that of the plate material to that of the fuel. Migration of the fuel on the emitter surface depends on the surface temperature and increases with the temperature. Recent data on the migration time of alkali on tungsten surface are not available, although some information has been published by Becker (Ref. 22), Benjamin and Jenkins (Ref. 23), and Frank (Ref. 24). It appears that the earlier investigations were made with insufficiently clean surfaces; therefore, the measured values may not be applicable. Further experimental investigations in this field appear to be warranted.

The question of migration time would appear to be negligible if a solid emitter surface is used and the fuel is equally distributed over the exchange plate by means of an atomic beam. To achieve this a small angle between incident atom-beam and the plate is useful.



LIFETIME ON HEATED TUNGSTEN SURFACE

Figure II-7

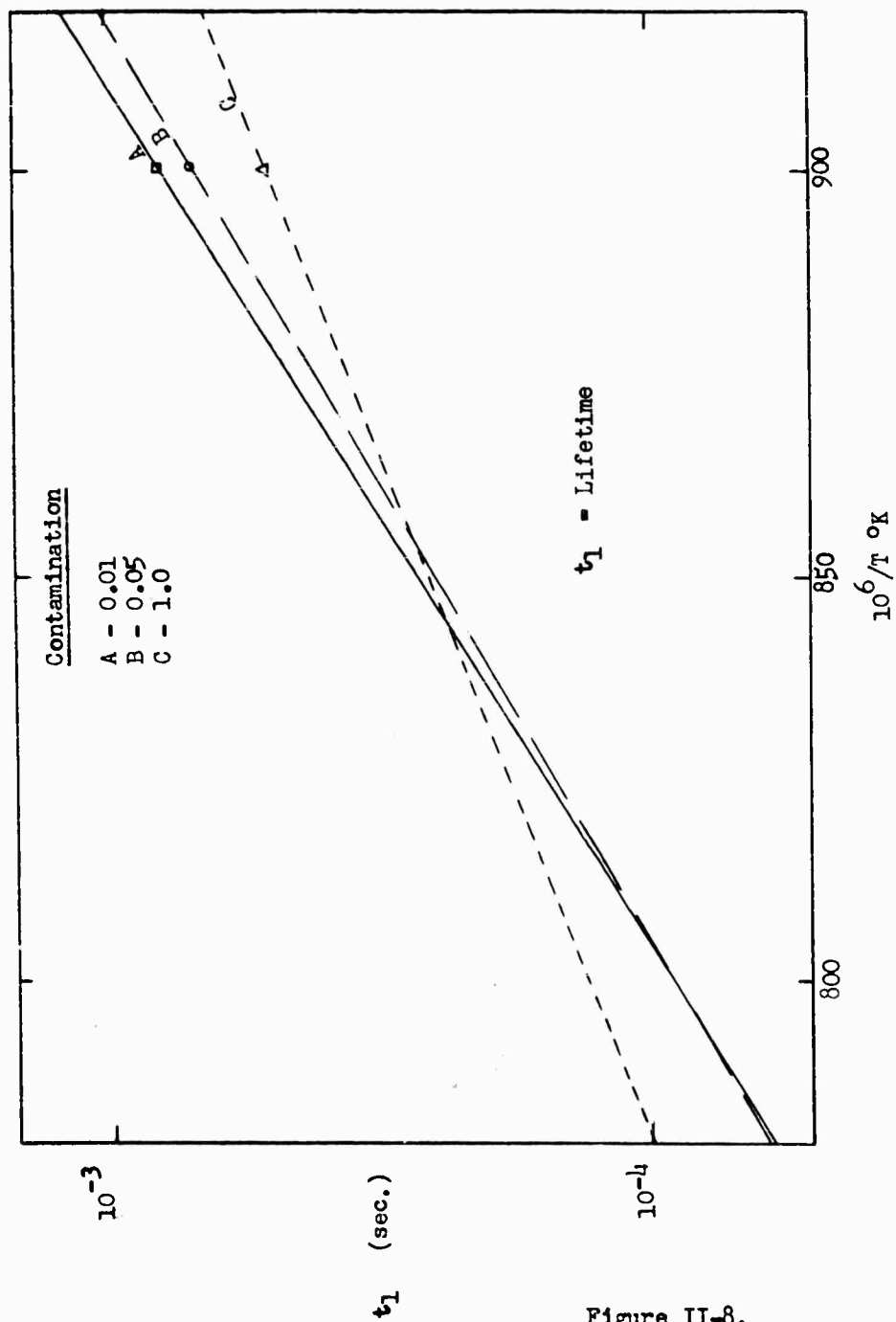


Figure II-8.

The fuel beam gun can be built into the focusing electrode (which is at the same potential as the ion emitter) of a Pierce type accelerator. Evaporation of the fuel from the accelerating electrode, however, may have disadvantages because of the breakdown voltage in the alkali-vapor.

In addition to the factors of ionization efficiency, fuel lifetime on the surface, and migration velocity, the ion beam current density is also governed by the fuel flow rate through the emitter material ("through" because this experimental investigation is confined to porous plates and fine screens).

Depending on the fuel vapor pressure and on the design (and the operating conditions) of the porous plate, a certain amount of the fuel will penetrate the porous plate and be evaporated from the surface. The saturation vapor pressures of the alkali fuels are relatively well known, and are given as a function of temperature in Figure II-9. The pertinent equations are:

$$Li : \log p = 8.00 - 8143/T$$

$$Na : \log p = 9.235 - 0.5 T - 5567/T$$

$$K : \log p = 8.793 - 0.5 \log T - 4552/T$$

$$Rb : \log p = 10.55 - 4132/T$$

$$Cs : \log p = 11.176 - 1.4 \log T - 4042/T$$

where p is mm Hg and T is degrees Kelvin.

The above equations are taken from Ditchburn and Gilmour (Ref. 25). Earlier references include those of Eucken (Ref. 26), and Taylor and Langmuir (Ref. 9).

The flow rate through the emitter is a function of the inlet fuel vapor pressure (P_1), the mean pore diameter, and the exit pressure (P_2). At higher fuel pressures, the flow rate follows the equation for viscous flow:

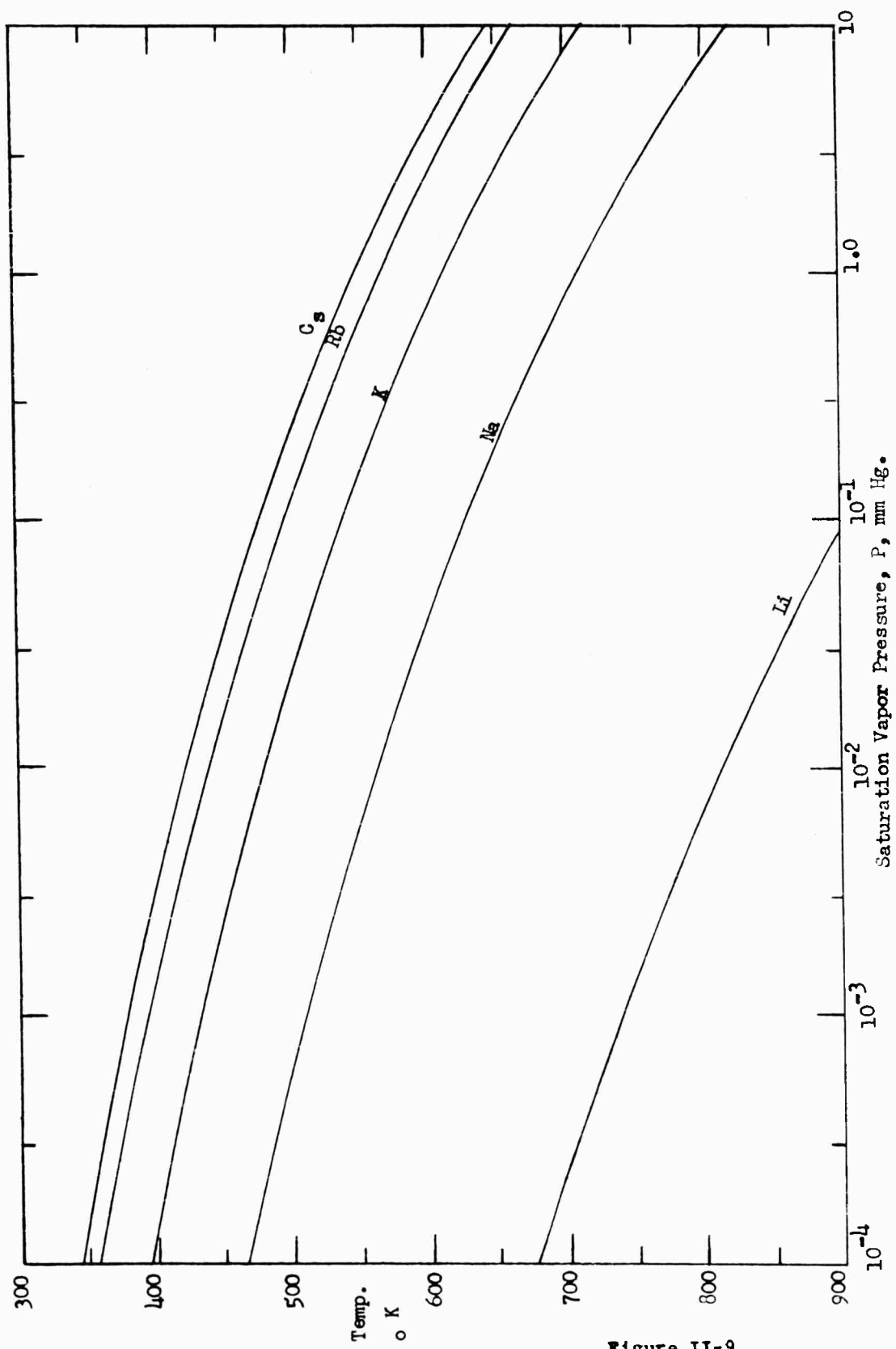
$$F_v = (1.33 \pi r^4 / 8 \eta L) \left(\frac{1}{2} \right) (P_1 + P_2) \quad (\text{Eq. II-3})$$

where

$$F_v = \text{viscous flow rate, cm}^3 \text{ sec}^{-1}$$

$$\eta = \text{viscosity coefficient}$$

$$r = \text{mean pore diameter, cm}$$



SATURATION VAPOR PRESSURE OF ALKALI METALS

Figure II-9

L = effective pore length, cm

P = pressure, microns

With smaller pore sizes and lower vapor pressures, the flow changes from viscous flow to slip flow and subsequently to molecular flow. Molecular flow denotes the condition wherein the mean free path is equal to or greater than the mean pore diameter. The mean free path for the alkali metals as a function of pressure is given in Fig. II-10 for temperatures of 1200°K and 2000°K. For comparative purposes, the mean free path of helium, argon, and xenon is shown, computed using the following equation:

$$\lambda = (7.6) 10^{-17} / \pi \sqrt{2} (2.68) d^2 (P) \quad (\text{Eq. II-4})$$

where λ is the mean free path in cm, and

d = atomic diameter, cm, where $d^2 = d_0^2 (1 - C/T) (1 + C/273)$

d_0 = atomic diameter at zero deg. C

C = Sutherland constant

P = pressure, mm Hg

The equations for slip flow and molecular flow, respectively, are given below.

$$F_{sp} = [(1.33 \pi r^4) (\frac{1}{2}) (P_1 + P_2) / 8 \eta L] + [8 \pi r^3 v_a / 12L] \quad (\text{Eq. II-5})$$

$$F_m = (8 \pi r^3 v_a / 12L) \quad (\text{Eq. II-6})$$

When the mean free path of an atom absorbed on the capillary surface is equal to or greater than the mean pore diameter, then surface flow also contributes to the total flow-rate, as given in Equation II-7 for constant plate temperature.

$$F_s = F_m (1 + a) \quad (\text{Eq. II-7})$$

where

F_{sp} = slip flow rate, $\text{cm}^3 \text{ sec}^{-1}$

F_m = molecular flow rate, $\text{cm}^3 \text{ sec}^{-1}$

F_s = surface flow rate, $\text{cm}^3 \text{ sec}^{-1}$

a = $(3/4) D_s(T) \sigma \theta_0 / (r^2) (v_a)$

v_a = mean velocity, $(1.455) (10^4) (T/M)^{1/2}$, cm sec^{-1}

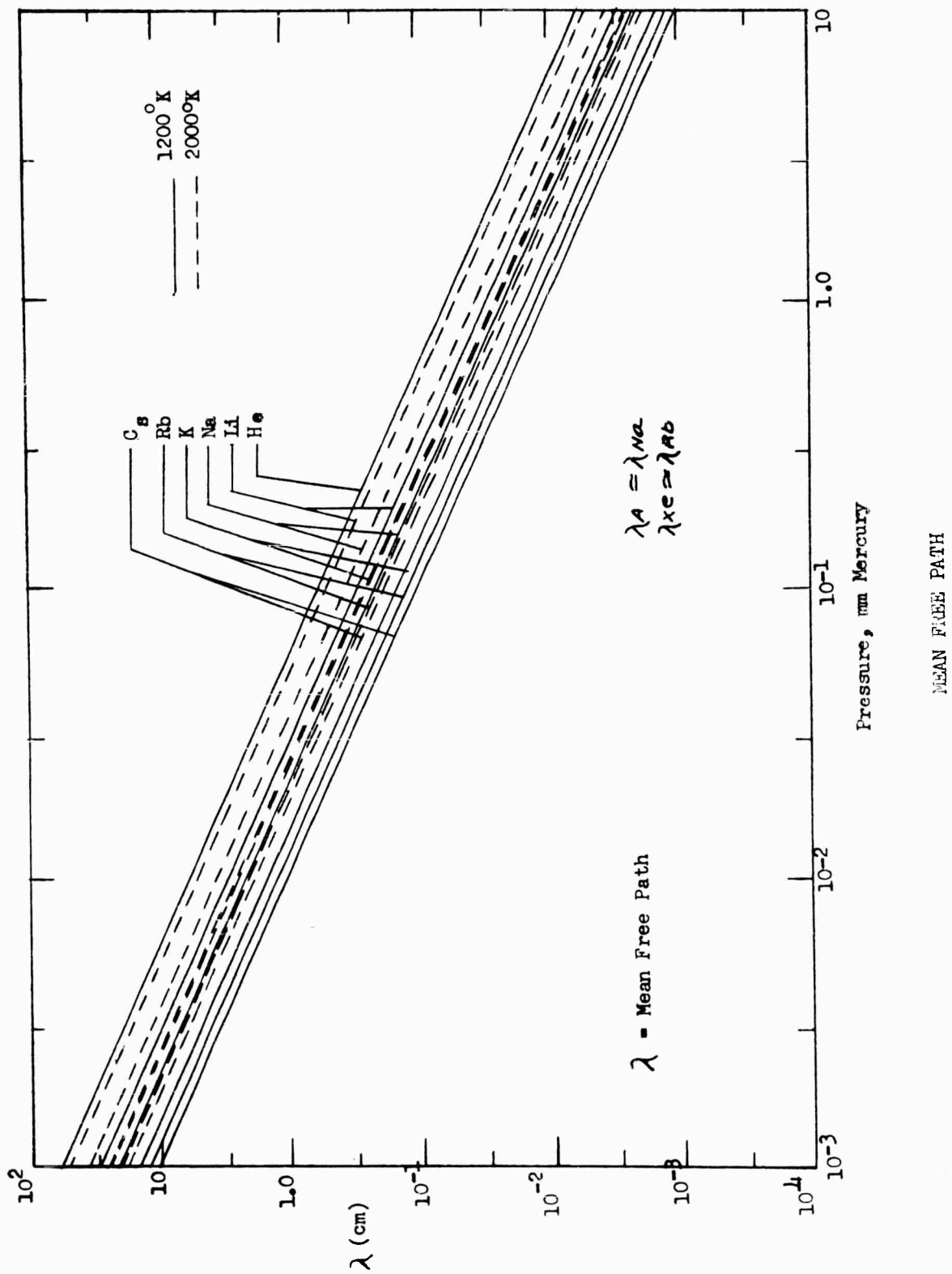


Figure II-10

$D_s(T)$ = surface diffusion coefficient

σ = surface concentration of adsorbed atoms

θ_0 = local surface coverage

T = temperature, deg. Kelvin

In the case of a porous emitter, the ratio of capillary length to diameter is greater than 100, so there are no corrections for short capillaries. The ratio of viscous flow to molecular flow would give the effective pore radius and, with the equation for the molecular flow, also the effective pore length, if it were assumed that the capillaries are circular and that the total flow rate is not affected by surface flow. Tortuosity of the capillary and deviation from a circular shape reduce the flow rate through the capillary. It is not possible in the case of a porous emitter to distinguish between the length and the shape of the capillary.

As will be discussed later in the section on "Diffusion Experiments", the emitter (porous or screen) can be calibrated for flow at various differential pressure conditions. Briefly, the emitter is connected on the inlet side to a container of constant volume filled with an inert gas (such as helium); the exit side is evacuated. Using a flow measuring apparatus, the dependence of flow rate on plate temperature, pressure differential, and fuel atomic weight can be determined and utilized in the design of the ion source.

As shown in Figure II-11, the total computed flow rate per unit area (F_m) is proportional to $1/T^{1/2}$ and to r ; whereas the contribution of the surface flow rate is proportional to $1/r$.

A factor which mitigates in favor of a high beam current density is the smaller emitter area which results, and the reduced power loss due to spatial heat radiation. It has already been shown that high emitter temperatures are required for efficient ionization, between 1100°K and 2000°K. The heat loss by radiation increases rapidly with temperature. For example, Figure II-12 shows power loss as a function of emissivity and temperature. Values of total emissivity between 0.13 and 0.26 are reported for tungsten in the temperature range of 1100°K to 2000°K.

It is also advantageous to limit the radiating area to the emitter surface itself; i.e., with a minimum "seeing" angle. Sideways emission can be reduced in part by radiation shielding. For example, if there are n thin metal shields of the same emissivity between parallel walls, then the energy loss reduces to:

$$E = \sigma (A) (\epsilon) (T_1^4 - T_2^4) / (1 + n)$$

(Eq. II-8)

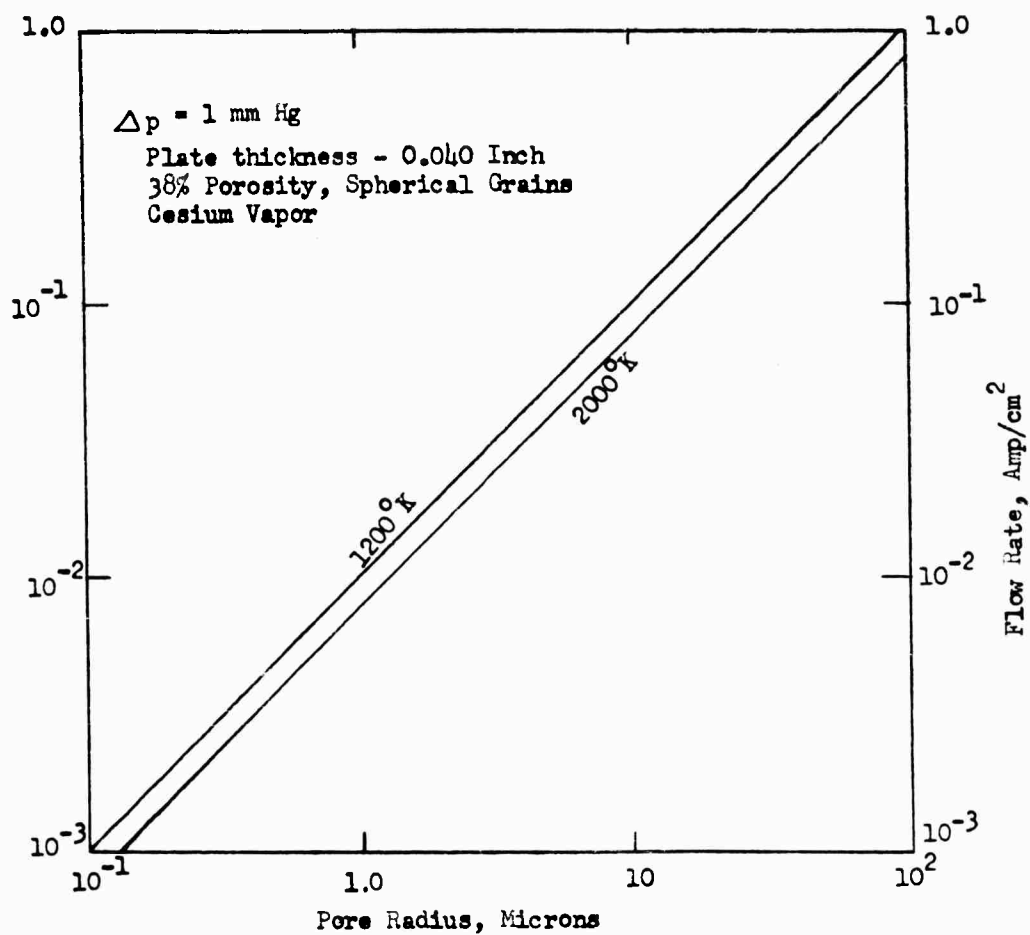
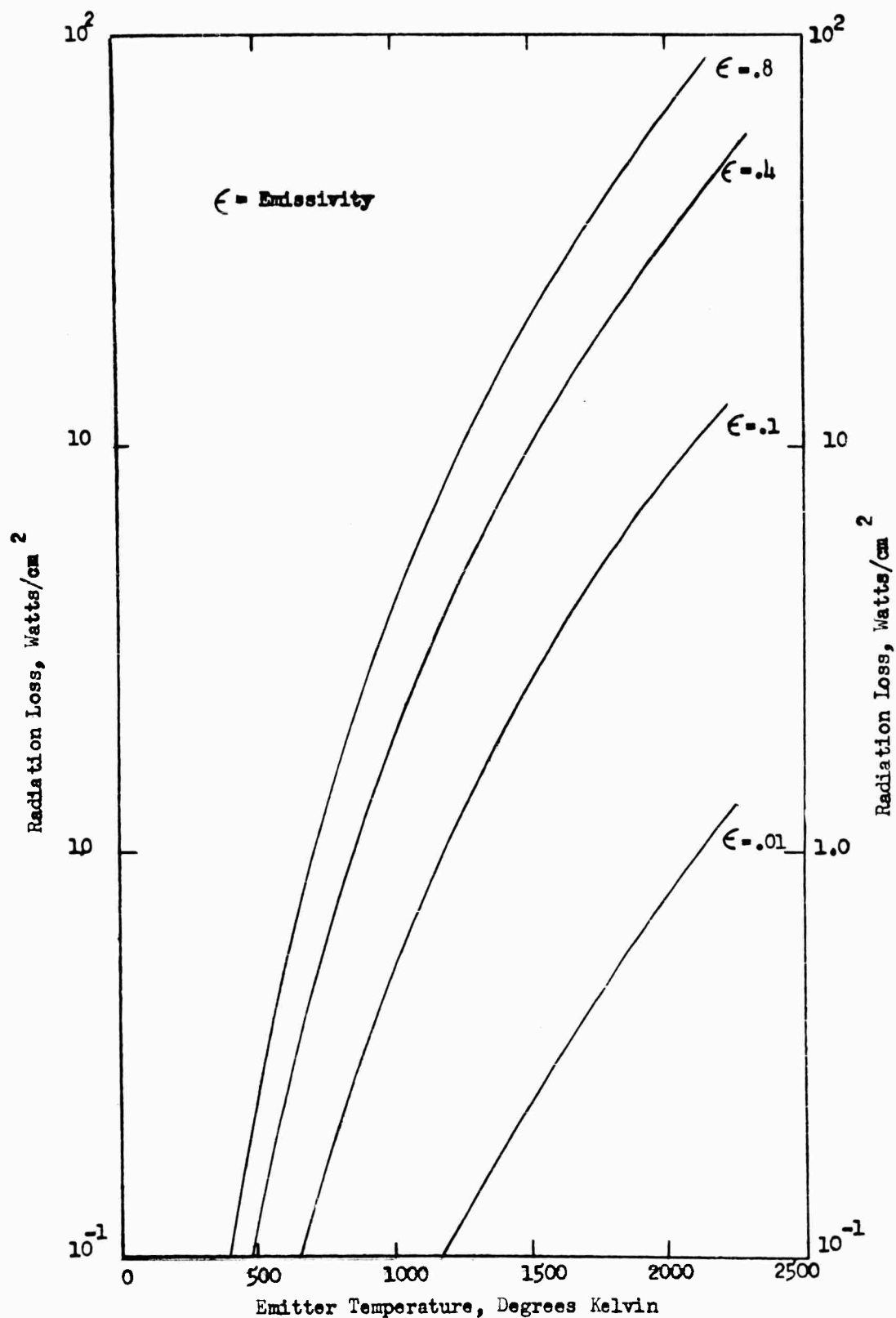


Figure II-11

FLOW RATE AS A FUNCTION OF PORE SIZE AND EMITTER TEMPERATURE



HEAT LOSS BY RADIATION TO SPACE AS A
FUNCTION OF EMITTER TEMPERATURE AND EMISSIVITY, NEGLECTING SOLAR RADIATION

Figure: II-12.

where

E = watts per sq cm

σ = $5.67 (10^{-12})$

A = surface area, cm^2

By proper shielding, the thermal radiation loss from the emitter therefore can be reduced. The overall loss, as indicated previously, can be further reduced by utilizing a minimum emitter surface, or correspondingly a high current density.

The production of an ion beam is governed not only by the fuel flow rate through the emitter and the emitter temperature, but also by the capacity of the ion extraction and acceleration systems. The ion current is space-charge-limited in accordance with the Child-Langmuir Law:

$$j = (5.45) (10^{-8}) U^{3/2} / (d^2) (M_i^{-1/2}) \quad (\text{Eq. II-9})$$

where

j = ion current density, amps cm^{-2}

U = accelerating potential, volts

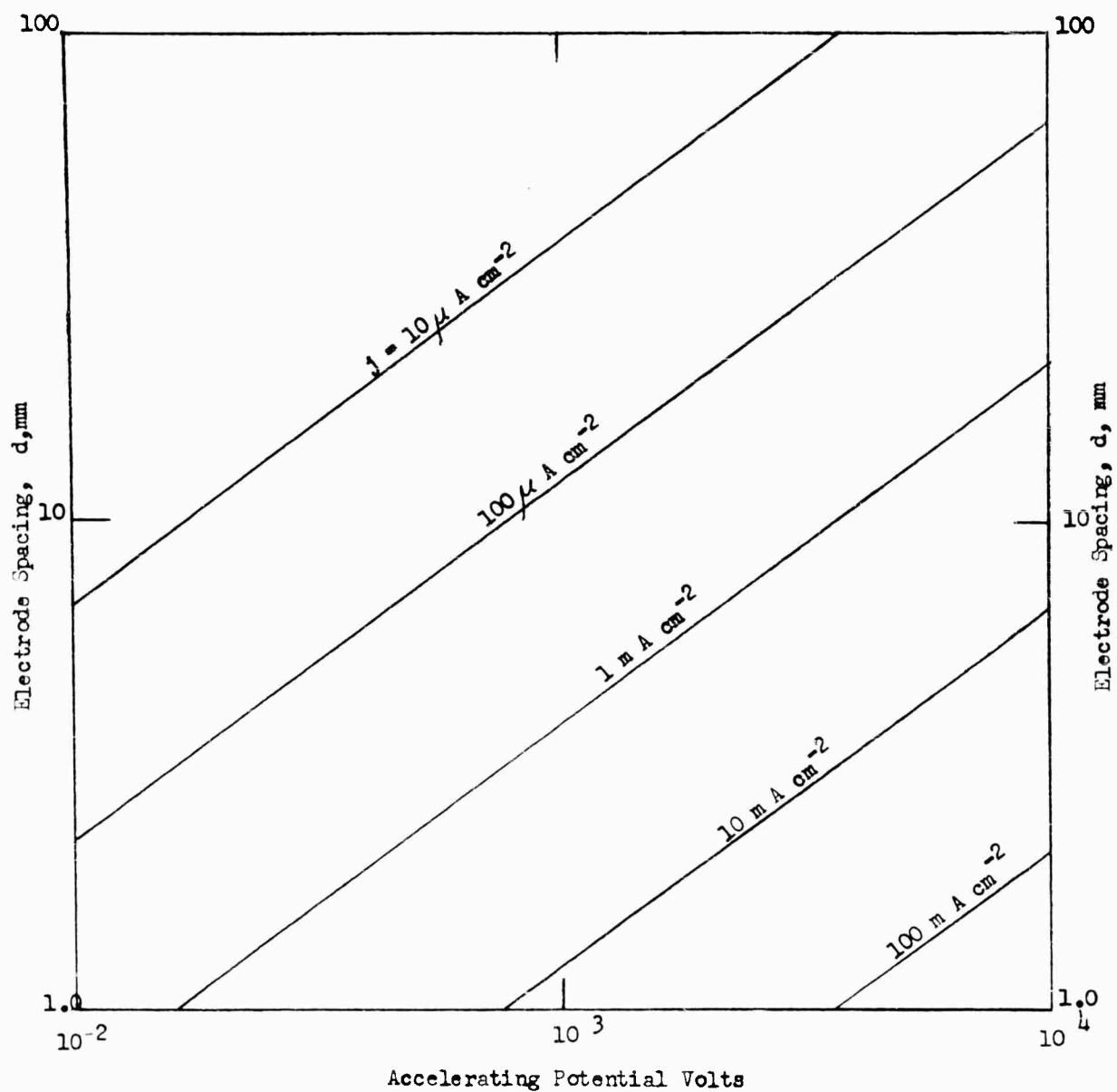
d = spacing between emitter and accelerating electrode, cm

M_i = atomic weight

Figure II-13 illustrates for cesium the dependence of the current density on the electrode spacing at various accelerating voltages. The space-charge-limited current density attainable for various fuels and accelerating potentials is given in Figure II-14, assuming an electrode spacing of 10mm. A reduction in the spacing between the emitter and the accelerator electrode sharply reduces the required voltage, but, on the other hand, the limit may be governed by field emission of electrons from the accelerating electrode which can be reduced by increasing the electrode work function. A portion of the emitted ions will impinge upon the acceleration electrode and reduce the work function. Because of the elevated temperature of the acceleration electrode, an equilibrium condition of fuel coverage on the electrode will be attained and (especially with an alkali fuel) the work function will be lowered so that the electrode may be converted to an electron emitter.

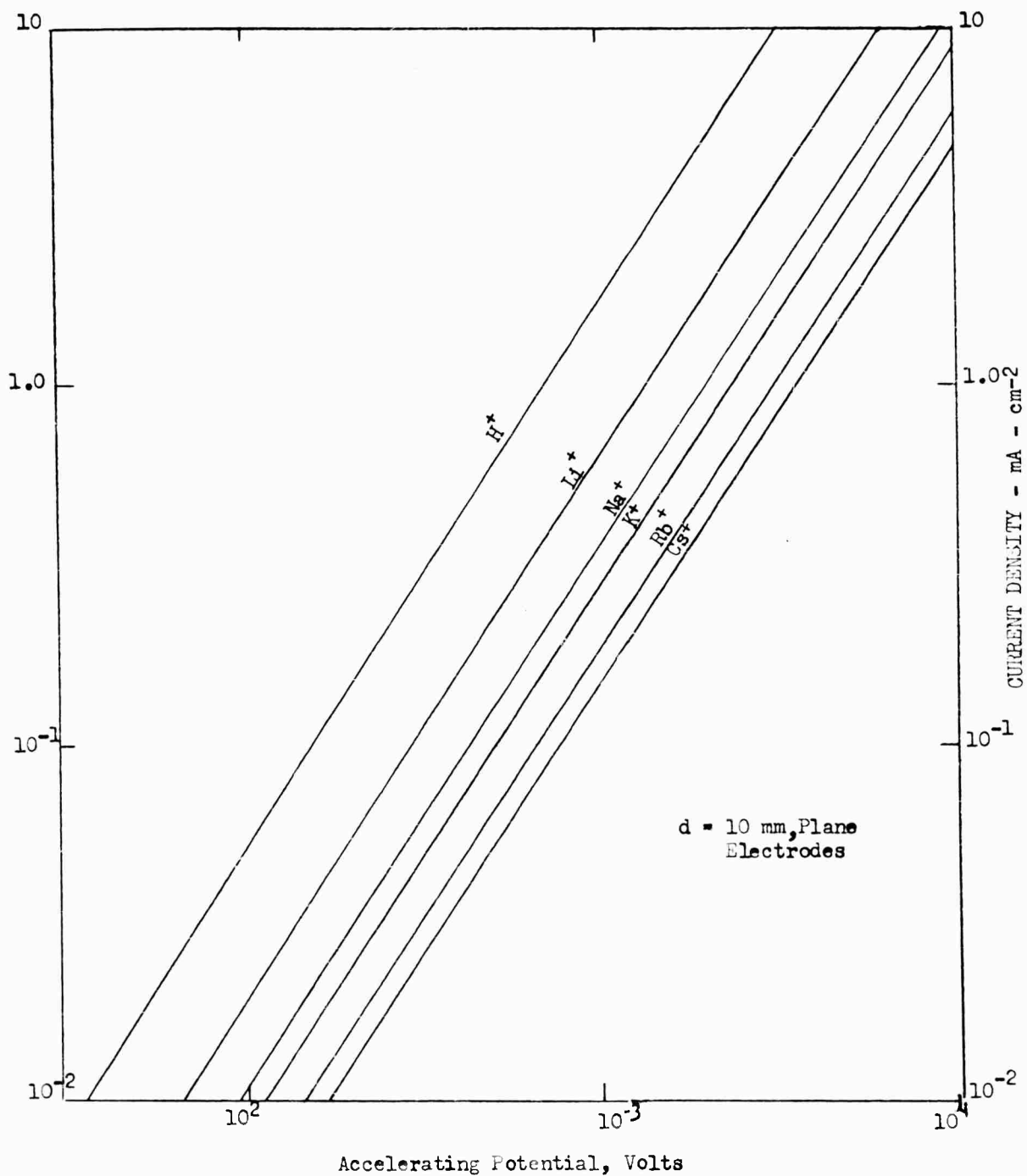
An approximation for the minimum electrode distance for discharge in centimeters is given by the equation:

$$d_{\min} = U / (10^5) \text{ (a)} \quad (\text{Eq. II-10})$$



EFFECT OF ELECTRODE SPACING FOR PLANE ELECTRODES
WITH CESIUM IONS

Figure II-13



EFFECT OF ION MASS ON CURRENT DENSITY

Figure II-14

where 'a' is 1.70 for rounded polished nickel electrodes at room temperature, U is expressed in volts, and equation II-10 pertains to pressure levels less than 10^{-4} mm Hg. The minimum radius for edges on the electrodes in areas of high field gradients is as follows:

$$r_{\min} = U_{kv}/20 \quad (\text{Eq. II-11})$$

where r_m is the radius in mm and U_{kv} is the accelerating potential in kilovolts. The use of values of r_m less than 0.2 is not recommended.

As indicated previously, cesium deposition on the acceleration electrode (by neutrals or ions) reduces the electrode work function and increases the possibility of field electron emission, as indicated in Figure II-15. Voltage breakdown in cesium vapor appears not to be a problem if a sufficiently high vacuum (low pressure) is available. However, if a grid type ionizer is used instead of a porous plate with its high ionization efficiency, then breakdown in the cesium vapor may be a significant problem.

At higher current densities, the beam tends to spread due principally to the space-charge effect. If (or when) the ions impinge on the electrode, material is sputtered with a loss both in fuel and in electrode material. Sputtering has been discussed by Wehner (Ref. 28), Goldman, et al (Ref. 29), among others. Following Wehner, the sputtering rate of molybdenum appears to be relatively low. Furthermore, molybdenum has a high melting point and therefore appears to be a good choice for electrode material. Extrapolation of the sputtering ratios for mercury given by Wehner indicate that the sputtering effect must be minimized in order to provide long life for the acceleration system. In addition, of course, the electron emission must be kept to a minimum.

A "conventional" method of focusing and accelerating the ion beam is the Pierce method (Ref. 32). Such a system is limited to a perveance of approximately 10^{-7} , where the perveance is given by the equation:

$$P = (M_i/m_e)^{1/2} (I)/U^{3/2} \quad (\text{Eq. II-12})$$

where

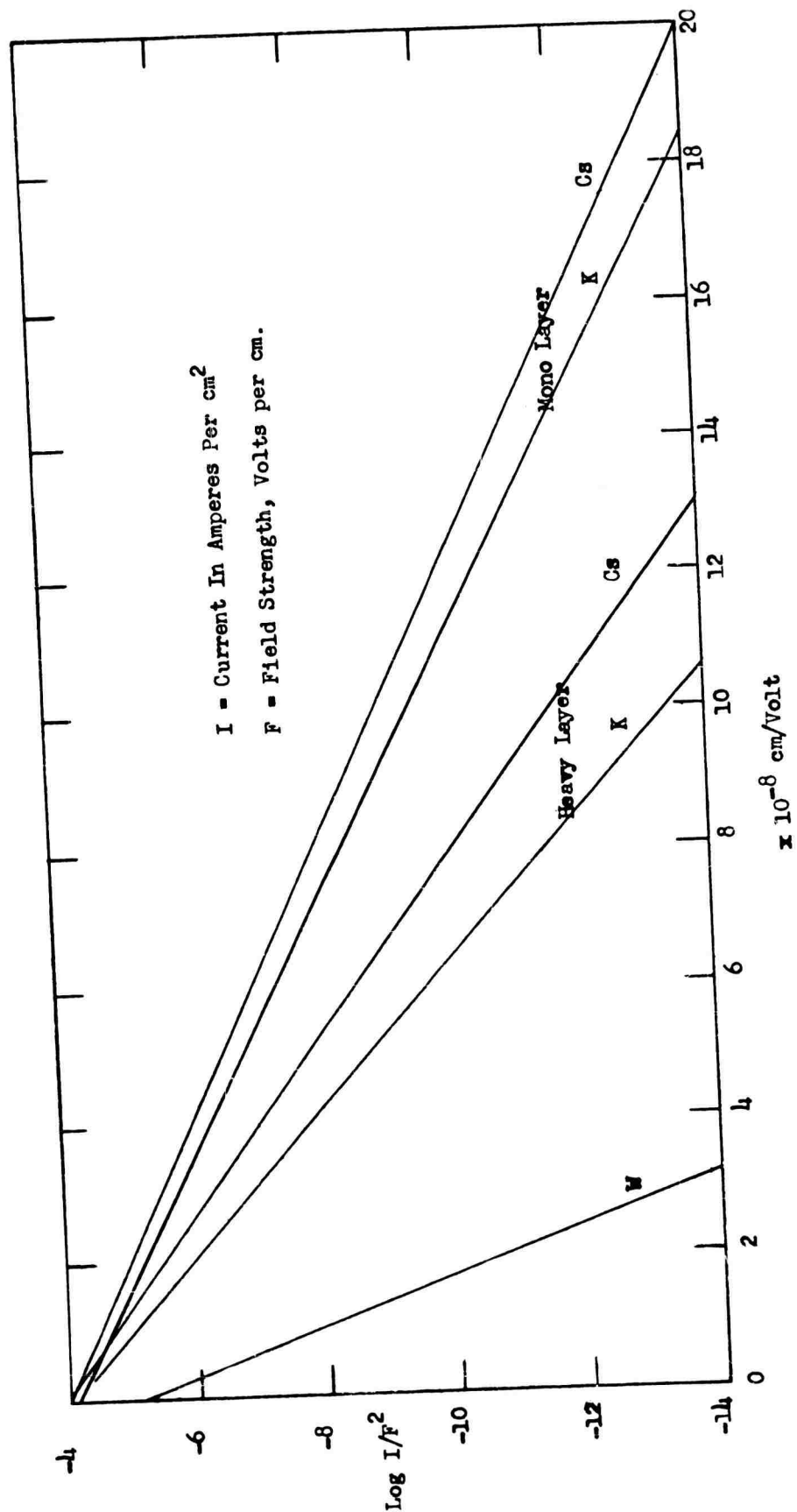
P = perveance

M_i = ion mass

m_e = electron mass

I = beam current, amps

U = accelerating potential, volts



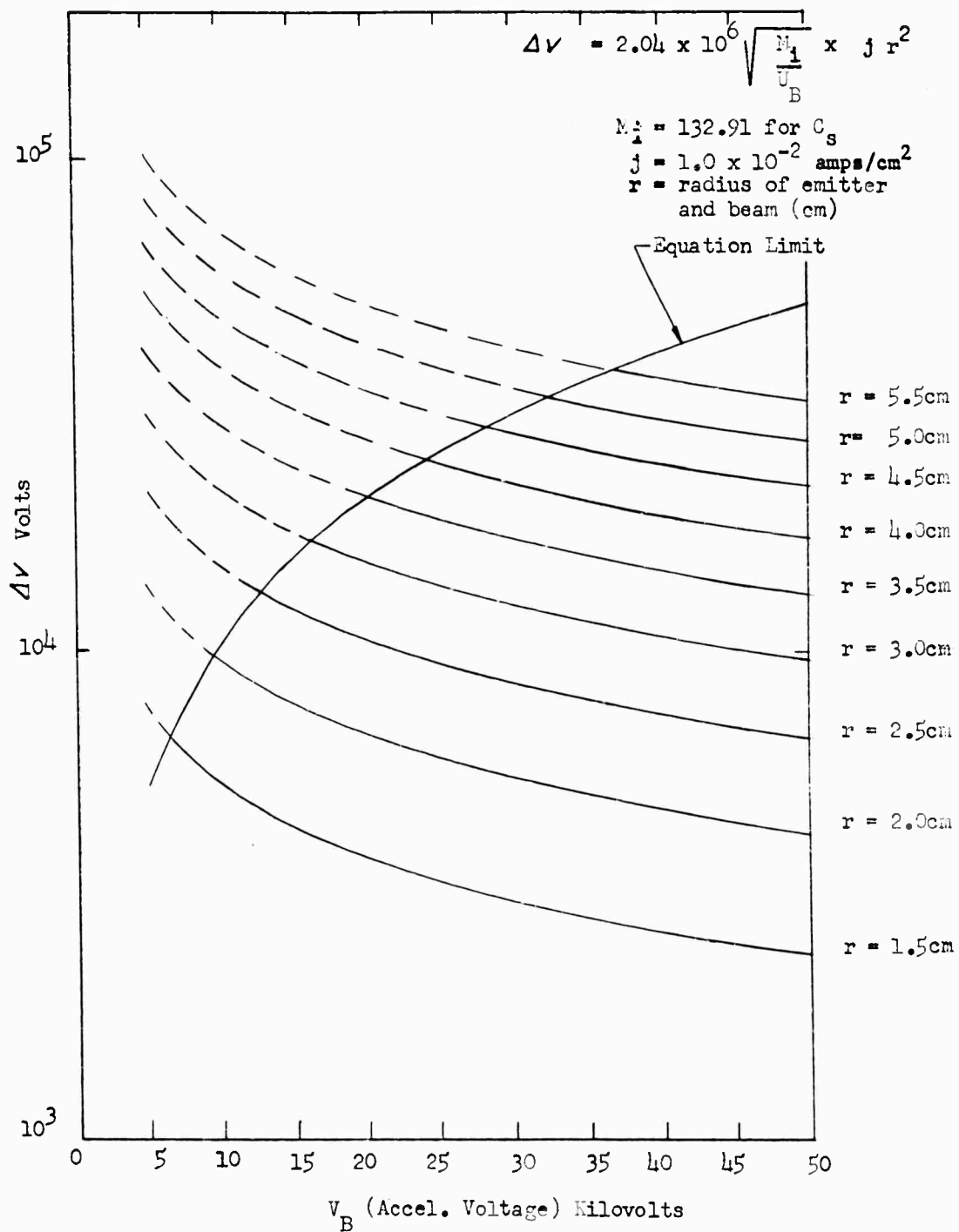
Field Emission
CURRENT-FIELD CHARACTERISTICS FOR TUNGSTEN COVERED WITH K AND Cs

Figure II-15

Perveances greater than 10^{-7} can be obtained by using electrostatic and magnetic fields, in accordance with Von Ardenne (Ref. 47), Hines (Ref. 33), Van Duzer and Brewer (Ref. 34), and Fox (Ref. 35). These types of acceleration systems merit further analysis.

The preceding discussion on sputtering and beam focusing-acceleration is pertinent to the present ion source investigation because the various sources can be evaluated and compared only if the beam is collected and measured. A consideration less germane to the source itself but unquestionably pertinent to the ultimate application is the problem of beam neutralization. The term "problem" is apropos; a considerable effort on beam neutralization has been and is being expended by various agencies (Ref. 36). Briefly, if a continuous stream of positive ions is being ejected, the same amount of the negative charge will remain in the system. Coulomb forces are built up and eventually will compensate the acceleration force. Therefore, it is necessary to eject the same number of negative charges with the positive ions. The question is how and where the ejection should occur, depending in some measure on the beam diameter and the acceleration gap. It would appear that electron injection directly into the beam is to be preferred, but the mechanism of mixing high-mass low-velocity ions with low-mass electrons is difficult and has yet to be fully developed. This problem is also under consideration at the Quehanna Laboratories, although not as an integral part of the present program on ion sources. Figures II-16 and II-17 illustrate the potential drop in the radial and longitudinal direction of an unneutralized beam. The potential drop indicates that injected electrons will be accelerated toward the center of the beam and toward the emitter plate, unless special provisions are taken.

It has been shown in the preceding discussion on the charge exchange method of ionization, that alkali metal fuels in contact with high temperature metals such as tungsten, molybdenum, rhenium, and platinum can provide a high ionization efficiency. The discussion also has included detailed consideration of such factors as diffusion flow through the emitter, atom and ion lifetimes, and emitter temperature effects. From the application viewpoint, brief mention has been made of sputtering, acceleration, thermal radiation losses, and beam neutralization, which are not principal areas of investigation in the present program. Other ion sources, principally the RF and plasma arc methods, are described in the following sections.



RADIAL POTENTIAL DROP IN A CESIUM ION BEAM

Figure II-16

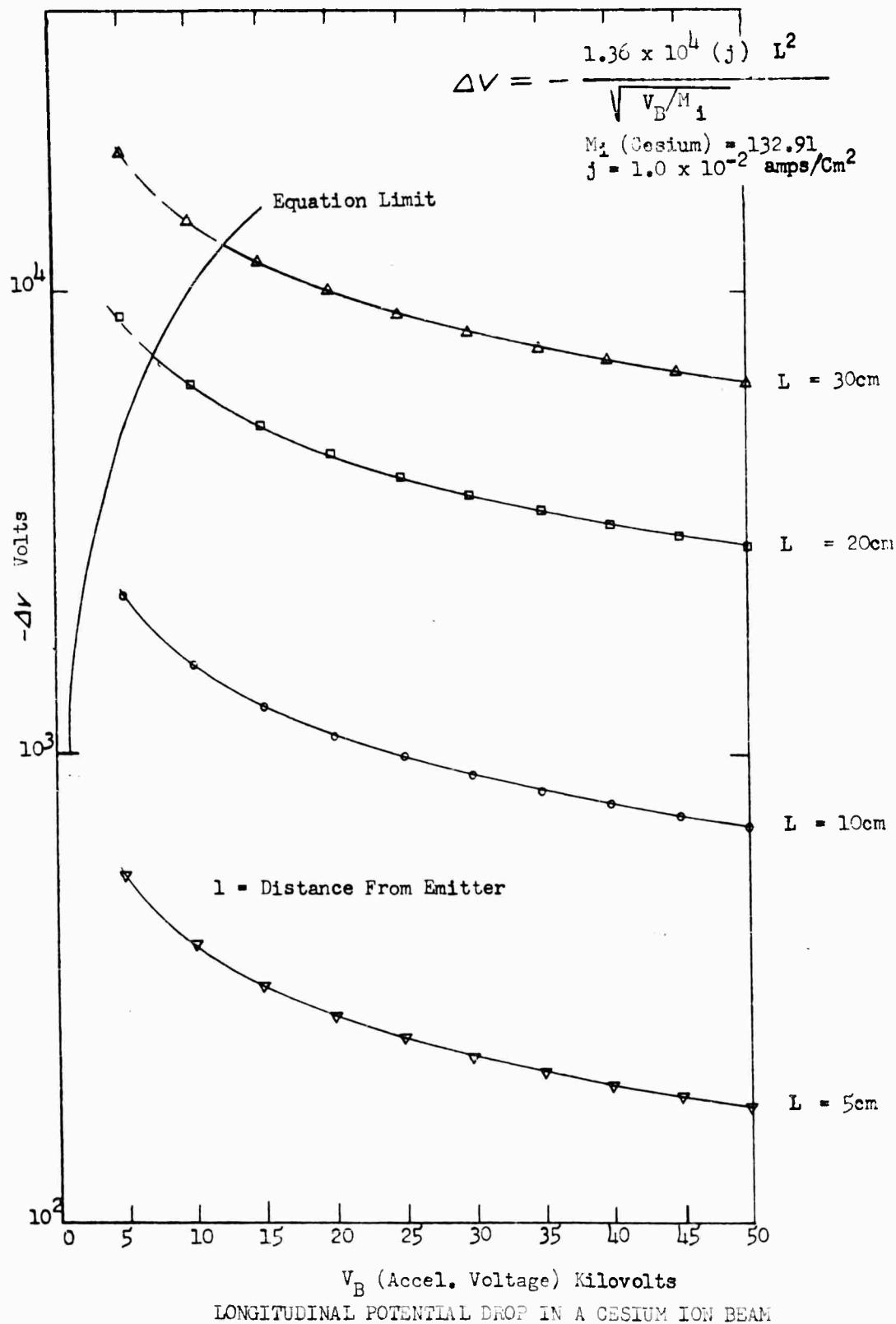


Figure: II-17.

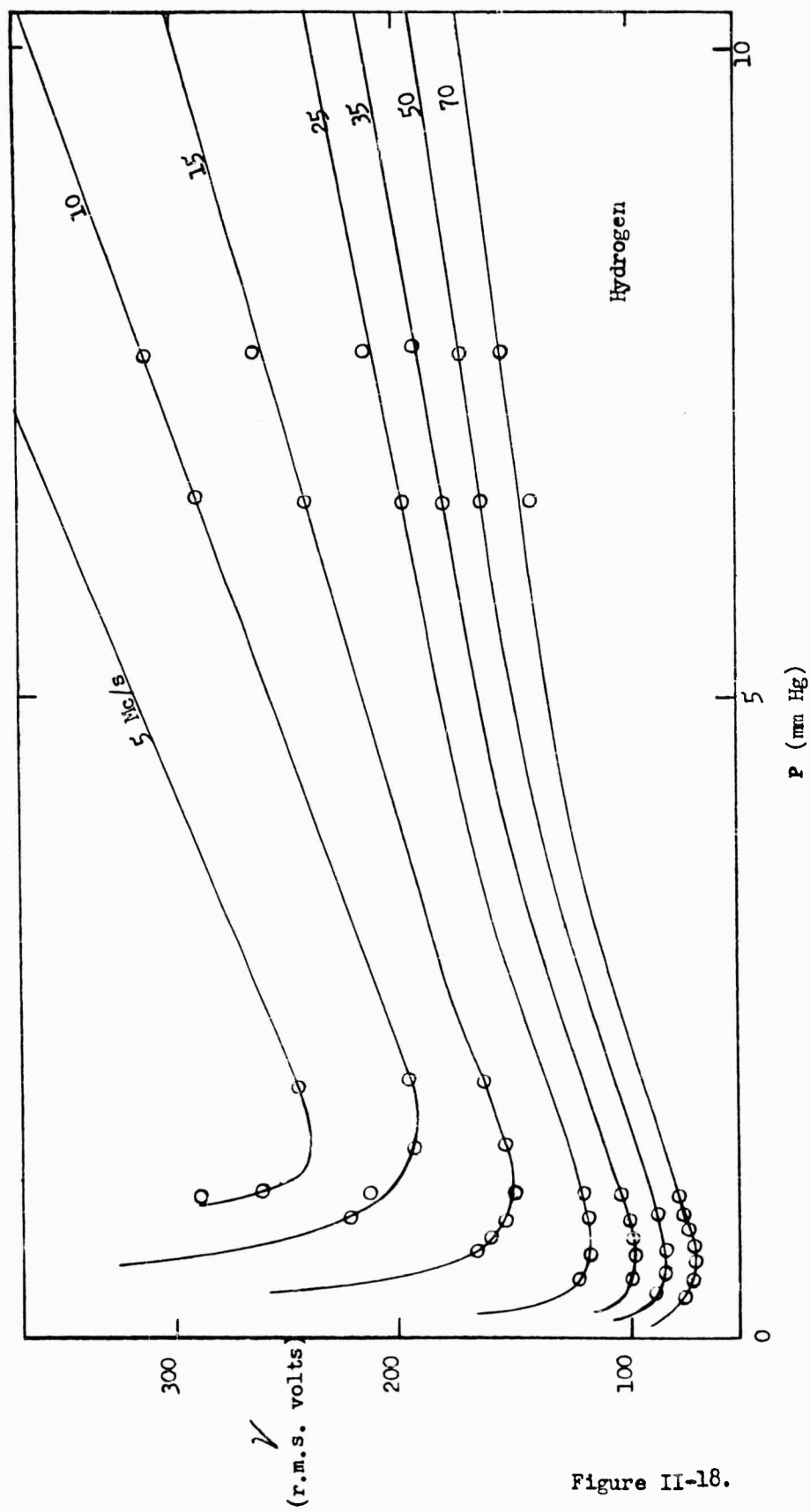
B. The RF Ion Source

Briefly stated, ionization can be obtained by subjecting the fuel vapor (e.g. cesium vapor) to a radio-frequency field. For a typical installation as discussed later in Section IX of this report, the vapor is enclosed within a glass container which is surrounded by external RF coils. The ions are extracted from the plasma boundary in the end of the container.

The mechanism of the RF ionization can be described briefly as follows. For ignition a certain amount of rest-ionization (as given in part by environmental cosmic radiation) is essential. The RF field (primarily the magnetic field component to prevent dielectric losses in the walls of the container) causes the free electrons to be accelerated and to ionize the low density gas or vapor. Before the ions reach the wall of the container, both the field direction and also the electron direction change. The breakdown potential follows the Paschen law (shown in Figure II-18) and decreases with increasing frequency. The operating frequency is in the range of 1.0 to 100 Mcps as shown in Figure II-18.

In the discharge area a luminous plasma is formed and serves as the source of ions. To extract the ions an electrostatic field is superimposed over the discharge area. In front of the negative extraction electrode a dark area is formed with a depth depending upon the applied potential and the plasma density. At some distance from the extraction electrode, the extraction field is screened by the positive space charge. The luminous plasma boundary is thus the ion-emitting surface. The dark area before the extraction channel is free of electrons and, therefore, also free of recombinations.

Inasmuch as the vapor pressure in the plasma is less than that used in other types of discharges, the extraction channel (aperture) can be larger, resulting in higher currents. Typical pressures in the RF discharge are in the range of 0.1 to 5.0 microns. Application of a longitudinal or transverse magnetic field to the RF discharge increases the plasma density, permitting lower gas or vapor pressures. Neuert, et. al., investigated the effect of a magnetic field on the discharge (Ref. 37). Fundamental studies on the RF ion source were performed by Thoneman (Ref. 38), Hall (Ref. 39), Neuert (Ref. 40), Chenot (Ref. 41), and Swann and Swingle (Ref. 42). Improvement over the first extraction systems was accomplished by Moak, et.al., (Ref. 43) and in particular by Reifenschweiler (Ref. 44) and Sommeria (Ref. 45 and 46). Reifenschweiler investigated the extraction channel with the result that the channel diameter can be increased and the channel length decreased due to the beam crossover in the channel. At the crossover point only a small aperture is necessary. Sommeria investigated the plasma-channel extraction conditions and showed good results by the arrangement of an electrostatic lens with its focal point in the aperture. Other investigators including Moak used a magnetic field for



BREAKDOWN IN R F FIELD WITH ELECTRODES OXIDIZED

Figure II-18.

confinement of the ions coming from the plasma boundary, thereby increasing the ion current and focusing it in the channel. Beam spreading behind the extraction channel is prevented by use of an ion condenser (Figure II-19), with the effect shown in Figure II-20. The increase of ion current by use of a transverse magnetic field is shown in Figure II-21 (Ref. 76).

The experimental technique proposed for use in the further extension of the present program is described further in Section IX of this report.

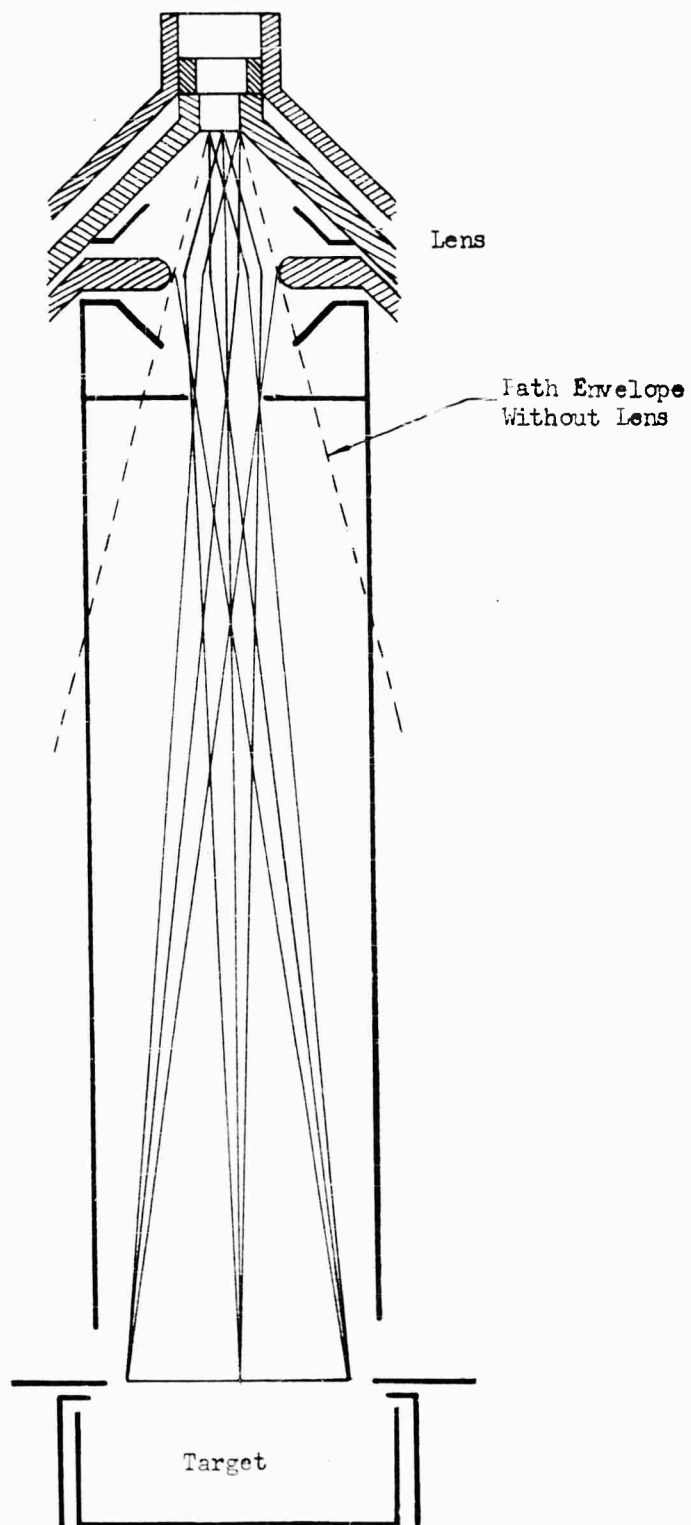
C. The Plasma Arc Source

The problem as previously cited is the ultimate production of a copious supply of heavy ions amenable to electrostatic acceleration.

The development of such an ion source and the evaluation of its performance requires that a number of basic problems in plasma physics be considered. The ionization, diffusion, and recombination processes in a plasma must be studied to obtain a suitable ion source. Additional problems involving plasma sheaths and ion optics are inherent in methods to extract ions from the source and to accelerate them. Fortunately considerable literature exists on ion source development for high energy accelerators, mass spectrographs, and, recently, the magnetic mirror fusion devices. It is readily apparent from this literature that the detailed processes in electric discharges are not completely understood. However, many useful experimental techniques have evolved and several types of ion sources have been produced which have been successful for their purpose.

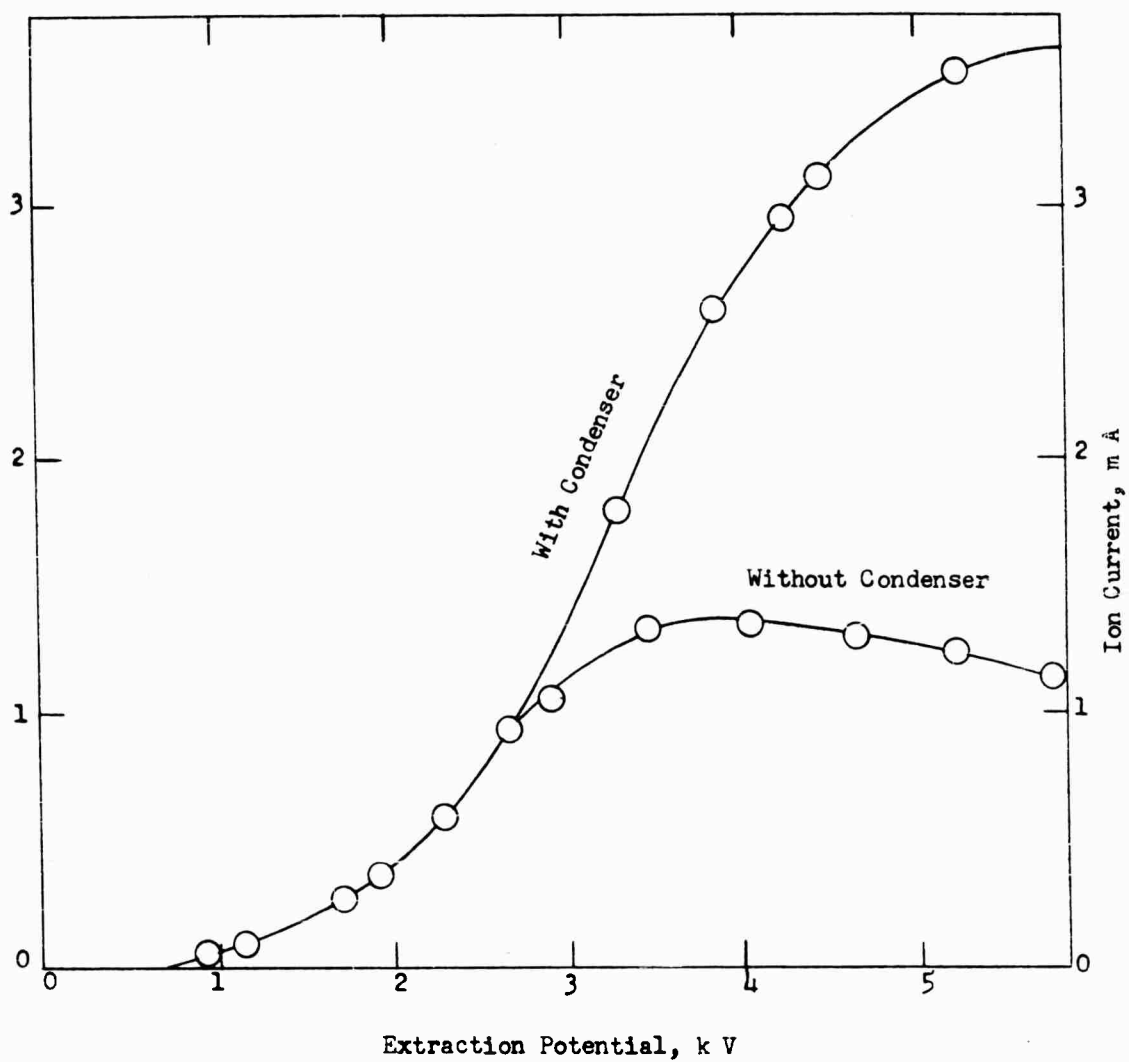
The ion source should be designed for the utmost in efficiency and dependability. An obvious parameter to be considered in determining the ion source efficiency is the ion current/source weight ratio. The total weight relating to source operation, however, is a complex consideration depending as it does on the power supply as well as source design. For the present, the emphasis will be placed on developing a larger ion current. It appears that the problem of power efficiency rests primarily with the prime power supply for the acceleration mechanism and for the overall device. The power used for ionization is negligible, even if the process is inefficient. Existing sources have a power efficiency on the order of 1%. Cesium ions requiring 3.87 eV for ionization and subsequently accelerated to at least 10 keV energy could thus be used at about 96% efficiency (for the overall system) if no other losses were encountered.

Likewise the fuel waste involved in neutral atom loss must be analyzed in terms of the overall device weight. For each ampere



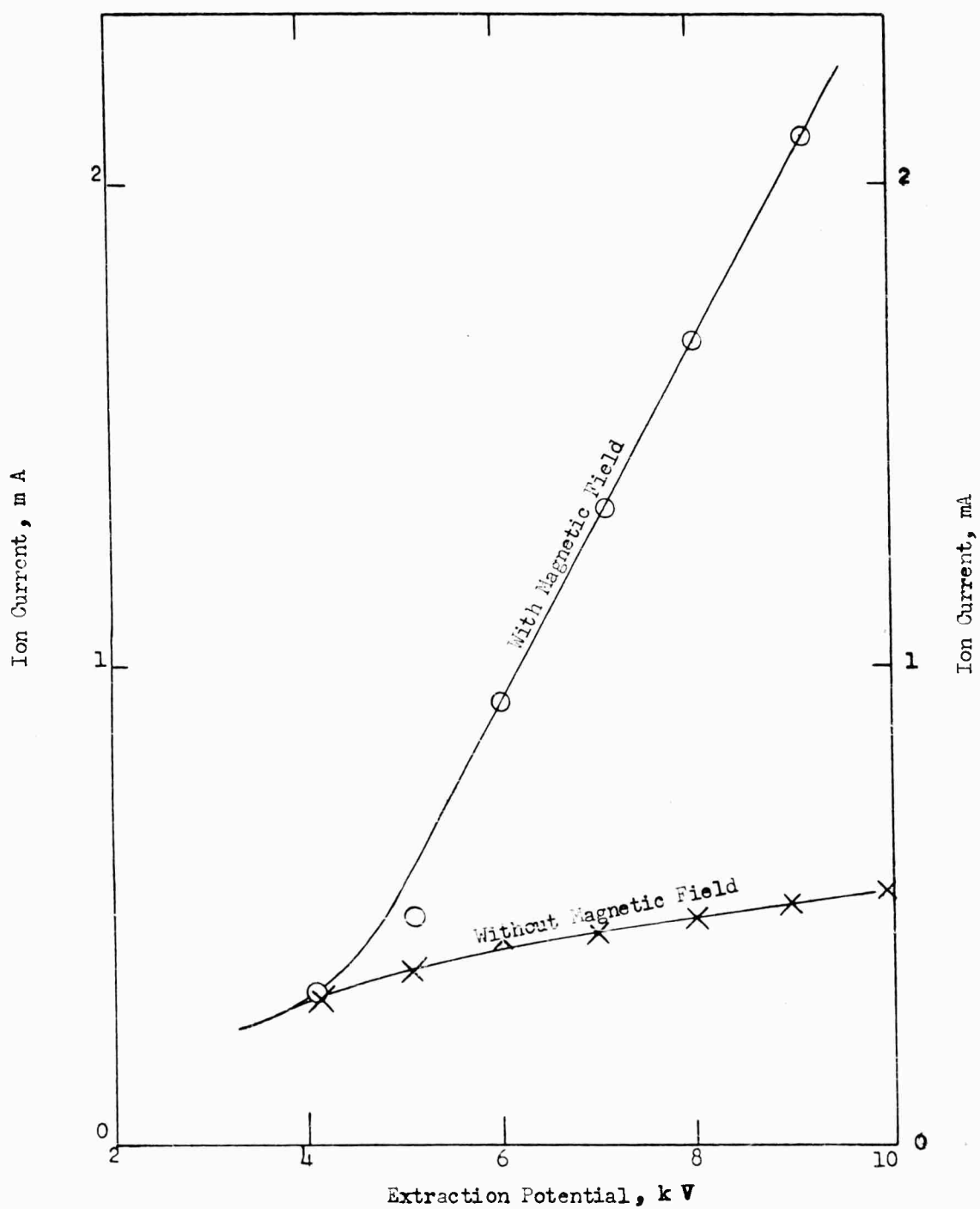
ION CONDENSER SYSTEM

Figure II-19



EFFECT OF ION CONDENSER

Figure II-20



EFFECT OF MAGNETIC FIELD
(TRANSVERSE)

Figure II-21

of ion current about 1 milligram/second of cesium would be ionized and ejected. Carrying a comparable amount of fuel to be wasted would probably not be a burden except for long-period operation. However, if these neutrals became ionized in the accelerating system, they would constitute a source of electrons which would parasitically load the power supply. A plasma sheath might also be established which would shield the ions from the accelerating field.

It appears that reliability should become a prime consideration in the ion source. Ease in starting the ion source, stability, and structural durability will be of crucial importance. In particular, those sources utilizing components subject to sputtering are not desirable. The choice of fuel should also be considered in this connection. The advantage of a low ionization potential for an element in a high temperature ion source may be overshadowed by the high chemical activity and the vapor condensation problems with an alkali metal. Experiments on the ionization of cesium will in any case be of interest.

A large number of ion sources in existence have been described recently by Von Ardenne (Ref. 47). The Duoplasmatron developed by Von Ardenne has excited considerable interest and this type of source is being tested at Oak Ridge National Laboratory and at Livermore for use in Project Sherwood fusion devices (Ref. 48 and 49). Von Ardenne's data for this source are as follows: maximum ion current, one ampere of protons with 7 ampere arc current at 120 volts and extraction aperture of 1 mm diameter. The power efficiency in the ionization process was thus about 1.5%. As far as can be determined investigators in this country have experienced difficulty in improving on the results. Filament life continues to be a problem and backstreaming electrons and negative ions in the extractor region require special care if power loss and sputtering problems are to be avoided. An important feature of this arc is the magnetic and electrostatic compression which makes the ionization process especially efficient near the extractor.

The Oak Ridge and Livermore laboratories are working also on a hot cathode arc which is somewhat similar to the Duoplasmatron but requires several hundred amperes arc current. This source is also operated in a magnetic field, but does not utilize the compression features of the Duoplasmatron. Operation is on a pulsed basis with several amps beam current extracted at the anode for use with the magnetic mirror fusion device (Ref. 50).

A similar grid ion source has been developed at Oak Ridge for continuous operation.

A DCX type arc developed at Oak Ridge has been suggested as a powerful ion source (Ref. 51). Observation of 20 amperes of backstreaming ions which strike the cathode has been interpreted to mean that electric fields exist within the arc and accelerate the ions to the cathode sheath. This observation is in agreement with the theory of positive ion collection by probes which shows that the ions should arrive at the probe sheath with an energy of about $1/2 kT_e$ (Ref. 52). The ion temperature of the arc measures from 10 ev to 50 ev and the drift energy of the ions toward the cathode is about 2 ev (Ref. 53). The arc current was 300 amperes.

It had originally been proposed in the present program to conduct experiments on the gas-stabilized plasma arc seeded with cesium to ascertain its capabilities as an ion source. The preceding discussion has indicated the considerable effort currently being expended by the AEC on arc devices and the high ion current densities which can be obtained. In Section X of the present report several proposed experimental arc devices are described. In addition, the methods of ion extraction and diagnostics are discussed.

III. TYPES OF CONTACT EMITTERS

The various types of emitter procured for use in the investigation of surface ionization are described. Mr. H. Szymanowski was responsible for the mechanical design and procurement of the emitters, assisted in the specification by Dr. O. Husmann and Dr. E. Petrick.

III. TYPES OF CONTACT EMITTERS

Three types of contact emitters were procured for evaluation. In each case, the cesium vapor is passed through the emitter. In order to provide maximum ionization efficiency, the use of (relatively) large mesh screens and grids had been ruled out, by the same reasoning as applied to the effort in this program in eliminating by-pass flow around the edges of the emitter.

Emitters with the smallest possible flow passages were obtained, including porous tungsten plates, platinum screens, and molybdenum screens. The specifications are given below.

A. Porous Sintered Tungsten

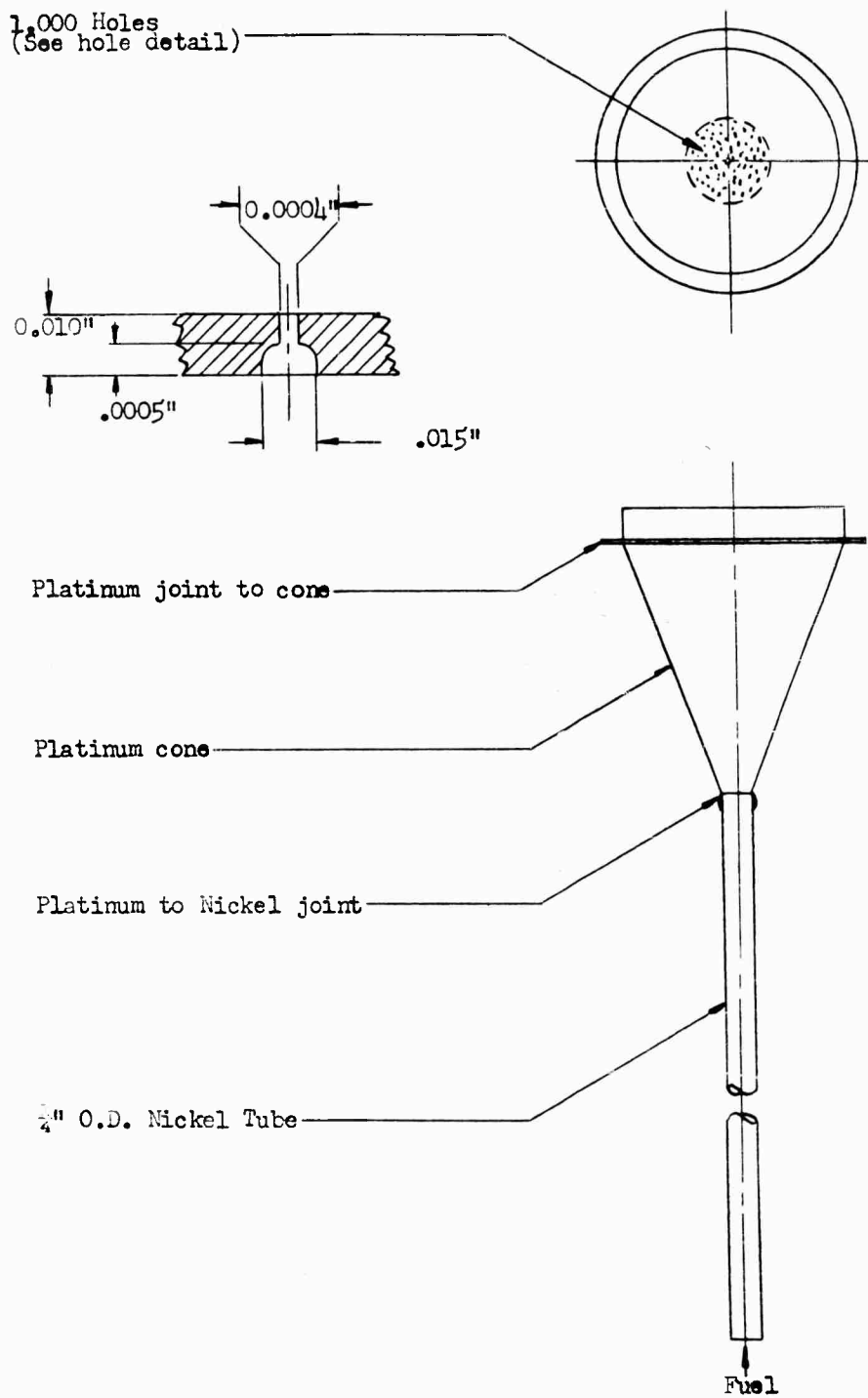
Items	Plate Thickness(in.)	Powder Size(Microns)	Apparent Density(%)	Porous Volume(%)	Sintering Temp.(°K)
F-1	.050	4.0-5.0	58	42	1700
F-2	.030	4.0-5.0	58	42	1700
C-1	.004 .104	6.0-7.0	52	48	1725
P-1	.060	0.5-10.0	83	17	2675
P-2	.040	0.5-10.0	83	17	2675
P-3	.020	0.5-10.0	83	17	2675

In the series of tests reported herein, the evaluation included Items F-1, F-2, C-1, P-1 and P-2. These were considered sufficient to provide an initial evaluation of plate types and the effect on performance. Time did not permit tests of all of the porous tungsten plates listed above.

As described later in Section VI of this report, another type of emitter made by sintering a porous tungsten plate directly into a tungsten holder has been investigated, as a means of eliminating the bonding problem. Photographs and further information on the latter emitter are presented in that section.

B. Mechanically Perforated Platinum Screen

The platinum screen was obtained in the form of a complete "spinerette," the general shape and form being similar to that used as a commercial spinerette for forming viscous rayon and artificial fibers. A sketch of the configuration is shown in Figure III-1. As can be seen from



PLATINUM EMITTER

Figure III-1

this sketch, 1000 holes are punched into the center of the emitter plate. In order to keep the diameter of each hole as small as possible it was decided not to polish the outer surface of the emitter, thus leaving a rough ring around each of the punched holes and reducing the apparent diameter of the holes from a nominal 0.001 in. to approximately 0.0004 in. As may be seen on the inset in Figure III-1, the actual holes through the platinum are not direct but rather bell-shaped, with the small punched hole leading from the apex of the bell to the emitter surface. The prime advantage of this fabrication is that the complete assembly is made from platinum with platinum-fused joints. Leakage is not a problem. Gaseous diffusion experiments were conducted on the emitter; cesium ionization tests were not made during this first contract period.

C. Electro-Formed Molybdenum Screen

Several types of screens were considered for application to the ion source. The conventional woven screen appeared to provide too large a variation in the size of openings, even though the size of openings can be reduced by mechanical rolling.

An electro-etched tungsten screen with uniform hole sizes could have been obtained, but the minimum hole size is 0.005 in., which is considered somewhat large. Therefore, an electro-formed screen made of molybdenum was procured; a photograph of the screen is given in Figure III-2. The screen is 0.001 in. thick, with a solid rim for bonding into a holder. The holes, which are 0.003 in. in diameter located on 0.010-inch centers, are remarkably uniform in size. Additional screens of the same type can be obtained, with hole sizes of 0.0015-inch diameter.



Photograph of Molybdenum Screen

FIGURE III-2

IV. DIFFUSION EXPERIMENTS

The apparatus and the results of diffusion experiments are described in this section. Excellent agreement is shown for flow rate as a function of $T^{-1/2}$, where T is plate temperature. Correlation between diffusion data and measured ion current (as described later in Section V) is demonstrated. The experiments indicate that the effect of surface flow for the tested specimens and operating conditions can be considered to be minor.

The experiments were conducted by Dr. O. Husmann, with the assistance of Mr. B. Houck, laboratory technician.

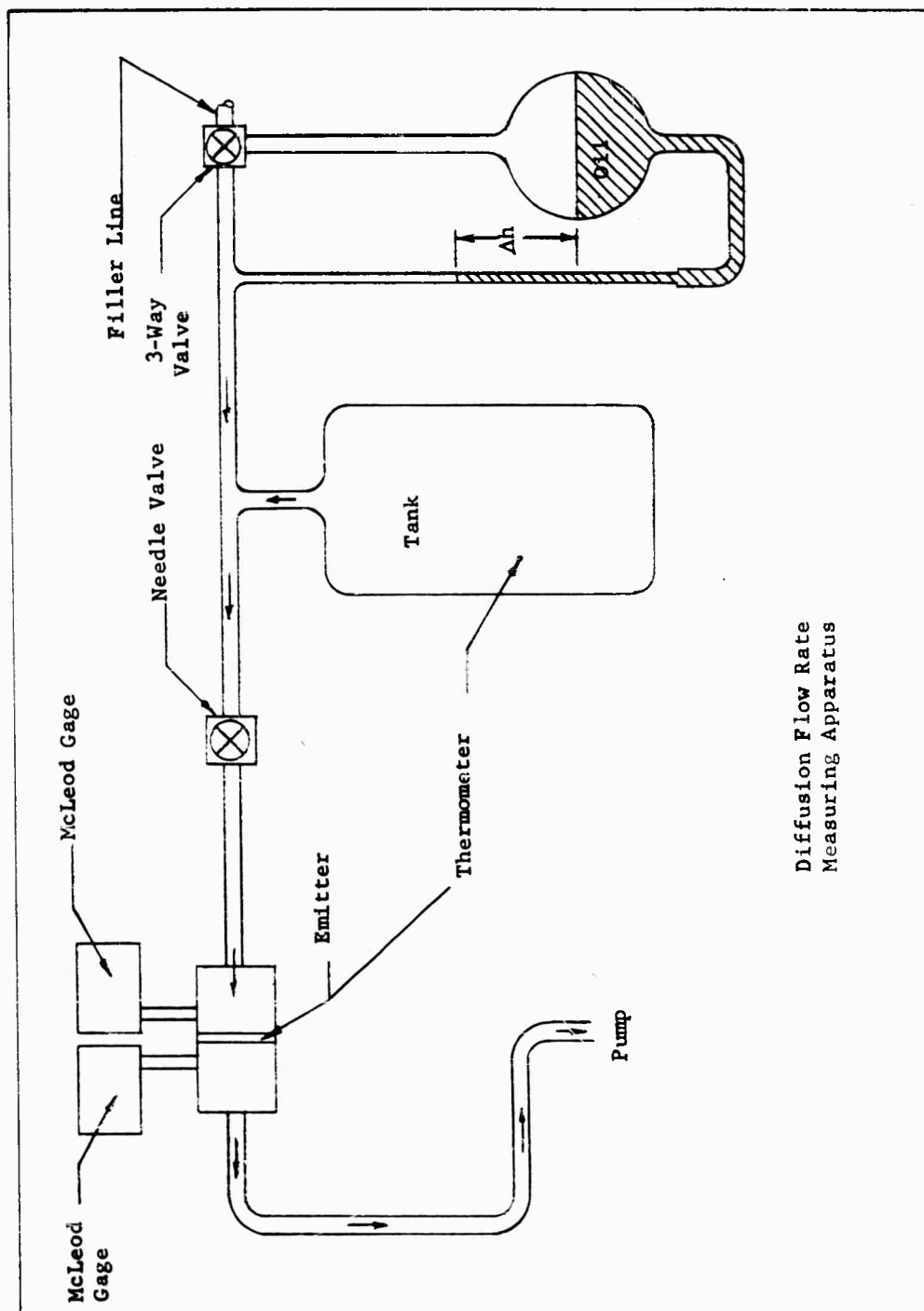
IV. DIFFUSION EXPERIMENTS

The diffusion flow mechanism was described earlier in Section II of the present report. Comparison of the porous emitter with a bundle of capillaries, as indicated therein, cannot be completely correct because the shape of the pores is variable; furthermore, the pores are interconnected. Recently E. E. Petersen (Ref. 66) and A. S. Michaels (Ref. 67) utilized a model to compute the diffusion through a porous body. The mean capillary diameter and the effective capillary length depend upon the powder size, the powder shape, the plate density, and the plate dimensions. In addition, consolidation of the powder may affect the flow rate, particularly when large powder areas are welded together. It should be noted that the consolidation effect may be negligible for spherical grains because the contact areas, in case of no deformation, are a minimum.

The experimental apparatus being used to measure the diffusion flow rate through a porous plate is shown in Figures IV-1. From right to left can be seen the pressure deflection meter, a gas container with fixed volume, and a needle valve connected to the porous plate for flow control. On the other side of the porous plate, the container is attached to a vacuum pumping system. McLeod pressure gauges are located on both sides of the porous plate.

As indicated earlier in Section II, flow rates in the molecular flow range and surface flow range appear to be of most interest. An estimate of the fuel evaporation rate (for 0.3% surface coverage of the exchange surface) for cesium, rubidium, and potassium can be made using the extrapolated lifetimes given by Knauer (l.c.), and also for rubidium by Hughes (l.c.). Extrapolation of Knauer's data for cesium gives an evaporation rate of approximately 10 amps/cm² for singly charged particles at 2000°K. The data of Knauer were taken at temperatures in the range of 1400°K, therefore this extrapolation may be optimistic. If we assume a maximum current density of 1 amp/cm², we are still far above the current densities published to date for charge exchange systems. The fuel flow through the porous plate at this high flow rate is in the molecular flow range, if the effective pore length and if the degree of consolidation are moderate. As indicated in Section II, in the molecular flow range the flow rate per unit area decreases with r , but on the other hand the fuel vapor pressure upper limit increases with $1/r$.

For a given vapor pressure, the flow rate decreases as the plate thickness L is increased, therefore for increased L , larger pressures have to be applied and the flow range may change from molecular to slip flow. The flow rate measurements, described below, were made



Diffusion Flow Rate
Measuring Apparatus

Figure IV-1

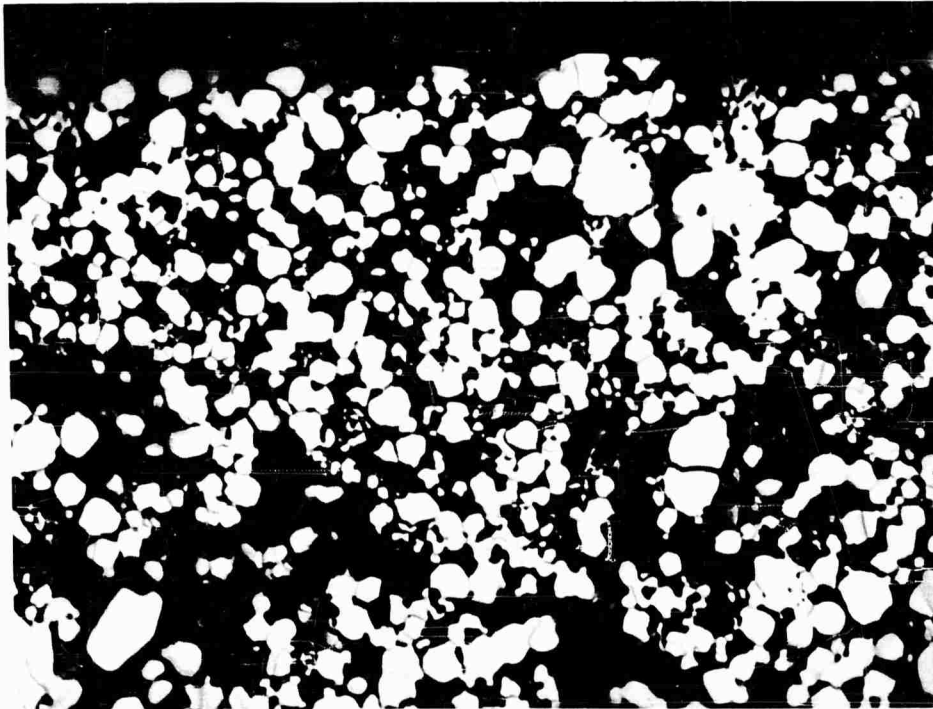
over a wide range of pressure to verify the flow regime. In the apparatus, the flow rate is measured by the change of gas pressure dp in the gas container (tank) as given by the oil level difference in the U-manometer.

Because of its low mass, helium was used initially in the experiments, followed in some cases by argon. In the molecular flow range the flow rate is a function of $1/M^{1/2}$, where M is the atomic or molecular weight, and of $1/T^{1/2}$, when the gas temperature is independent of the temperature T of the diffusion plate.

The porous plates tested were described previously in Section III. Before starting the flow rate measurements, however, statistical information was developed on the F-2 porous plate including the mean pore diameter and the isotropy of the pore distribution in three directions. Figures IV-2 and IV-3 show cross-sections of the F-2 plate perpendicular and parallel to the surface; Figure IV-4 is a cross-section of the more dense P-1 porous plate. For the F-2 plate, the number of holes of equal length (± 0.25 micron) were counted out in the range from 0.5 to 20 microns in 0.5 micron steps (TABLE IV-A). In each photograph, right-angle directions were counted independently. The result is shown in Figure IV-5. Of interest is the small deviation in the single counts, so that isotropic distribution of the holes can be assumed in the F material. Only the deviations of the 0.5 micron holes are greater, which may be due to the tolerance in the diameter. The number of counts per diameter is a maximum for the 0.5 micron holes and decreases at greater diameters.

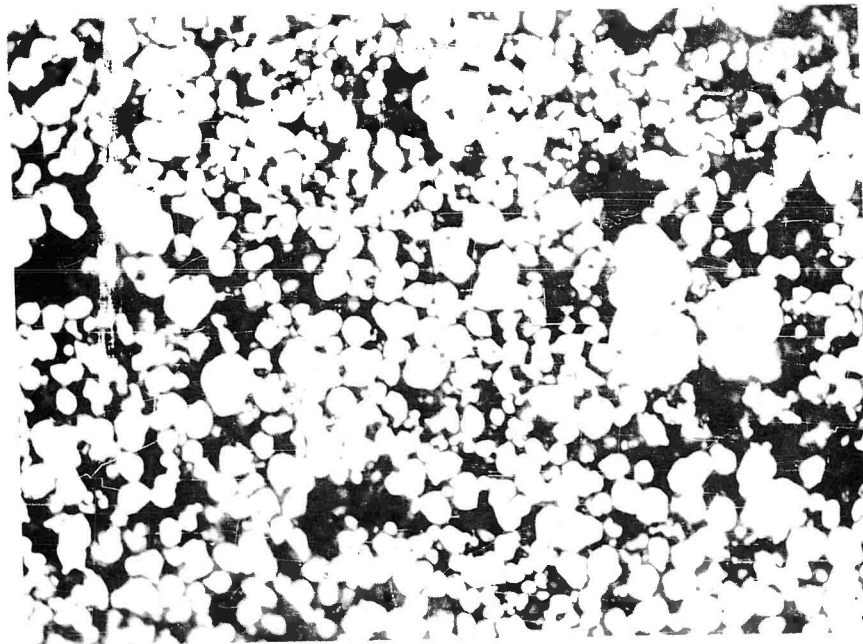
The measured mean pore diameter resulting from this statistical study when weighted with the statistical errors gives a value of about 5 microns as shown in TABLE IV-B. The total length of the holes to the total length of the traverses gives the percentage of porous volume. It is of considerable interest to note that the statistical value of volume, within the statistical error, agrees with the plate density value determined by weight tests.

Computations also have been made on a model of spherical grains of equal size, for three different kinds of package, to determine the pore diameters and the effective pore lengths. The least dense package has a porous (void) volume of 48%, the middle density 38%, and the most dense 26%. The effective length of path or the effective length of capillary also depends on the kind of package and is equal to the plate thickness in the case of the 48% porous volume plate, is increased to 1.23 L (with L as plate thickness) for the medium density, and is increased to 1.3 L for the most dense package. The mean capillary cross sections are $2.95 r^2$ for 48% porous volume, $2.1 r^2$ for 38%, and $1.2 r^2$ for 26%. Figure IV-6 gives for this model the number of capillaries per cm^2 , as a function of the mean pore radius. Figure IV-7 shows the relationship between the mean pore radius and the grain diameter for the three packages. Figure



Cross-Section of F-2 Porous Emitter, (1000X)
Perpendicular to Plate Surface
(Surface of Plate is Shown at Top of Photograph)

FIGURE IV-2



Cross-Section of F-2 Porous Emitter (1000X)
Parallel to Plate Surface

FIGURE IV-3



M-1085

Cross-Section of F-1 Porous Emitter (1000X)

FIGURE IV-4

TABLE IV-A. PORE SIZE COUNT

FLAT						SECTION					
Microns	#1	#2	#1	#2	Σn	Microns	#1	#2	#1	#2	Σ
x	+	o	o	Δ	*	x	+	o	o	Δ	*
0.5	50	134	83	150	417	10.5	3	2	2	1	8
1.0	65	81	69	54	269	11.0	2	2	2	2	8
1.5	54	65	59	60	238	11.5		1			1
2.0	56	55	44	41	196	12.0	1		3		4
2.5	18	35	19	46	118	12.5	2				2
3.0	28	35	28	21	112	13.0					
3.5	19	19	18	12	68	13.5					
4.0	21	15	17	11	64	14.0			2		2
4.5	9	9	8	12	38	14.5			1		1
5.0	19	8	8	13	48	15.0	1				1
5.5	7	7	2	7	23	15.5					
6.0	11	14	8	2	35	16.0			1		1
6.5	6	5	4	4	19	16.5			1	2	3
7.0	7	2	3	5	17	17.0	1				1
7.5	3	5	2	6	16	17.5					
8.0	7	1	1	6	15	18.0	1				1
8.5	1	6	-	2	9	18.5					
9.0	3	6	1	-	10	19.0		1			1
9.5	1	1	1	3	6	19.5					
10.0	6	3	1	1	11	20.0		1		1	2
POROUS TUNGSTEN PLATE, F2 .030in. THICK Original data taken from measurements on 1000 x, microphotographs Numbers in body of table (n) are counts of holes "x" microns long						20.5					
						21.0	1				1
						21.5					
						22.0	1				1
						22.5					
						23.0					
						404	513	388	462	1767	
						110	125	95	130		
						LENGTH EACH LINE - MICRONS					

ORIGINAL READINGS

(Traverses #1 & #2 taken at right
angles to each other on the
same photograph)

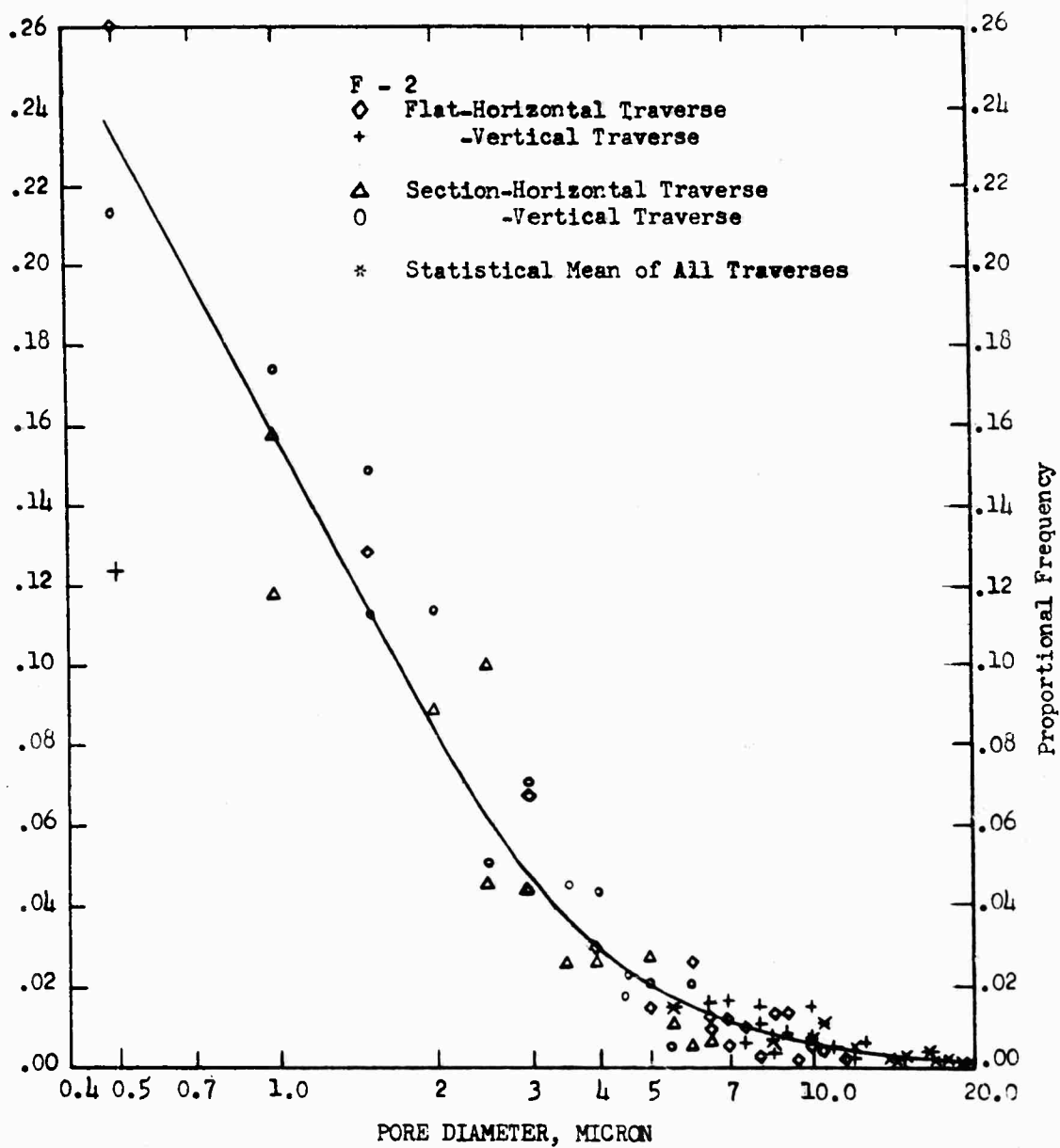


Figure IV-5.

PROPORTIONAL FREQUENCY OF VOID SIZES

TABLE IV-B. MEAN PORE DIAMETER

FLAT						SECTION					
Microns	#1	#2	#1	#2	Σ	Microns	#1	#2	#1	#2	Σ
x	+	◇	o	Δ	*	x	+	◇	o	Δ	*
0.5	3.535	5.788	4.555	6.123	10.210	1.05	18.186	14.847	14.847	10.500	29.694
1.0	8.062	9.000	8.307	7.348	16.401	1.10	15.534	15.534	15.534	15.854	31.108
1.5	11.022	12.093	11.521	11.619	23.140	1.15		11.500			11.500
2.0	14.966	19.852	13.266	12.806	28.000	1.20	12.000			20.784	24.000
2.5	10.607	19.790	10.898	16.355	27.157	1.25	17.675				17.675
3.0	15.873	17.748	15.873	13.749	31.749	1.30					
3.5	15.257	15.256	19.851	12.124	28.861	1.35					
4.0	18.332	15.492	16.492	13.268	32.000	1.40				19.796	19.796
4.5	15.500	13.500	12.726	15.588	27.738	1.45				14.500	14.500
5.0	21.795	14.140	14.140	18.030	39.640	1.50	15.000				15.000
5.5	14.553	14.553	7.777	14.553	26.378	1.55					
6.0	19.902	22.452	16.968	8.484	35.496	1.60				16.000	16.000
6.5	15.918	14.534	13.000	13.000	28.334	1.65				16.500	23.331
7.0	18.522	9.898	12.124	15.652	28.861	1.70	17.000				17.000
7.5	12.990	16.770	10.605	18.368	30.000	1.75					
8.0	21.168	8.000	8.000	19.592	30.984	1.80	18.000				18.000
8.5	8.500	20.816	-	12.019	25.500	1.85					
9.0	15.588	22.041	9.000	-	28.458	1.90		19.000			19.000
9.5	9.500	9.500	9.500	16.454	22.266	1.95					
10.0	24.490	17.320	10.000	10.000	33.170	20.00		20.000		20.000	28.280
POROUS TUNGSTEN PLATE, F2 .030 in. THICK 1000 x PHOTO SUMMATION OF $x\sqrt{n}$ Body of table gives $x\sqrt{n}$ with n and x both taken from table IV A						20.50					
						21.00	21.000				21.000
						21.50					
						22.00	22.000				22.000
						22.50					
						23.00					
						$\Sigma(\Sigma x\sqrt{n})$	450.435	369.924	337.584	325.117	883.474
						$\Sigma\sqrt{n}$	87.976	88.678	77.765	90.128	178.658
						$\Sigma(\Sigma\sqrt{n})/\Sigma\sqrt{n}$	5.121	4.171	4.212	3.607	4.945
						STATISTICAL MEAN DIA.					

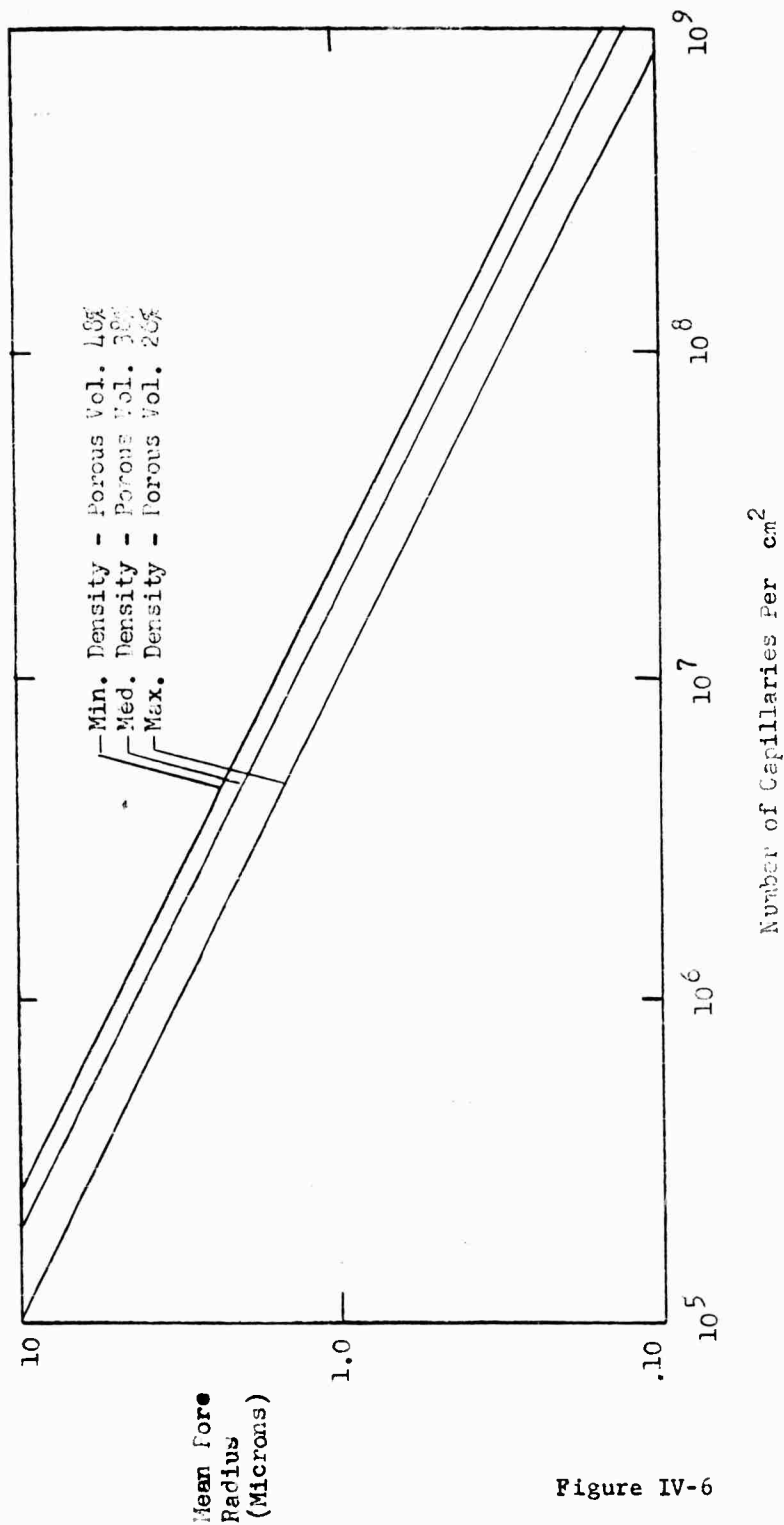


Figure IV-6

THEORETICAL POROUS PLATE MODEL, WITH UNIFORM SPHERICAL GRAINS

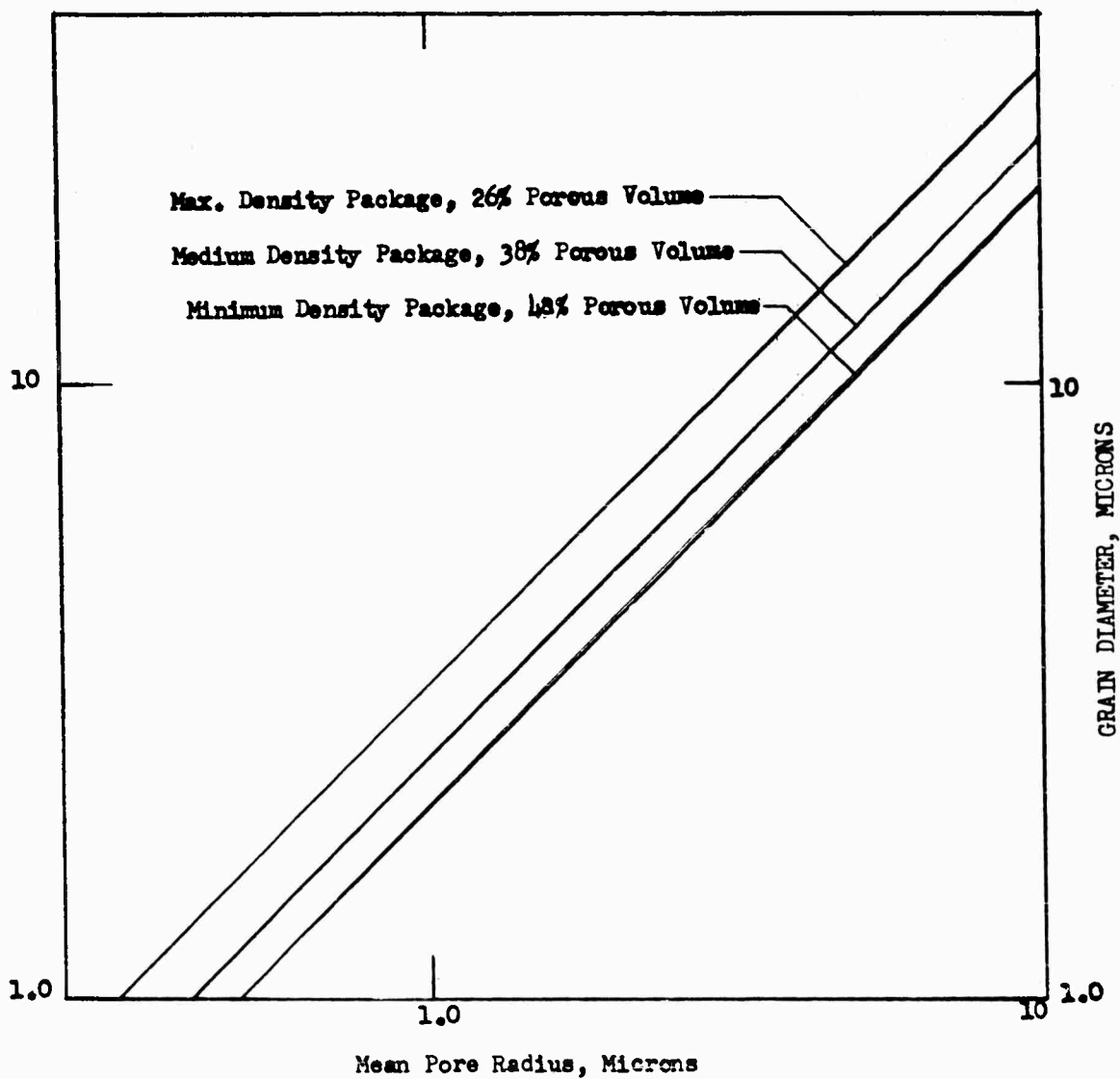


Figure IV-7

MEAN PORE RADIUS VERSUS GRAIN DIAMETER FOR
THEORETICAL MODEL WITH UNIFORM SPHERICAL GRAIN

IV-8 shows the flow rate in amps/cm^2 for the three models dependent on the mean capillary radius "r", with C_8 as fuel. Figure IV-9 gives the flow rate again in amps/cm^2 as a function of the porous volume with the mean pore radius as a parameter.

The aforesaid model was used for comparison purposes with the measured flow rates of the three tested porous plates.

A less complicated assumption is the use of a bundle of capillaries instead of a porous plate. Figure IV-10 presents the flow rate in amps/cm^2 for such a bundle as a function of the vapor mass, and Figure IV-11 gives the flow rate through a bundle of capillaries as function of the pore radius. Depending on the two possible kinds of package the porous volumes are 90.7% and 75.8%.

TABLE IV-C. SOME GAS PROPERTIES

Gas	M (gr)	Molecular diameter (cm)	Viscosity	Sutherland Const. 20 to 100°C
Helium	4.003	$2.18(10^{-8})$	$1.8(10^{-4})$	73
Argon	39.94	$3.66(10^{-8})$	$2.11(10^{-4})$	148
Xenon	131.3	$4.88(10^{-8})$	$2.11(10^{-4})$	250

In making the flow rate measurements with the apparatus of Figure IV-1, the pressure on one side of the porous plate is adjusted with the needle valve. The flow rate is measured by dh , the change of the oil level in the U-manometer, as a function of time. TABLE IV-C above shows physical data for the gases used and also for xenon, which is close in weight to cesium.

Platinum Screen Test Results

The diffusion experiments were started with Pt - screen (spinnerette), in which 1000 holes had been punched. The flow rates, TABLE IV-D, agree well with the expected flow rates after cleaning the plate by preheating under vacuum conditions.

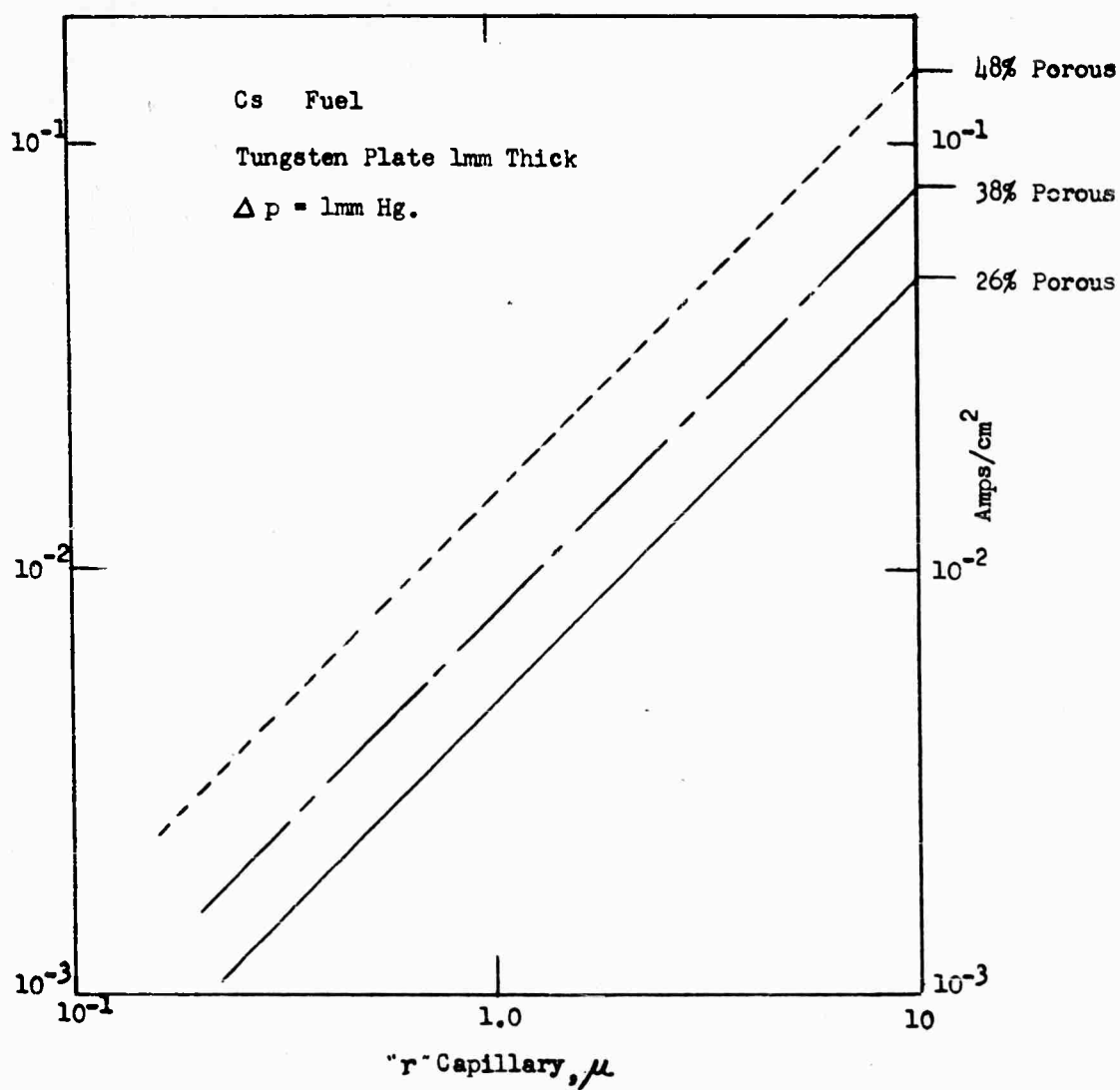
TABLE IV-D. PLATINUM SCREEN DIFFUSION RESULTS

~~Maximum mean free path 20 μ~~

P_{max} (argon) 1.9mm Hg

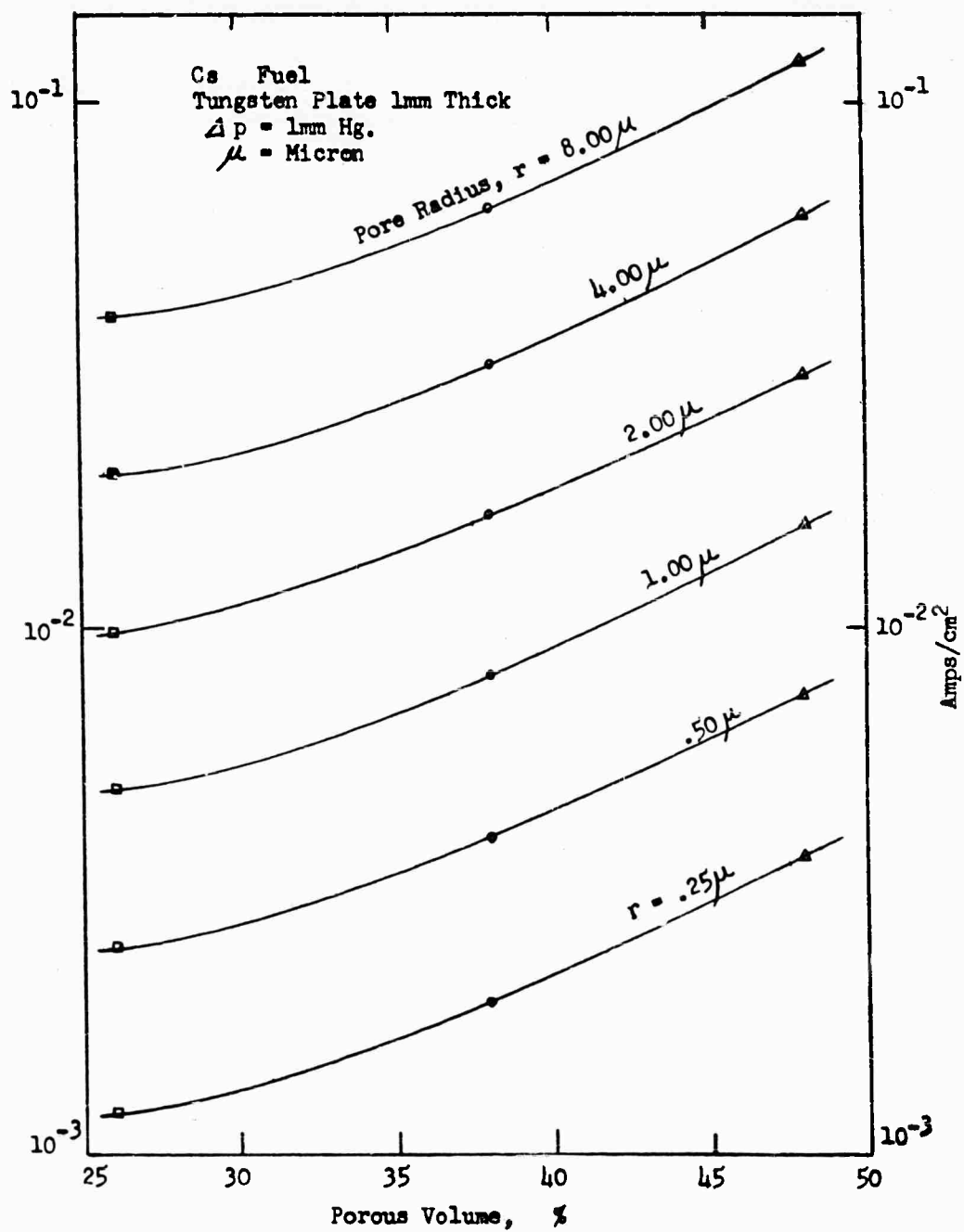
Clausing factor 1.27

P_{max} (He) 5.3mm Hg; P_2 in micron range



THEORETICAL FLOW IN AMPS PER cm^2 IN
 MODEL PLATE AS A FUNCTION OF PORE RADIUS

Figure IV-8



THEORETICAL FLOW IN AMPS PER cm^2 IN
 MODEL PLATE AS A FUNCTION OF POROUS VOLUME

Figure IV-9

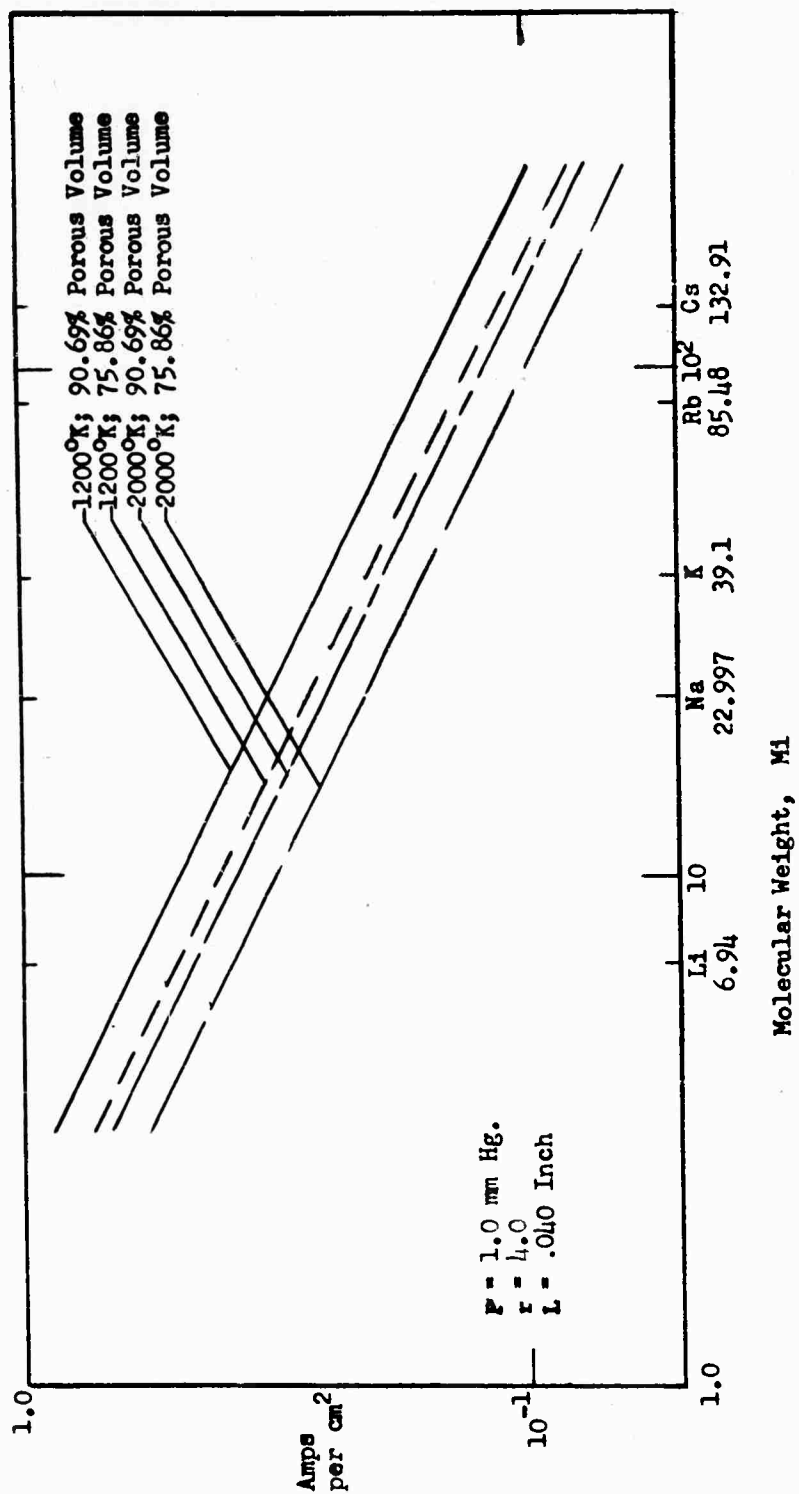
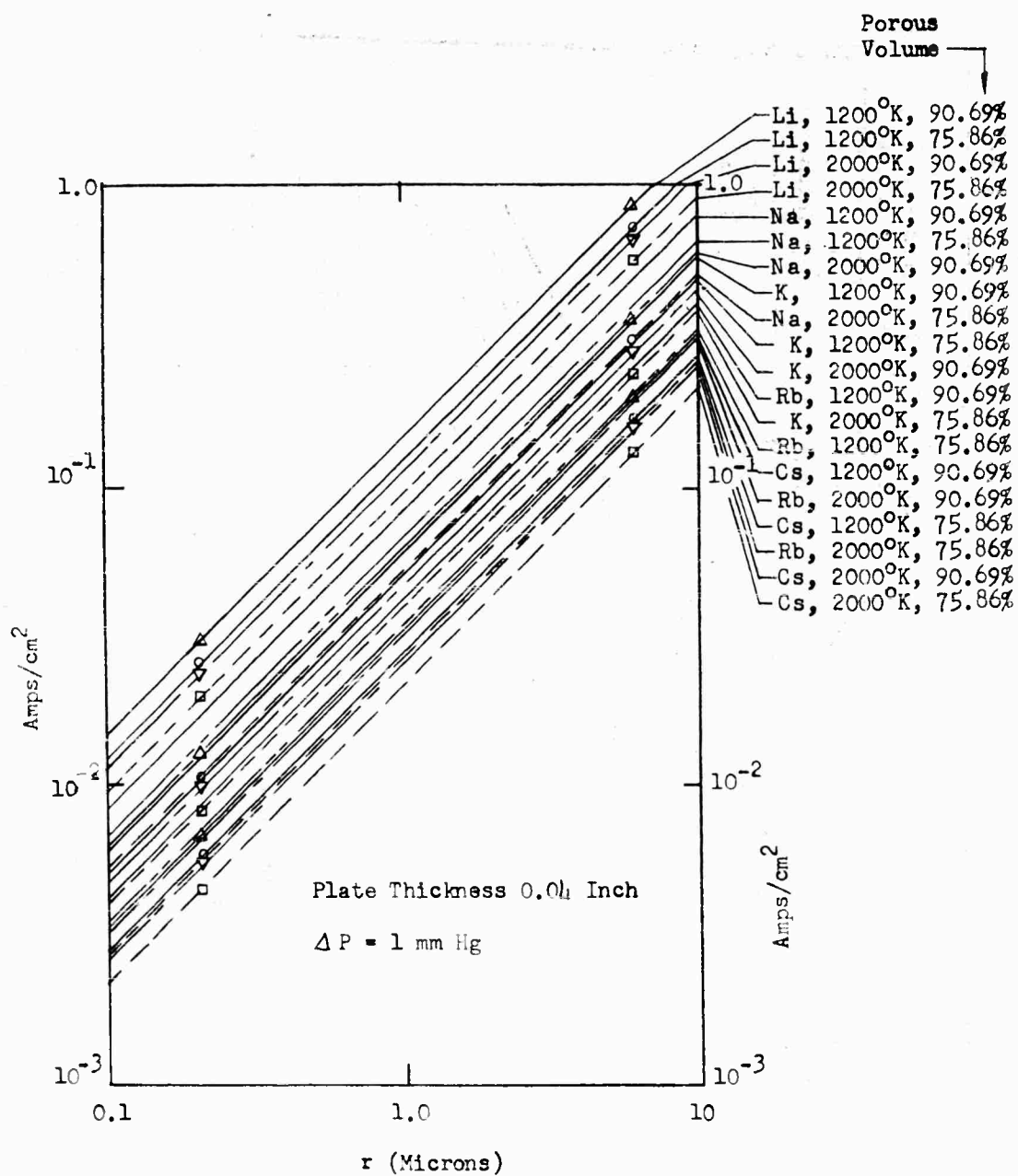


Figure IV-10

MOLECULAR FLOW RATE THROUGH A BUNDLE OF CAPILLARIES
AS A FUNCTION OF MOLECULAR WEIGHT



MOLECULAR FLOW RATE THROUGH A BUNDLE OF CAPILLARIES
 AS A FUNCTION OF PORE RADIUS

Figure IV-11

Gas	dp (mm Hg)	Plate Temp. °K	Vg (cm ³ /10 Min) at 760 mm Hg, 0°C	Remarks
Argon	16.3	296	38.9	Before Outgassing
Argon	14.75	300	72.5	After Outgassing
Argon	1.4	1033	4.5	
Argon	1.2	1273	4.4	
Argon	1.25	296	7.8	
Helium	3.37	298.5	65.2	

As TABLE IV-D shows, the flow rate before outgassing was about half of the measured value after heating. Since the capillary length is not much greater than its diameter, a correction factor (Clausing factor) must be applied, as given in TABLE IV-E.

TABLE IV-E. CLAUSING FACTOR, f

$4L/r = \infty$	f = 1.00
20	1.35
16	1.44
12	1.58
8	1.86
4	2.60

where L is capillary length
and r is capillary radius.

Figures IV-12 and IV-13 show that the $1/T^{1/2}$ and the $1/M^{1/2}$ laws are followed. In Figure IV-12 the flow rate is shown versus the vapor pressure.

Moly Screen Test Results

Measurements with the molybdenum screen do not agree as well with theory as the previous platinum screen. Data is given in TABLE IV-F.

TABLE IV-F. MOLYBDENUM SCREEN FLOW TESTS

1680 holes per cm ²	Surface area, 3.01 cm ²	
Total number of holes, 5055	Hole length, 25 u	P _{max} (He) 1.9mm Hg.
Hole diameter, 67 u to 72 u		

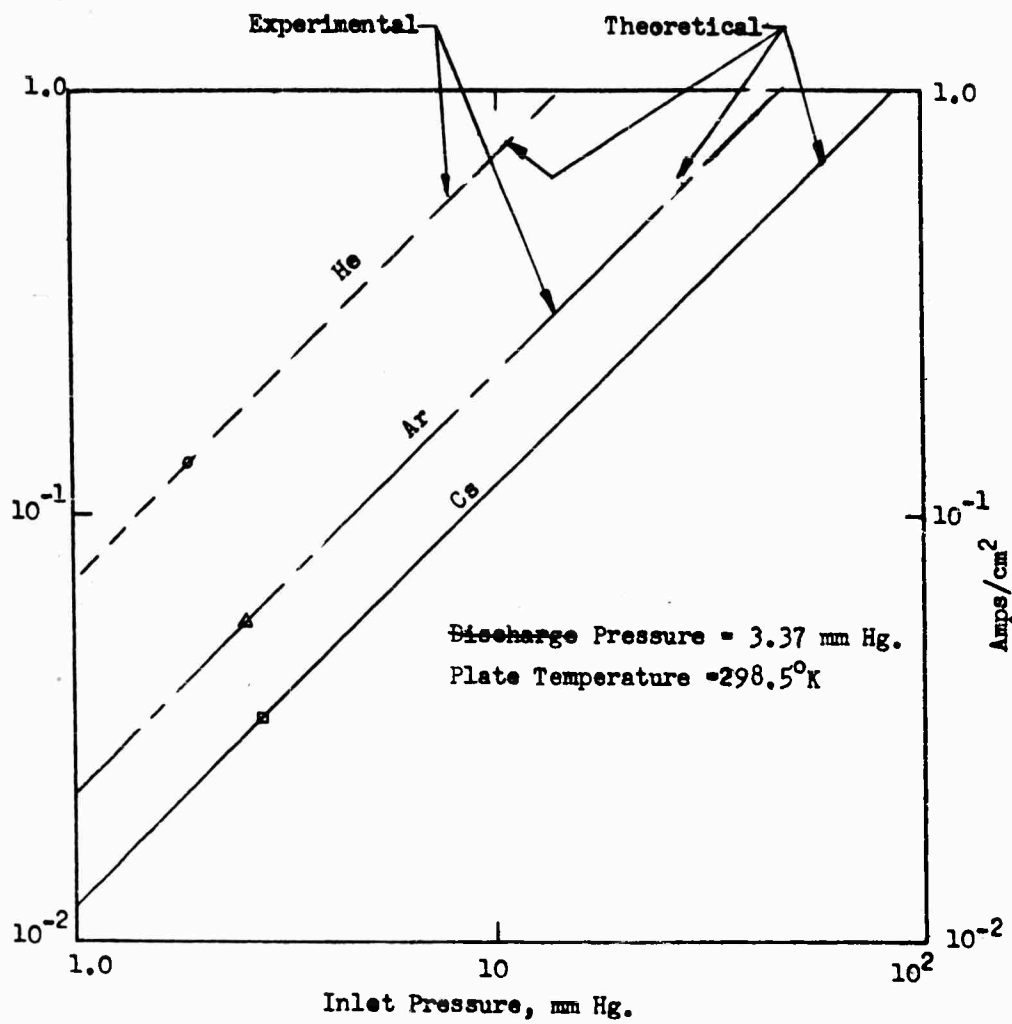


Figure IV-12.

EXPERIMENTAL AND THEORETICAL DIFFUSION FLOW
FOR PLATINUM SCREEN

P_{max} (Argon) = 1.9 mm Hg.
 P_{max} (He) = 5.35 mm Hg.

— Argon Measured.
 - - - Helium Measured.
 - - - He: Theoretical value
 with Clausius
 correction

} 1 mm Hg.

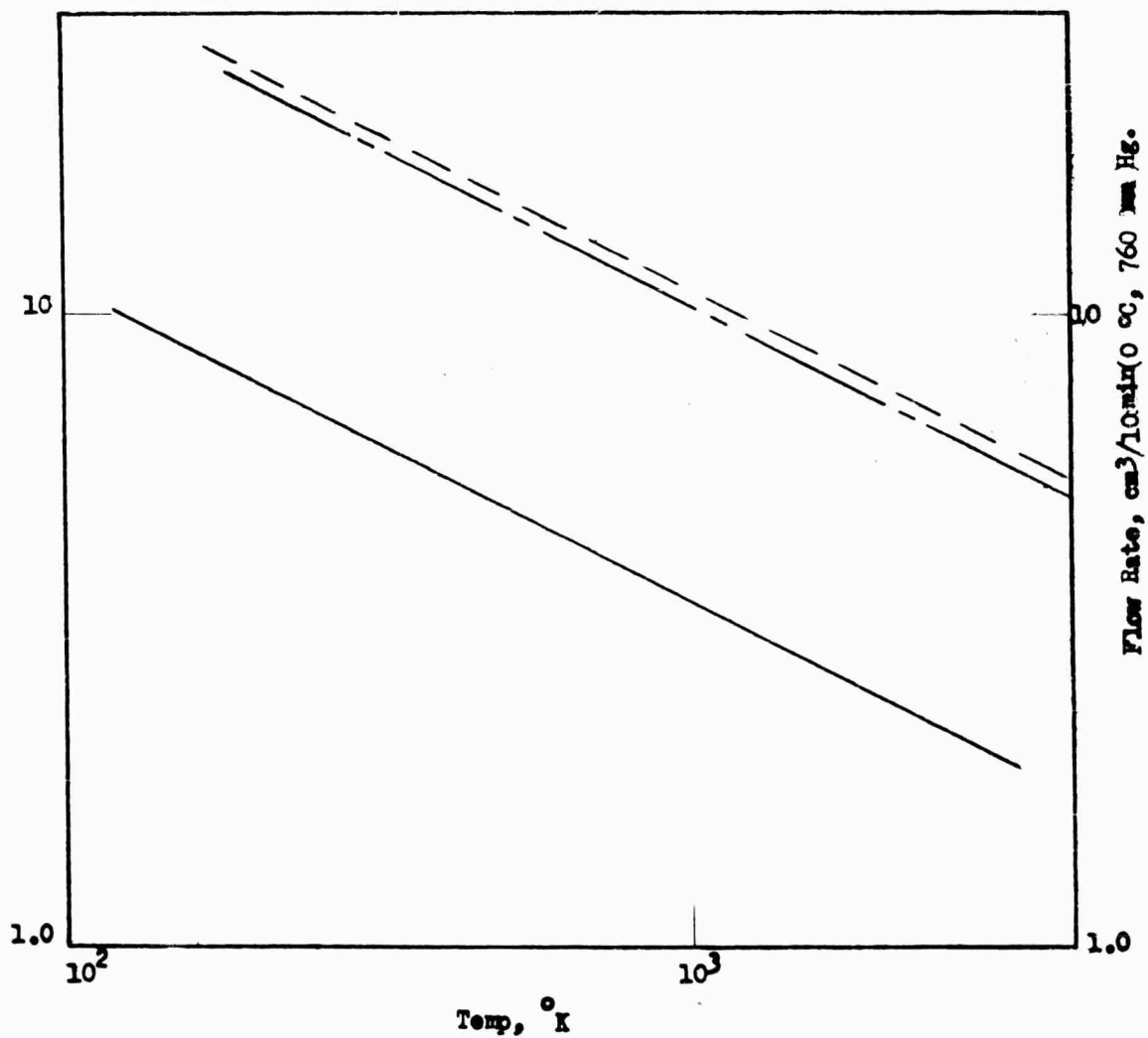


Figure IV-13.

PLATINUM SCREEN DIFFUSION FLOW AS A
 FUNCTION OF SCREEN TEMPERATURE

Gas	dp (mm Hg)	Plate Temp. °K	Vg (cm ³ /Min) per cm ² - mm Hg at 760 mm Hg, 0°C
He	0.7	293	40.6
He	0.7	293	40.0 (After outgassing at 900°K)
He	0.7	293	43.0 (After outgassing at 900°K)

The measured flow rate per capillary is smaller than the computed (Figure IV-14) value for capillaries of 68 u diameter and 25 u length. The measured flow rate corresponds to a capillary of 50 u diameter. The main reason may have been due to partial clogging of some holes.

Porous Tungsten Plate Results

TABLE IV-G gives values of the flow rate measurements with the P-2 0.040 in. porous plate, 17% porous volume.

TABLE IV-G. FLOW TEST OF P-2 TUNGSTEN PLATE

Porous Volume: 17%	Surface Area 1.138 cm ² (later investigation showed that the surface had been partially covered with what appeared to be Ni - see remarks below).
Plate Thickness: 0.040 in.	
Plate mechanically bonded into nickel holder tube.	

Gas	dp (mm Hg)	Plate Temp. °K	Vg (cm ³ /min)
He	16	308	0.865
He	14	1305	0.795
He	27	297	2.14
He	33	1393	3.09
He	30.5	795	1.7
He	27.8	489	1.595
He	28.5	296	1.66
He	13	296	0.722
He	12	873	0.436
He	10	1233	0.436
He	14.1	292	0.99
He	36.3	292	3.46
He	39.5	1183	2.84
He	36	1183	2.64

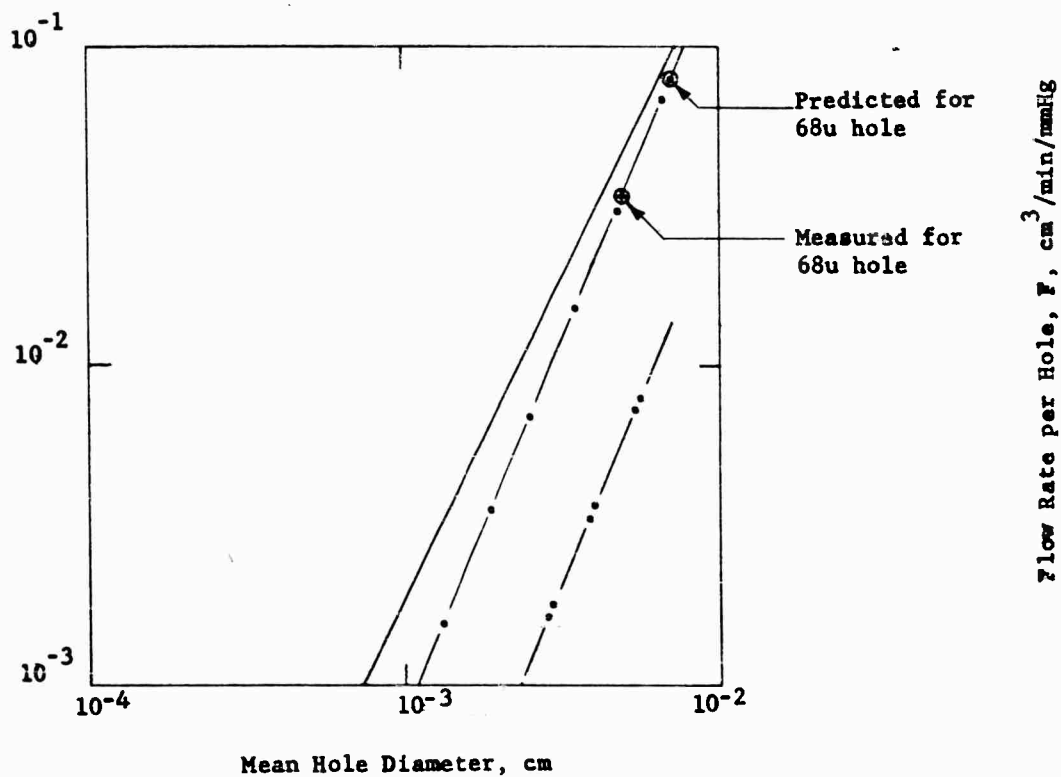
After the flow rates had been measured, a microscopic investigation of the plate surfaces showed one side as much as 90% covered with what appeared to be a nickel material. The flow did not increase in proportion

————— Orifice
 — . — . — Capillary with $L = 2.5 \times 10^{-4}$ cm
 — .. — .. — Calculated Cs Flow Rate per Hole

$$F^* = (22.8) (10^2) (A)$$

$$F = (22.8) (10^2) \frac{A}{17 \frac{3}{16} L \frac{C}{A}}$$

where F = flow rate
 A = surface area
 C = circumference



FLOW RATE FOR MOLYBDENUM SCREEN

Figure IV-14

to pressure, as expected, but changed to some extent independent of pressure. Bypassing of part of the gas between the porous plate and the molybdenum holder tube is a tentative explanation. Therefore the expected temperature slope is not well confirmed (Figure IV-15). The computed slope for cesium is included.

Duplication of the test using the P-1 plate again showed what appeared to be a clogging effect. This clogging was not immediate but appeared after about two hours operation of P-1 at 1500K plate temperature (using a platinum-bonded plate). As described later in Section VI, the P-series of plates are undergoing further examination to establish the cause of the reduction in flow rate. The measured flow was only 38% of the predicted value.

TABLE IV-H gives the flow rate data for the F-1 porous plate; Figures IV-16 and IV-17 show the corresponding fuel flow rates depending on the gas pressure. In contrast to the statistical investigation, the mean hole diameter appears to be far smaller, i.e., 0.51 μ . As indicated previously, a porous plate of spherical grains would be expected to show no consolidation. The considerable experimental deviation from the predicted flow rate (based upon the statistically-measured mean hole diameter described earlier in this section) is attributed to consolidation of the obviously non-spherical grains in the actual test plate.

The plate showed considerable shrinkage after heating as shown in Figures IV-16 and IV-18. Because the plate had been brazed to a molybdenum tube, no bypass leakage was observed. Figure IV-18 shows this flow rate before and after heating. The $1/T^{3/2}$ slope is well established.

TABLE IV-H. FLOW DATA FOR F-1 POROUS PLATE

F-1 --- 0.050 in. Porous Tungsten Plate --- Surface Area 0.798 cm^2
Porous Volume 42.2%

Measurements after outgassing at 990°C

Gas	dp (mm Hg)	Plate Temp. $^{\circ}\text{K}$	Vg (cm^3/min)	Remarks
He	19.9	293	11.98	
He	13.45	1028	4.31	
He	12.6	1263	4.05	
He	19.0	1038	6.44	
He	5.0	1268	1.375	
He	10.5	299	5.18	After heating at 1033°K for 215 minutes.
Argon	5.1	300	0.765	

1.138 cm² (no blockage) Surface

17% Porous Volume

$r = .12\mu$

$T = 308^\circ\text{K}$

$\Delta P = 16.0$ mm Hg.

$L = 1.35 \times$ plate thickness

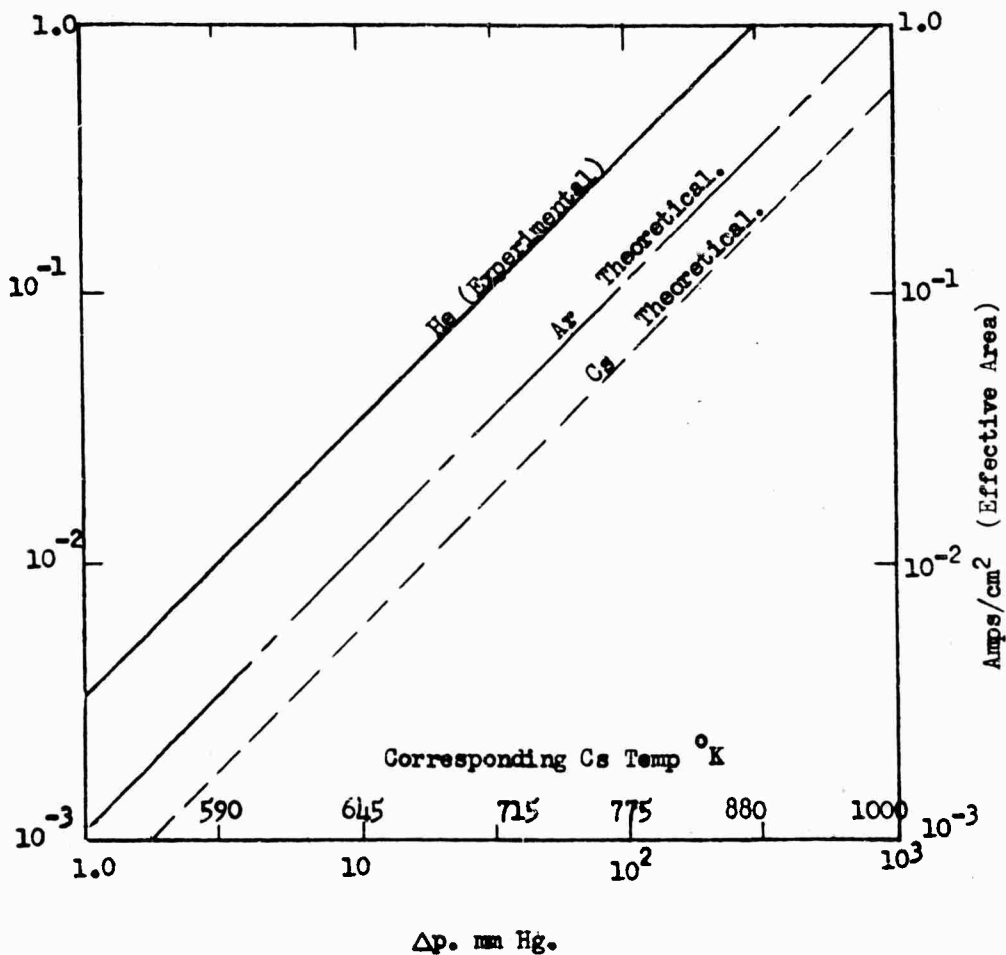


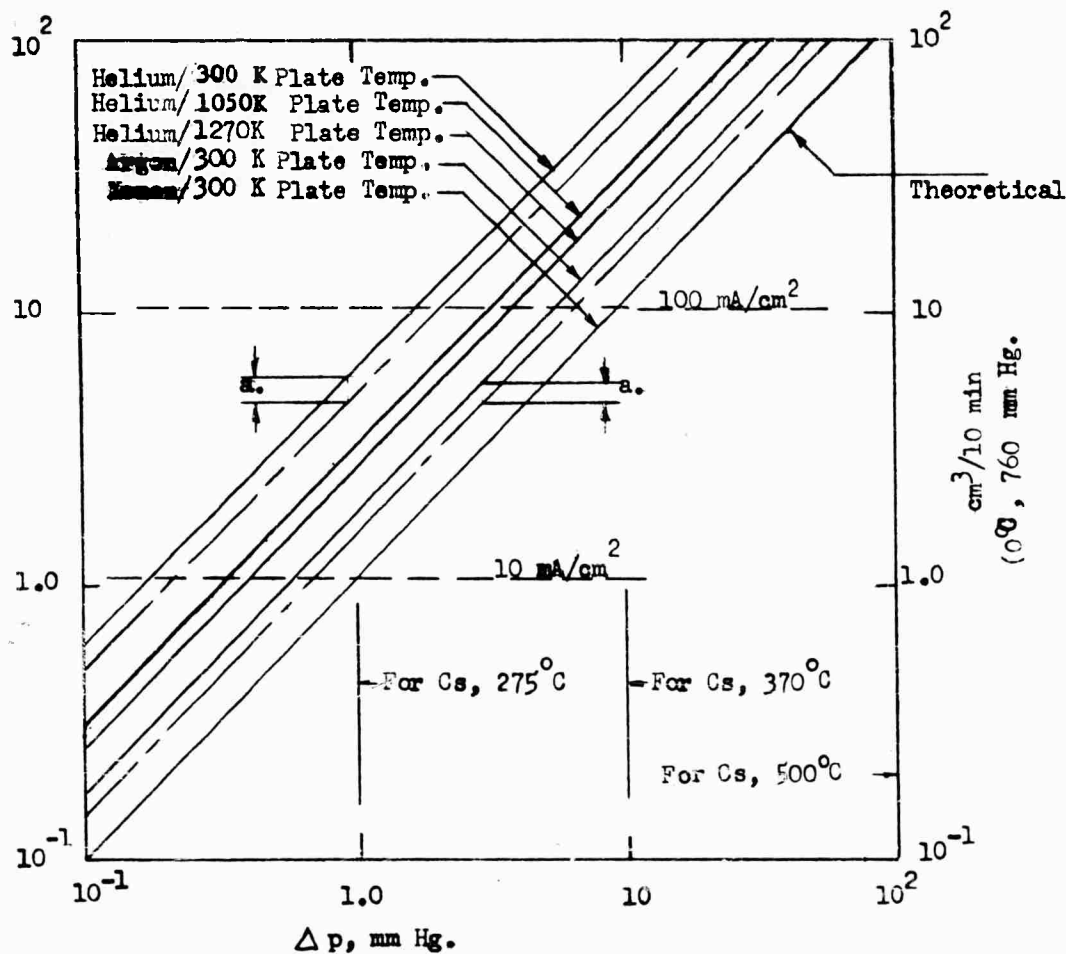
Figure IV-15.

EXPERIMENTAL AND THEORETICAL
FLOW DATA FOR P-2 TUNGSTEN PLATE

43% Porous Volume

Surface Area, 0.797 cm²

a = Aging Effect (After heating)



EXPERIMENTAL

FLOW DATA FOR F-1 POROUS TUNGSTEN

PLATE SHOWING AGING EFFECT

Figure IV-16

.798 cm² Surface
42.2 % Porous Volume

T = 293 °K
Δp = 19.4 mm Hg.
L = 1.23 x Plate Thickness
r = .509 μ

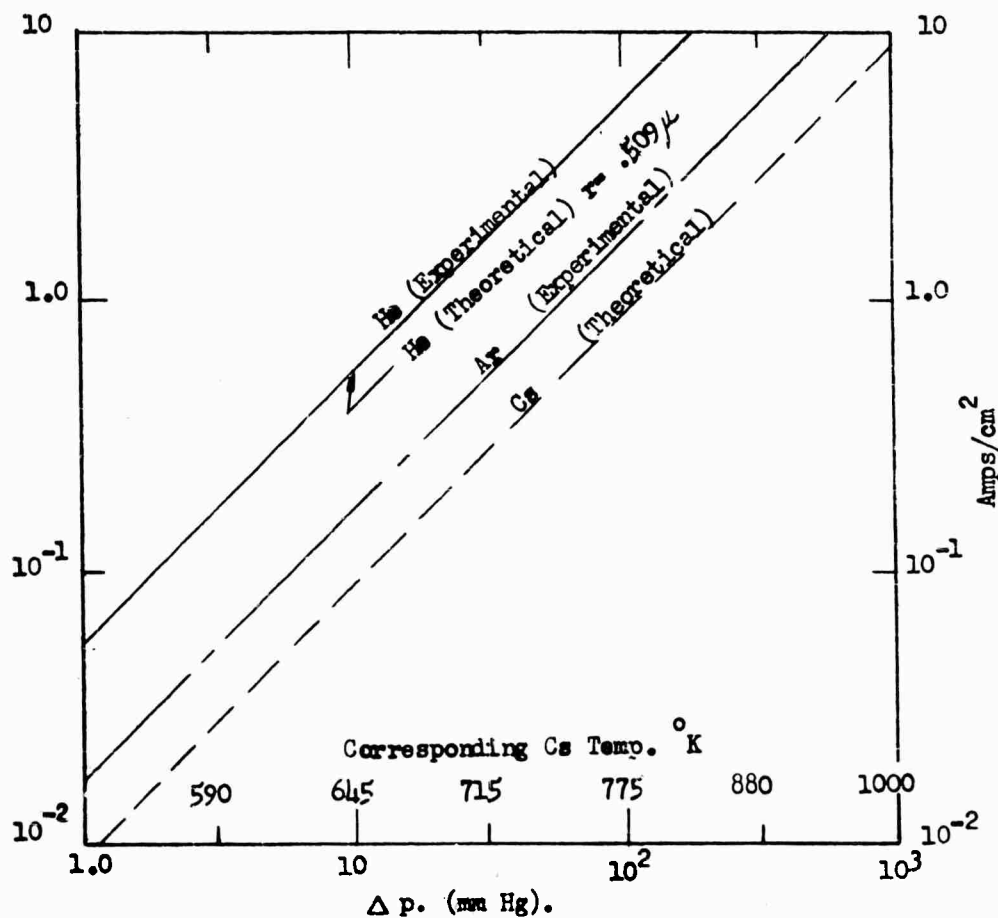
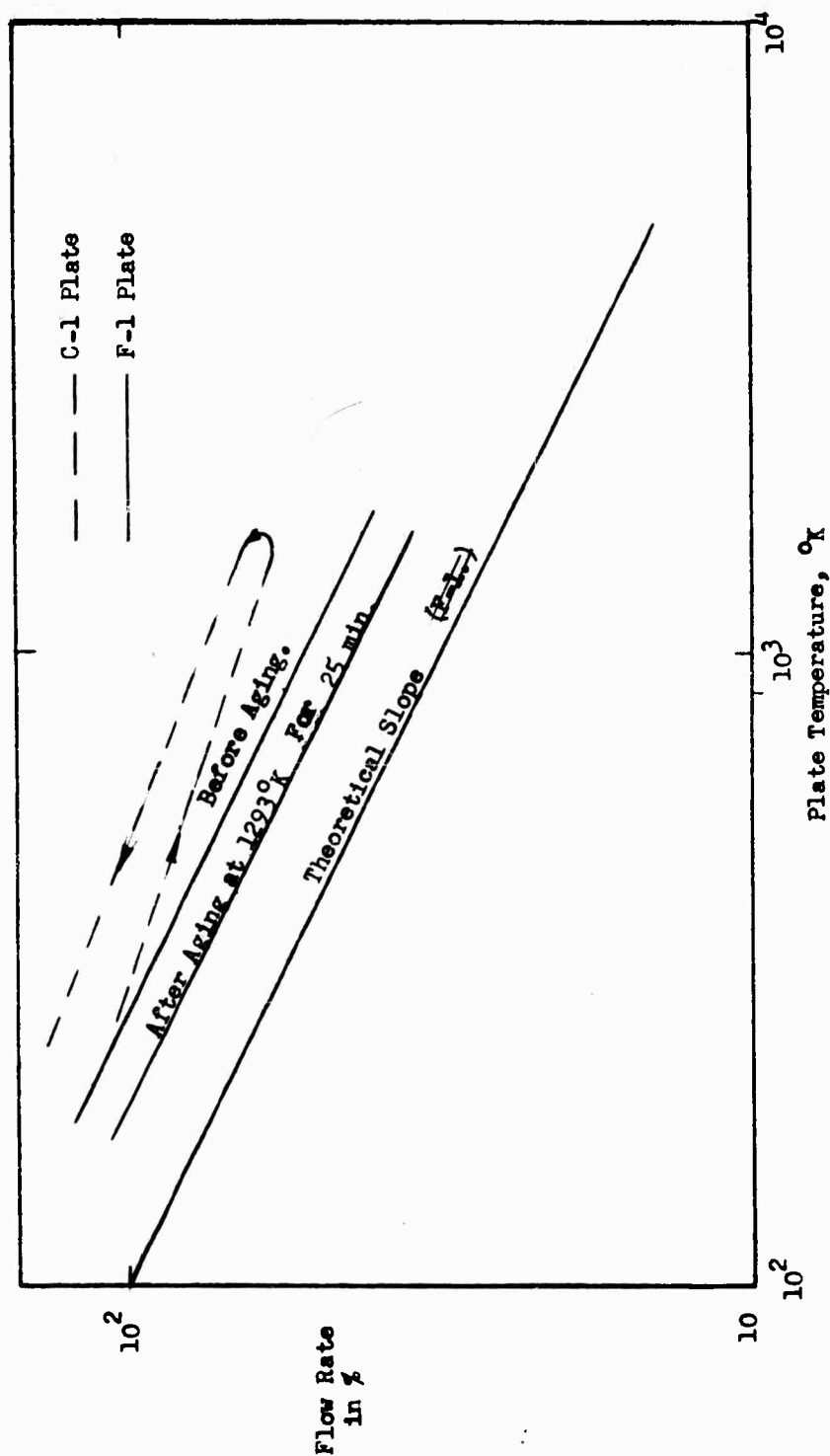


Figure IV-17.

EXPERIMENTAL AND THEORETICAL FLOW DATA
FOR F-1 POROUS PLATE

Figure IV-18.



HELIUM FLOW RATE THROUGH POROUS TUNGSTEN EMITTERS
AS A FUNCTION OF PLATE TEMPERATURE (Molecular Flow)

Figure IV-18

The flow rate through C-1 tungsten plate versus plate temperature is also shown in Figure IV-18. The slopes do not follow closely the $1/T^2$ slope. The arrows indicate the temperature cycle. With decreasing temperature the flow rate is increased, possibly due to bypassing caused by non-uniformity of the bond. Data are given in TABLE IV-I and Figure IV-19.

In connection with the development of the L-cathode, which is similar in construction to the P-series emitters discussed herein, Rutledge and Rittner (Ref. 68) measured Ba-flow rates through porous plates in the range between 11% and 29% porous volume. Figure IV-20 shows their values of transmission coefficient versus porous volume. Our test results are low in comparison with the Rutledge and Rittner data due to clogging as previously discussed in conjunction with TABLE IV-G.

Current and flow rate are related by: $(K)(e) = I$ amps, where $e = (1.602)(10^{-19})$ coulomb, k is the number of particles per second, and I is the current in amperes; assuming 100% ionization efficiency and singly-charged particles. Therefore 1 amp is equal to $(6.25)(10^{18})$ singly-charged particles, assuming 100% efficiency.

TABLE IV-1. FLOW DATA FOR C-1 POROUS TUNGSTEN PLATE

Porous Volume: 48.2%

Surface Area 1.259 cm²
Plate Thickness: 2.645mm

Gas	dp (mm Hg)	Plate Temp. °K	Vg (cm ³ /min)
He	4.4	299	2.8
He	33.0	299	22.6
He	3.0	299	2.0
He	4.1	300	2.65
He	12.8	300	8.8
He	8.0	300	4.85
He	3.7	377	1.92
He	5.7	375	3.58
He	6.4	598	3.2
He	6.4	783	2.9
He	4.6	297	3.15
He	4.5	953	1.87
He	3.8	1158	1.52
He	3.6	297	0.96
He	5.65	1280	2.335
He	2.1	299	1.685

1.259 cm² Surface
48.2% Porous Volume

$r = .415\mu$
 $T = 299^\circ\text{K}$
 $\Delta P = 4.4 \text{ mm Hg.}$
 $L = \text{Plate Thickness}$

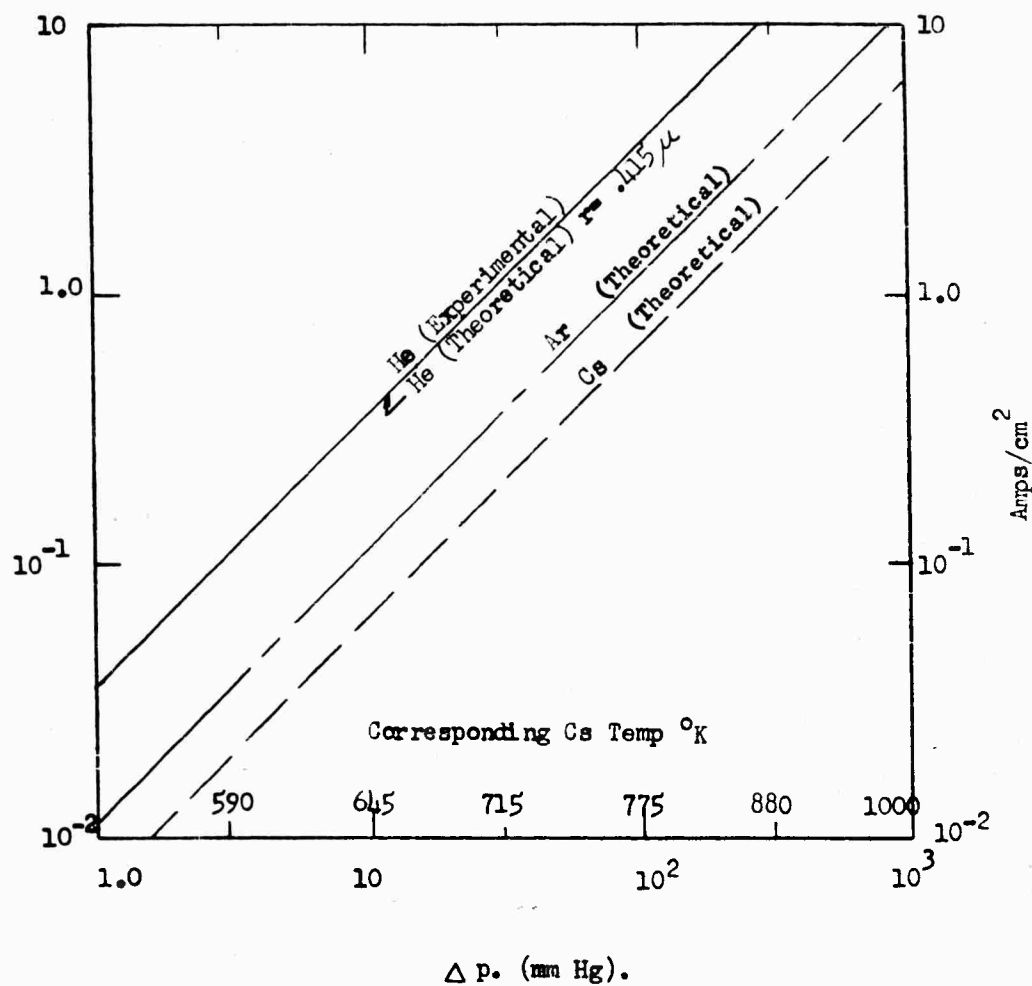


Figure IV-19.

EXPERIMENTAL AND THEORETICAL
FLOW DATA FOR C-1 POROUS PLATE

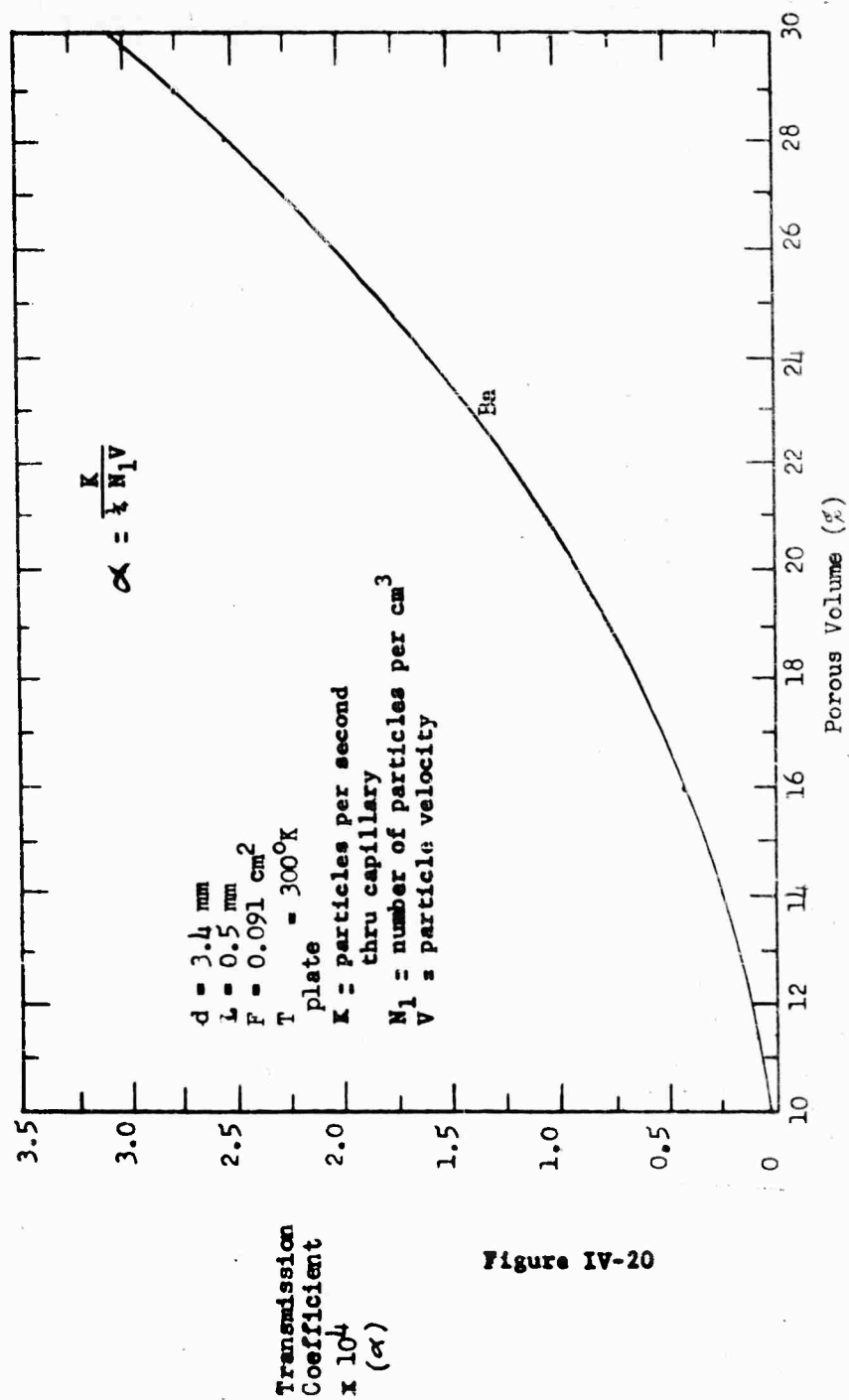


Figure IV-20

TRANSMISSION COEFFICIENT VERSUS POROUS VOLUME FOR BARIUM THROUGH POROUS PLATE

Conclusions

The results of the diffusion tests on a unit basis are given below in Table IV-J for helium gas at a plate temperature of 300°K. For higher plate temperatures, excellent agreement with the $T^{-1/2}$ power law was demonstrated.

TABLE IV-J. UNITIZED DIFFUSION FLOW RESULTS

Emitter	Hole Length,u	Hole Diameter,u	Flow Rate per Hole, cm ³ /min (at 760mm Hg, 0°C)	Flow Rate per Unit Area, cm ³ /min - cm ² - mm Hg (at 760mm Hg, 0°C)
Platinum Screen	125	25	1.93 (10 ⁻³)	0.98
Moly Screen	25	70	24 (10 ⁻³)	40.0
Porous Tungsten F-1	---	--	-----	0.59
Porous Tungsten C-1	---	--	-----	0.82
Porous Tungsten P-1	(See further remarks below on this measurement)			0.048

per mm Thickness

The measured flow rate for the platinum screen was in excellent agreement with the predicted value. The results for the molybdenum screen are not as large as had been expected. The measured flow rate for porous plate P-1 is approximately only 40% of published data. As indicated previously and as further discussed in Section VI, the cause of the latter deviation is being further investigated, and will be presented in a letter addendum to this report.

Perhaps the most significant result of this phase of the investigation (i.e., diffusion measurements) is the excellent correlation between diffusion data obtained with inert gases and the ion current actually measured for cesium fuel (See Section V). The correlation also shows that the effect of surface flow for the tested specimens and operating conditions (which are typical for an ion engine) can be considered to be minor.

For the continuation of this type of experiments, it is recommended that xenon gas be used in the range of vapor pressures corresponding to that of alkali fuels to further investigate surface flow rate effects.

It is suggested also that these investigations be extended to a larger number of porous plates, with porous (void) volumes in the range between 15% and 40%. In addition, the effects of grain size, grain form, grain size distribution, and sintering pressure and temperature should be investigated, with grain sizes in the range of 10u, 3u, 1u,

0.3u, and 0.1u. The sintering temperatures should be above 2000°K to avoid shrinkage at working temperatures. Because the consolidation effect may be small in comparison with other grain forms, spherical grains seem to be promising and should be evaluated in subsequent experiments. Very small grains (between 1u and 0.1u) appear to be of interest, because the fuel distribution over the plate surface tends to equalize at temperatures lower than for the larger grains and, in addition, surface flow may contribute to the total flow rate, per Sears and Hill (Ref. 69 and 70).

V. EXPERIMENTAL EVALUATION OF VARIOUS CONTACT EMITTERS

The results of cesium ionization experiments with various types of emitters are presented in this section. The apparatus, including an ion gun and a mass spectrometer, are described and the experimental technique is discussed.

The results indicate a close correlation between measured ion currents and predicted values based on diffusion data acquired with inert gases. It is shown that a porous sintered emitter can provide reliable and predictable results. A molybdenum screen containing holes approximately 0.003 inches (68u) in diameter provides a lower ionization efficiency due to the large hole size. Continued testing of various emitters is recommended; the emitters to be used in further tests are described herein.

The experiments and the preparation of this section of the report were supervised by Dr. O. K. Husmann, with Mr. B. Houck assisting in the laboratory.

V. EXPERIMENTAL EVALUATION OF VARIOUS CONTACT EMITTERS

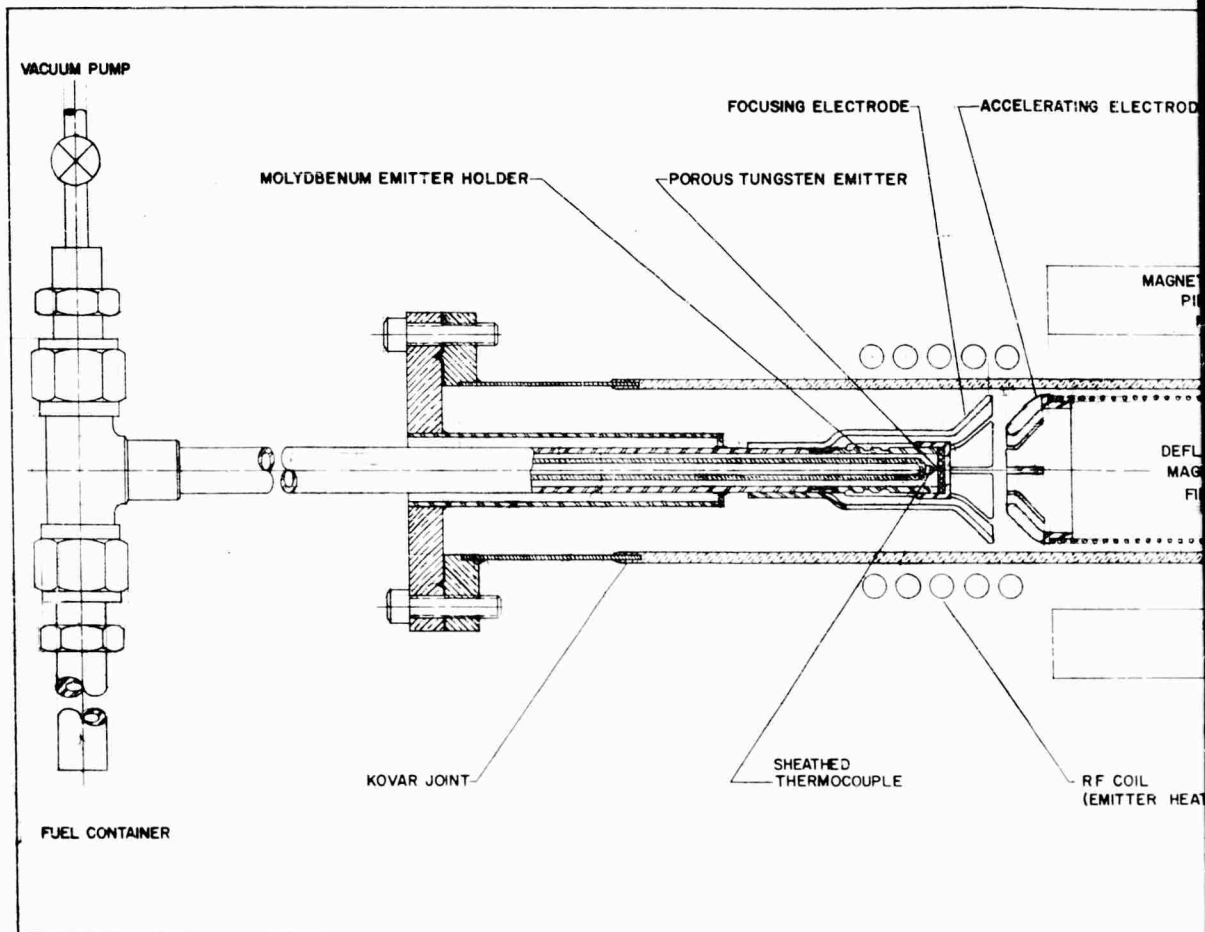
The experimental investigation of an ion source requires measurement of the ion current and of the ionization efficiency, as a function of such operating conditions or parameters as emitter material, surface temperature, surface contamination, emitter porous volume and pore size, and cesium vapor pressure or temperature. The initial measurements described herein were made in an ion gun using a Pierce system for ion current extraction. In order to prevent secondary emission, a deep Faraday cage is used as the target, in front of which a suppressor grid has been mounted. Because it is difficult to prevent the ionization of the residual gas in the system, and in particular the emission of secondary electrons, the ion gun system is not expected to provide precise readings. It is particularly difficult, even with the application of a magnetic field perpendicular to the beam, to distinguish between ions of different masses. To overcome the aforesaid handicaps, a mass separator had been constructed and will be used in later tests to provide more complete data.

A. Ion Gun

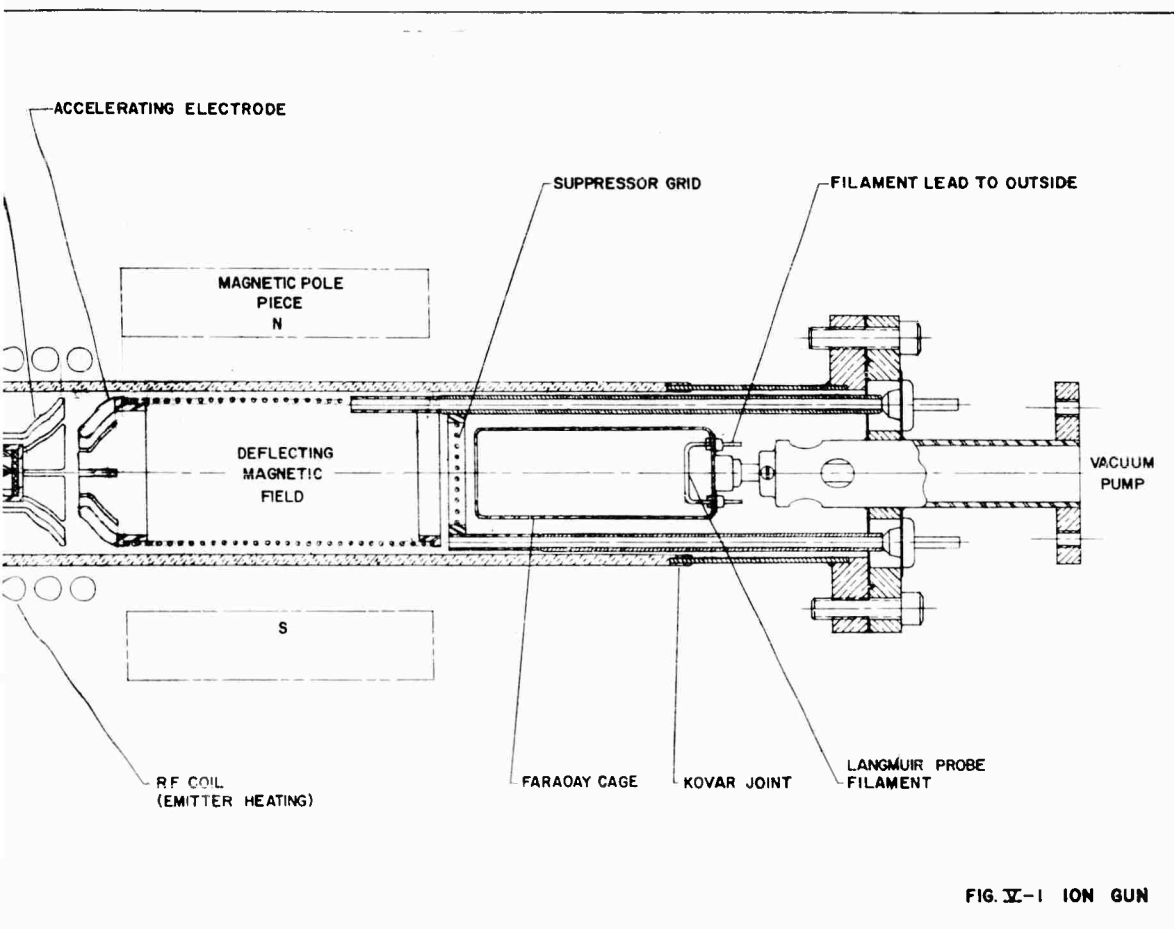
Figure V-1 is a schematic of the ion gun apparatus. The fuel container is connected to the porous emitter plate by a $\frac{1}{4}$ -inch tube. The cesium capsule is placed in the fuel container (a nickel tube) and externally broken after thorough evacuation and outgassing. During the experiments, the fuel container is heated by hot air which can be regulated to maintain the fuel temperature constant within 3°K in the range from 300°K to 600°K . The fuel vapor pressure corresponds to the lowest temperature in the fuel system. The vapor which penetrates through the plate is partially ionized on the surface and accelerated by the Pierce electrode system toward the Faraday cage.

The emitter is heated by RF; typical data are given in Figure V-2. The matching between the RF coil and the emitter plate shown in Figure V-1 has an estimated power efficiency of 10%. By design and with a proper coil configuration, the matching can be improved, but is not required at present for the ion gun experiments since the desired emitter temperature can easily be attained. As shown in Figure V-2, the position of the coil can be altered within a limited range to improve the matching. An obvious question in the use of RF heating is the effect of the RF field on the ionization process itself. It was experimentally established in the present experiments that the RF field used for emitter heating did not affect ionization.

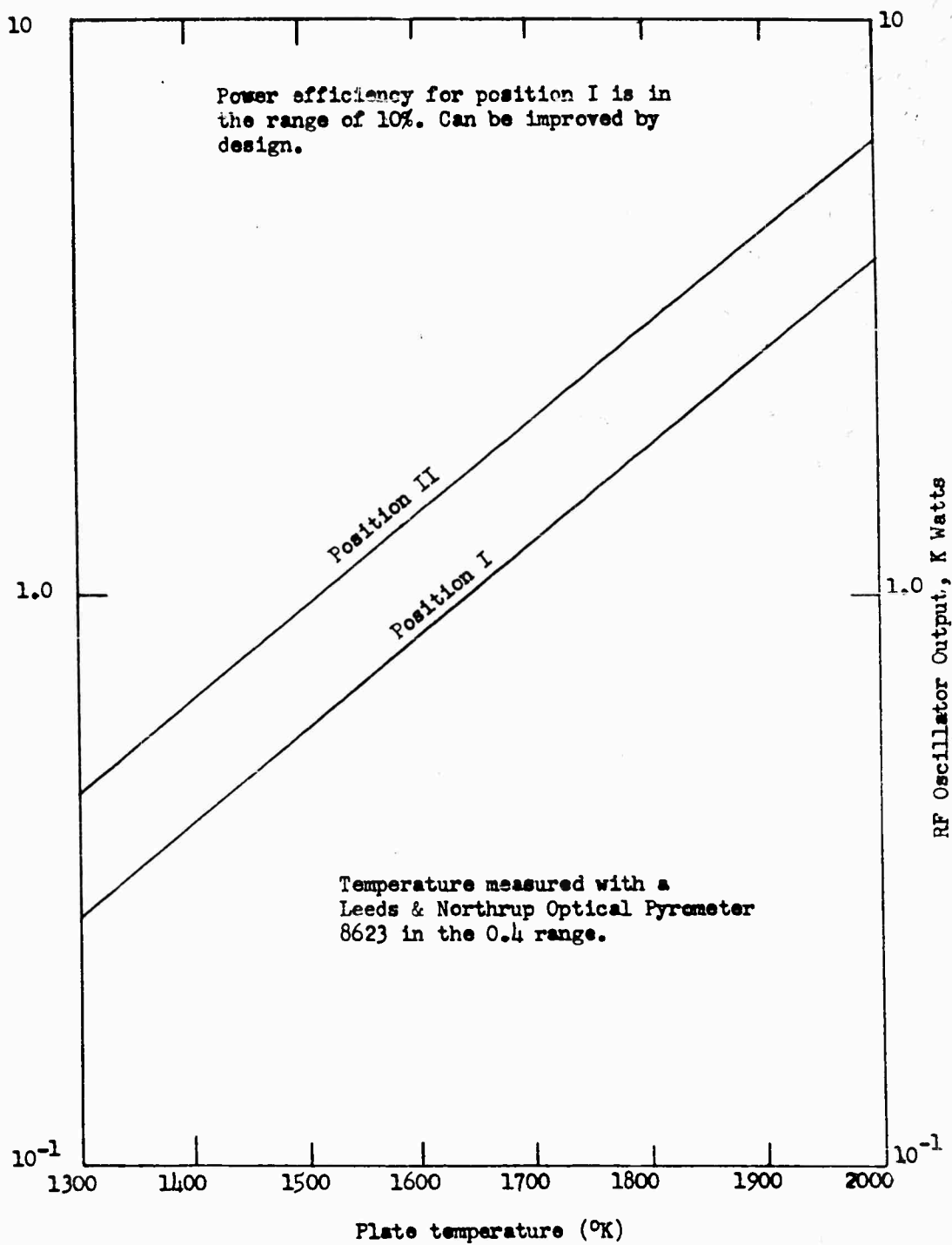
The focusing and acceleration electrodes in the apparatus of Figure V-1 were originally slotted to reduce electrode heating by the RF system. For still better matching of the emitter the electrodes subsequently were shaped of tungsten wires, with excellent results. It should be



1



2



RF HEATING OF THE P-I POROUS TUNGSTEN EMITTER

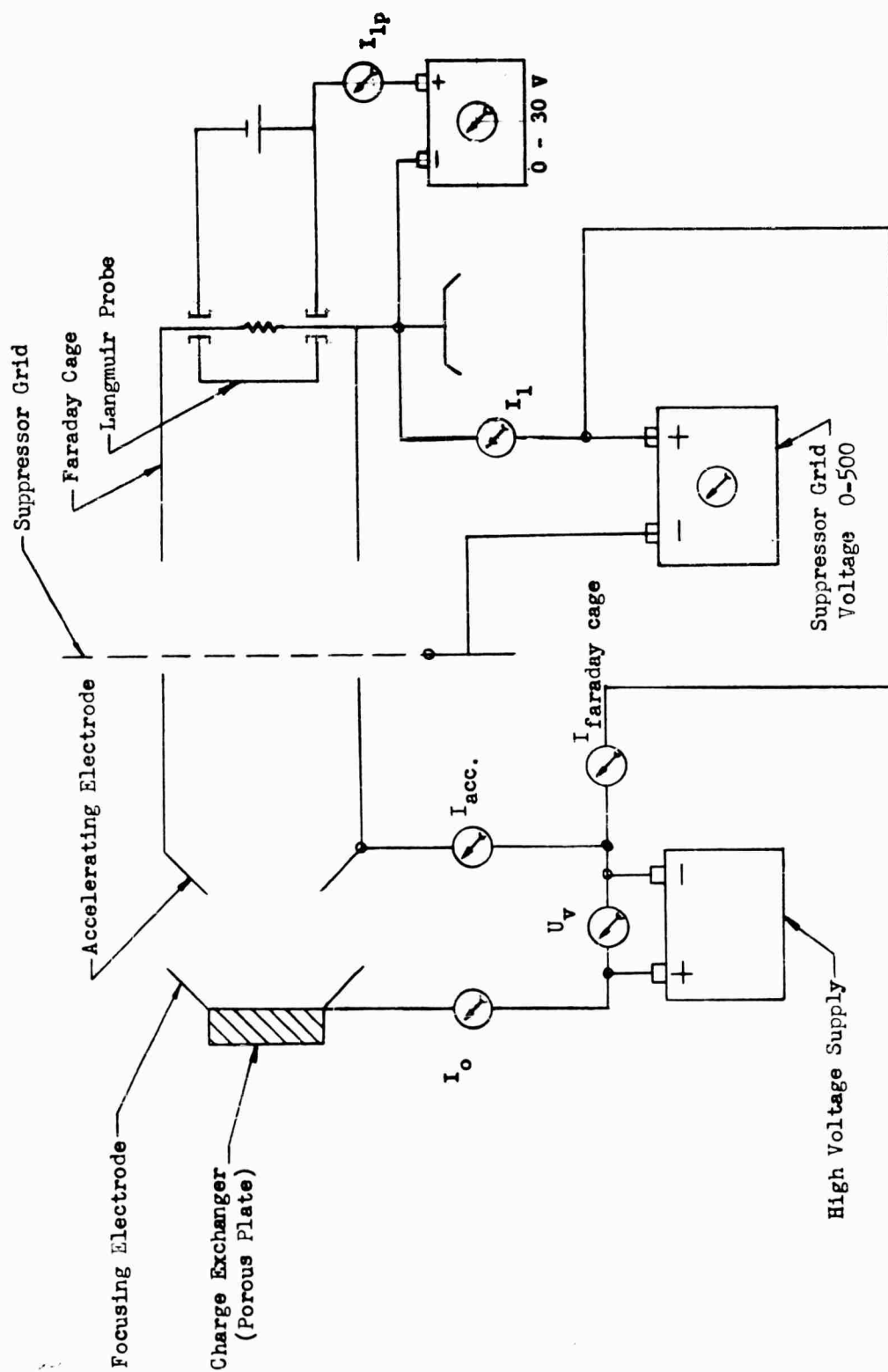
FIGURE V-2

noted that current flow in the mA range from the accelerating electrode to the emitter (electron emission) will contribute to heating the emitter, particularly at higher accelerating potentials. The change in the emitter plate temperature due to this effect was observed by pyrometer while the RF power and the RF coil configuration relative to the surface ionizer were held constant. It is possible that the emitter could be designed to be heated in this way after initial heating by a conventional method. (Experiments on the stability of this heating method have not been conducted.)

Inasmuch as sputtering cannot be prevented, it is necessary for reasons of power efficiency to maintain either a relatively hot or a relatively cool acceleration electrode to prevent excessive electron emission (Ref. 77). The work function of W-Cs is only 1.36 volts. If it were possible to reduce sputtering of the acceleration electrode appreciably (for instance, by proper design of electrode configuration) the question of temperature of this electrode in relation to electron emission would be of minor interest because of the high work function of tungsten. In the case of sputtering, however, part of the impinging Cs will build up a Cs layer with a resultant decreased work function. At higher electrode temperatures part of the Cs layer is evaporated and at sufficiently high temperature only part of a Cs monolayer covers the electrode with a consequent small reduction in the tungsten work function. It may be emphasized that even at 600°C a Cs-covered tungsten electrode can emit high electron currents. The number of impinging ions cannot be made zero and, in addition, a small fraction of neutrals may impinge. Because of the distance between the emitter and accelerating electrode, the latter will be heated by radiation and maintain a very low fuel coverage in a well-designed acceleration system.

The entire ion gun apparatus is mounted in a two-inch Pyrex tube which permits easy outgassing; only glass or metal is used, including the vacuum gasketing. The magnetic pole pieces shown in Figure V-1 are provided to deflect the ion beam so that neutrals can be measured with the Langmuir probe in the Faraday cage (which is cooled by liquid nitrogen). With a four-inch gap between the accelerating electrode and the suppressor grid, a 1200 gauss magnetic field deflects a 200 volt-accelerated cesium ion beam. A later model of the gun with a 15-inch gap permitted accelerating potentials up to 10 kv with a larger number of magnets.

Figure V-3 shows a wiring diagram for the ion gun. The current at the acceleration electrode and Faraday cage are measured separately; instrument ranges are from one μ A to 300 μ A in five steps. The main instruments are on the ground (negative) side of the circuit and only I_0 and the fuel temperature are measured on the high voltage side. Because of the low voltage drop in the instruments, the accelerating potential is measured directly at the high voltage source (maximum 20 kv and 50 mA). A second potential, adjustable between 0 to 500 volts



WIRING DIAGRAM FOR ION GUN

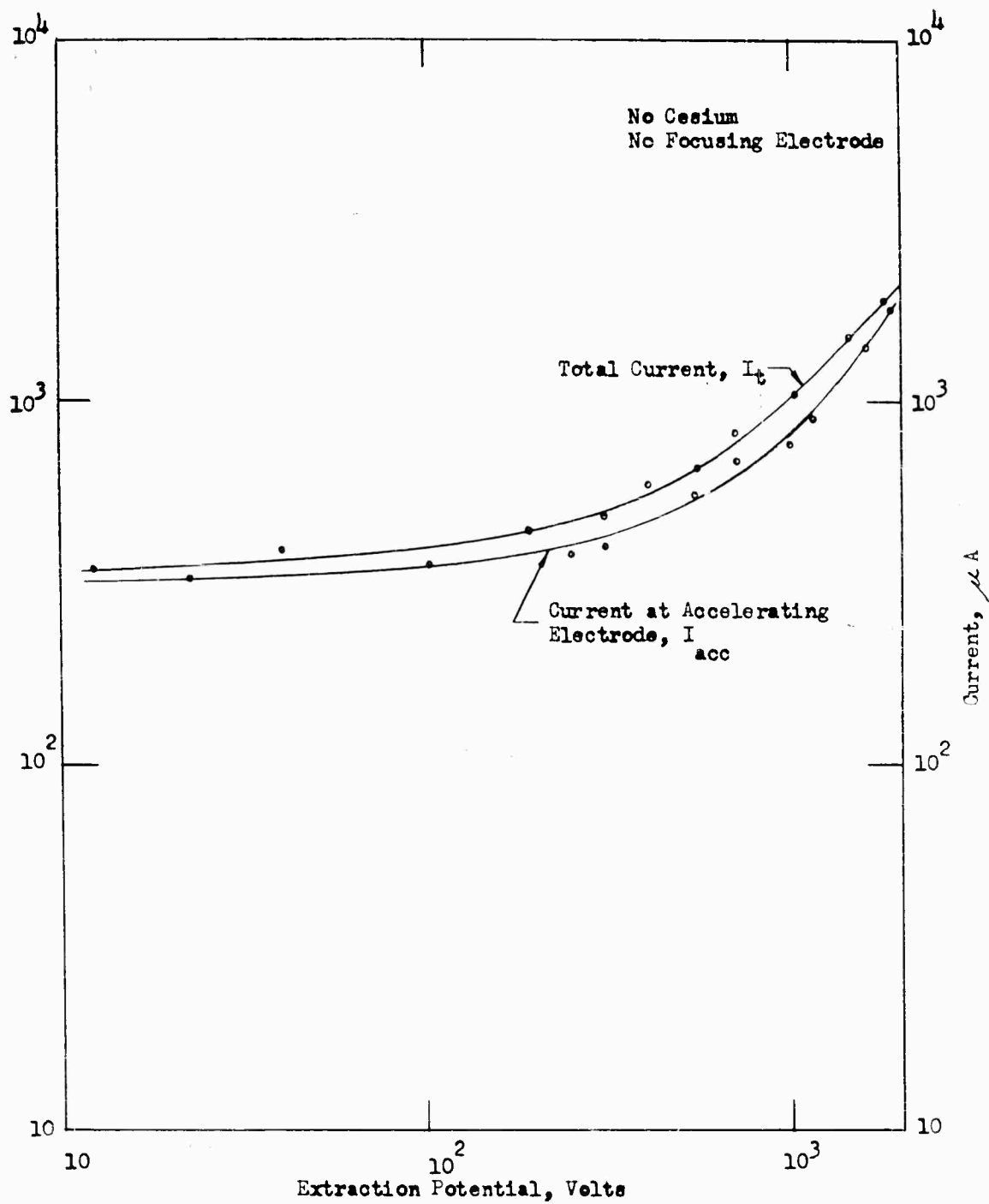
FIGURE V-3

negative on the grid side, is included. The filament of the Langmuir probe is separately heated and a voltage supply permits measurement of the neutral ratio.

SE emitted from the suppressor grid can contribute to the Faraday cage current. Even when the cage current is measured at I_1 (see Figure V-3), SE from the suppressor grid can cause increased readings. By means of the instruments at I_0 , I_1 , I_{acc} , and I_{F-cage} , distinction can be made between ion current and SE. In confirmation, extrapolation of the Faraday cage currents from readings at low potential gives the same results (see Ref. 30 and 31). The contribution from the residual gases in the ion gun system is analyzed by the method of Von Ardenne (Ref. 47, p. 573).

Before starting each experiment, the complete gun system was carefully outgassed, including heating of the emitter (heated to 1750°K for approximately ten minutes in the case of the platinum-bonded plates, and to 1900°K in the case of the mechanically-bonded plates), acceleration electrode, and F-cage. In particular, the porcelain insulators were outgassed. It can be noted that the metallic vacuum seals were repeatedly heated for several hours to 620°K without failure. Experiments were conducted with emitter plate temperatures up to 1800°K. Operating vacua between $(5)10^{-6}$ and $(5)10^{-7}$ mm Hg. were obtained. During the experiments it was noted that the pressure (measured with an ionization gage between the ion gun and diffusion pump) increased somewhat with the acceleration potential. This effect can be attributed to gas adsorbed on the walls, and is reduced with time. Proper outgassing of the gun components, especially on the F-cage side, improved the vacuum considerably during the operation of the gun.

Figure V-4 shows the total current (F-cage current plus the accelerating electrode current) and the accelerating electrode current alone versus the extraction potential for the first experimental extraction system (without a focusing electrode). The current was not constant and decreased considerably with operating time of the gun. This current is a spurious reading and could be misconstrued as a legitimate reading in an ion gun device. After the emitter had been in operation for several hours, the current due to residual unidentified materials (measured with the fuel temperature at 300°K) had been reduced to a small value in the one microamp range. For this condition, the accelerating electrode current approached a relatively constant value at higher accelerating potentials.



ION GUN CURRENT WITH RESIDUAL GASES

FIGURE V-4

B. Emitter Evaluation

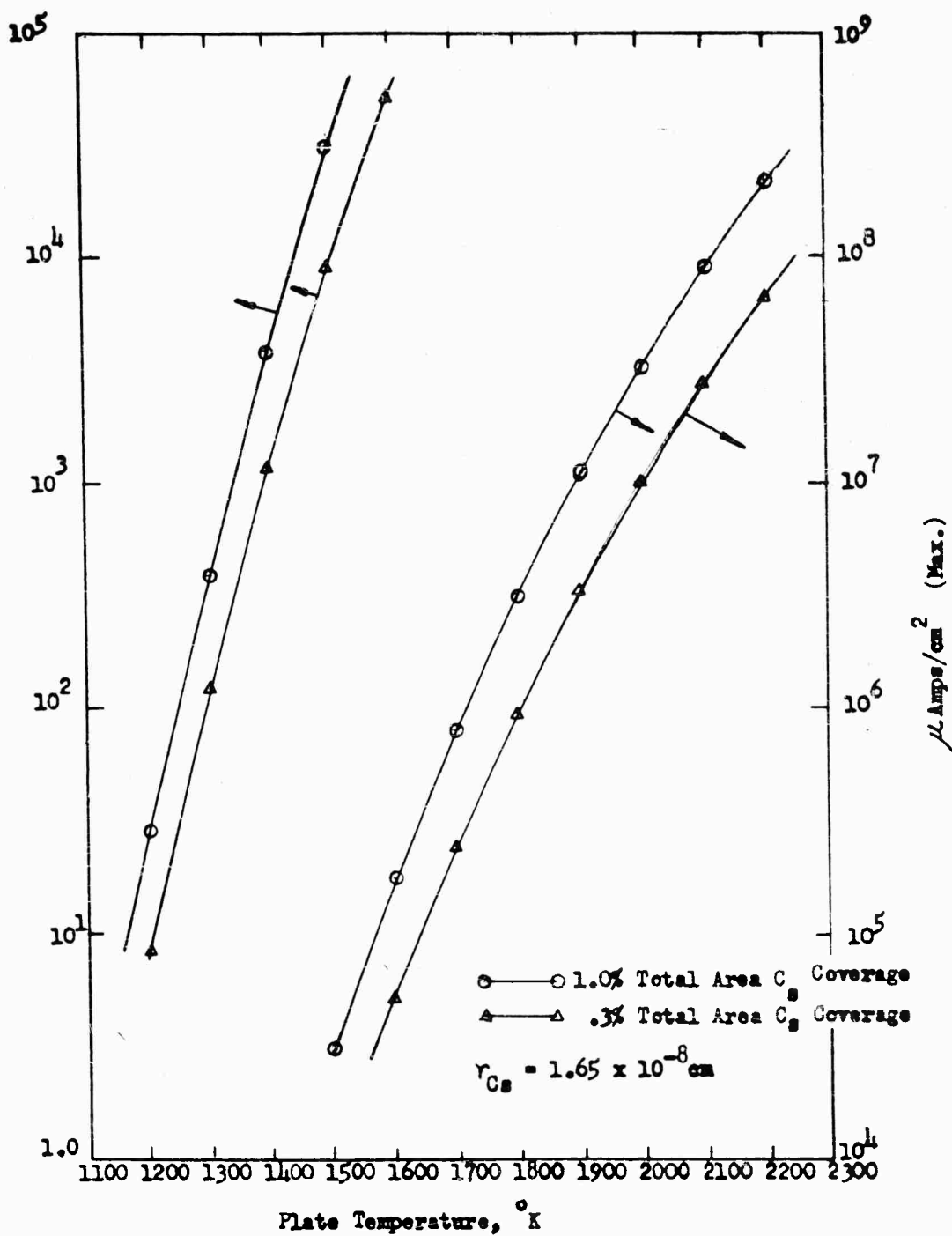
Before presenting the emitter test results, it is significant to review the theoretical limits. At a plate temperature of 1500°K a cesium ion current of 10^4 u amps/cm^2 is possible, using the values for lifetimes given by F. Knauer (Ref. 19), with 0.3% surface coverage as shown in Figure V-5. For platinum and tungsten plates using a cesium fuel, the ionization efficiency is 95-100% in the range between 1200°K and 2000°K (see Figure II-1). Thus, under the assumption of equal distribution of the fuel over the W_0 surface (i.e., at a sufficiently high migration velocity), only the diffusion flow rate and the fuel lifetime affect the ion current. To avoid reduction of the work function, a maximum 0.3% coverage is preferable, and this maximum coverage in connection with the diffusion flow rate gives the minimum required plate temperature (the upper limit of plate temperature is influenced by radiation losses, bonding problems, and aging effects).

The results given below apply to the molybdenum screen, and to the F-1 and F-1 porous tungsten emitters. The moly screen and the F-1 emitter were Pt-brazed to the fuel vapor supply tube; the F-1 emitter was investigated with both the mechanical bonding and the Pt-braze. In each case, the emitter was affixed to a molybdenum tube 2" long; the latter tube in turn was Pt-brazed to a tantalum tube attached to the fuel system. Before the emitter tests, the brazed emitters were tested to ascertain that there was no by-pass flow.

Molybdenum Screen Emitter

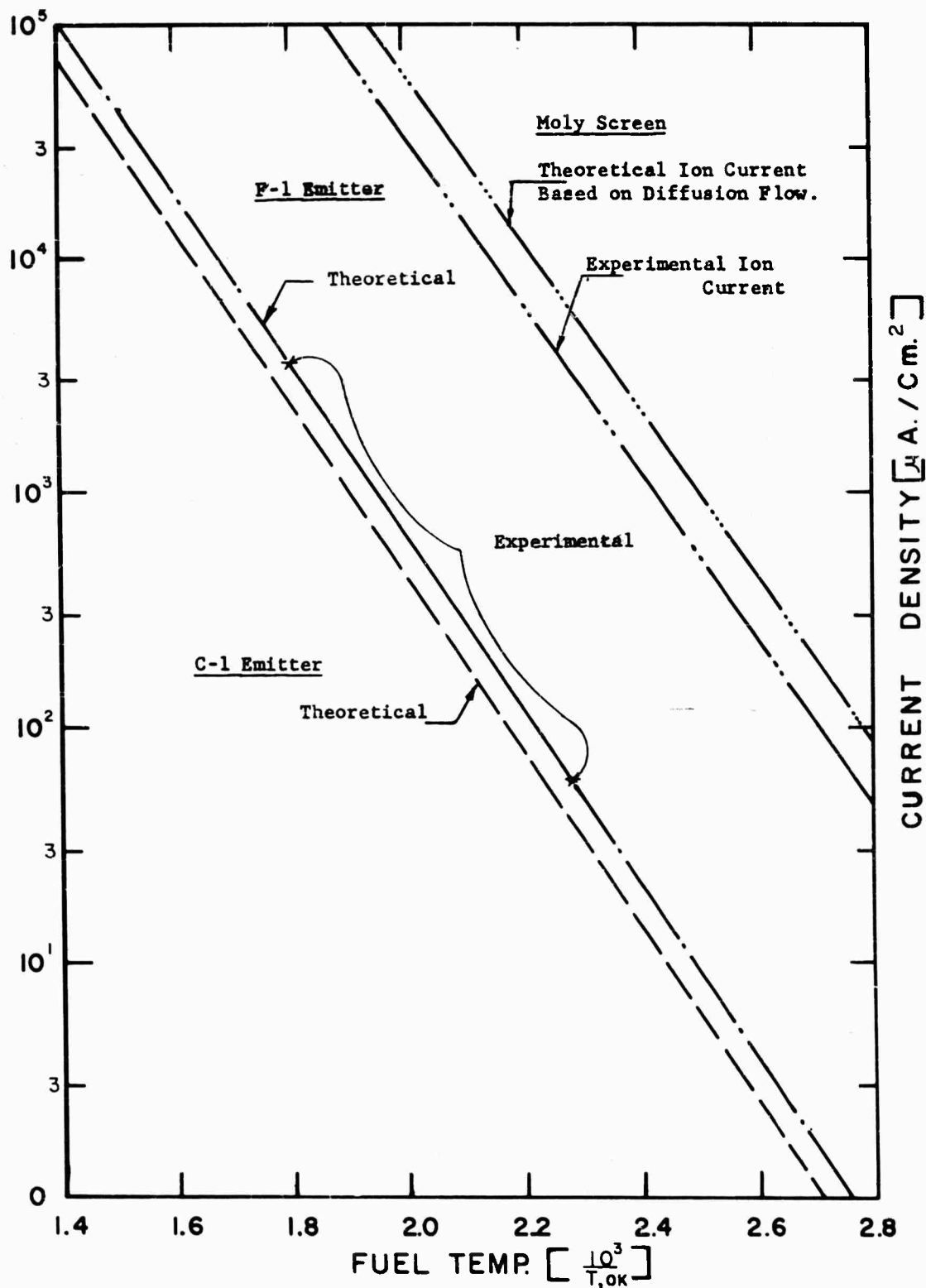
The details of construction were as follows: Pt-brazed in moly tubing; surface area 0.38 cm^2 ; ca 640 holes; 68 u hole diameter; 25 u hole length. Before testing with cesium, the screen was out-gassed for approximately two hours. During the experiments of approximately seven hours' duration, the exchange surface temperature was maintained between 1400° and 1700°K ; the fuel temperatures did not exceed 417°K . Electrode distance was 6.30 mm and the accelerating potential was varied up to 16 kv. The results indicate that below 150 volts the Faraday cage current followed the $U^{3/2}$ law closely at lower fuel temperatures. At higher accelerating potentials SE emission resulted in deviation from the expected values toward higher currents, as discussed previously. Separate measurement of the SE contribution showed that the Faraday cage current closely followed the Langmuir-Childs law in its entire range. SE of the Faraday cage was suppressed by the negative-biased grid.

As shown in Figure V-7, the measured space-charge-limited ion current was less than that theoretically expected for a Pierce gun. For the molybdenum electron work function of 4.24 volt ionization efficiencies between 90% and 84% are derived from the Saha equation. Ion current measurements at several fuel

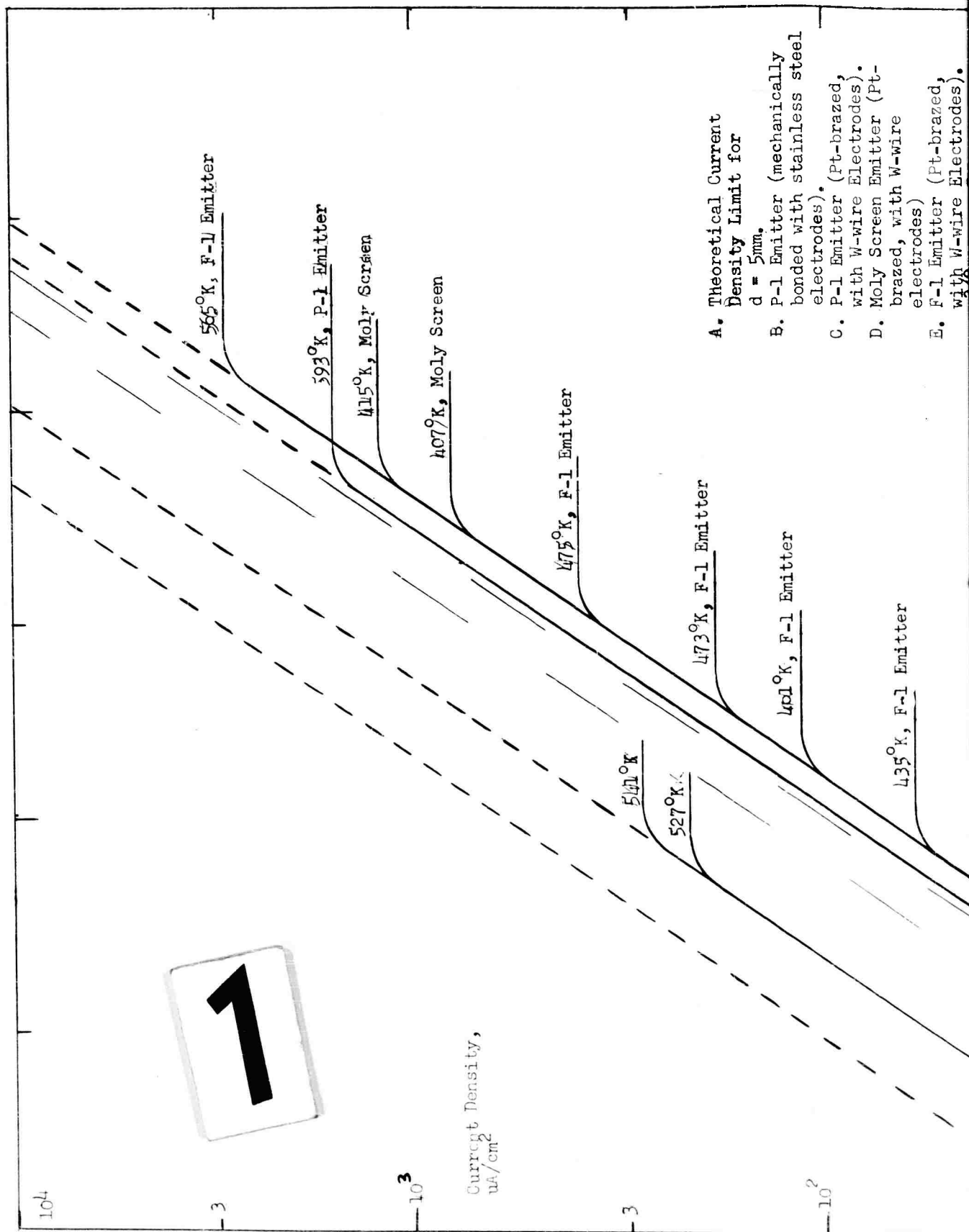


THEORETICAL DEPENDENCE OF ION CURRENT
ON PLATE TEMPERATURE (Ref.19)

FIGURE V-5



Comparison of Measured Ion Currents with Diffusion Flow Rates
for an Emitter Temperature of 1500°K .



- $d = 5\text{mm.}$
- B. P-1 Emitter (mechanically bonded with stainless steel electrodes).
 - C. P-1 Emitter (Pt-brazed, with W-wire Electrodes).
 - D. Moly Screen Emitter (Pt-brazed, with W-wire electrodes)
 - E. F-1 Emitter (Pt-brazed, with W-wire Electrodes).
 - G. U $^{3/2}$ Slope with Potassium (based on D).
 - H. U $^{3/2}$ Slope with Rubidium (based on D).

Electrode Spacing $d = 5\text{mm}$
 Emitter Surface 1 cm^2
 Cesium Fuel
 Emitter Temperature 1500°K

$1401^\circ\text{K, F-1 Emitter}$

$1435^\circ\text{K, F-1 Emitter}$

Figure V-7 Measured Ion Current
 Densities for Various
 Emitters

Acceleration Potential, Volts

10^3

3

10^4

3

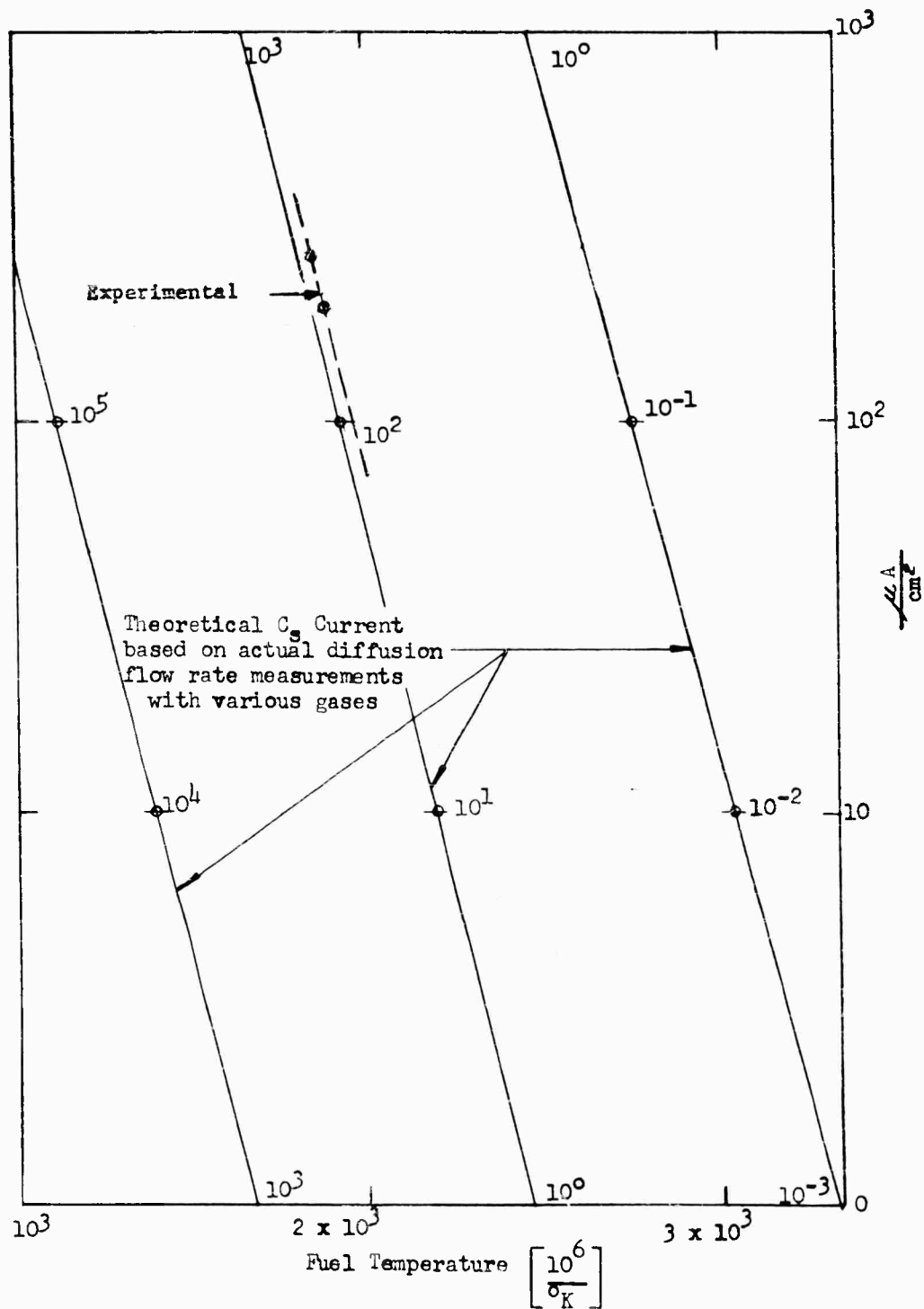
temperatures confirmed the theoretical slope of the saturation ion current but yielded an ionization efficiency of only 55% of the value predicted from the diffusion flow rate measurements (Fig. V-6). The explanation for this low ionization efficiency may be due partially to fuel passing directly through the relatively large holes, and partially to a dense fuel layer around the holes, thereby reducing there the work function. (The migration velocity of Cs on moly is not known.) For purposes (Fig. V-7) of comparison, the calculated $U^{3/2}$ slope for Rb and K also are shown. In the experiment with cesium on the moly screen emitter at 415°K the saturation ion current reached a current density of 1.43 mA/cm². It is intended to expand these experiments to higher vapor pressures using smaller holes in order to increase the ionization efficiency.

Emitter P-1 Test Results

Figure V-7 includes the test results for the P-1 mechanically-bonded emitter. Maximum ion current was about 280 uA, close to the expected value based on diffusion measurements. A microscopic investigation of this emitter after the Cs ionization experiments showed a surface coverage (estimated to be 90% of the effective area) with a non-porous metal layer, possibly Ni. The measured flow rates therefore may be due primarily to bypassed fuel. In Figure V-8, the diffusion flow rate (theoretical current) measured as described in Section IV with a plate temperature of 1200°K, is plotted in microamps per square centimeter versus the inverse fuel temperature and is compared to the experimental results. The dotted curve shows the measured saturation ion current. The saturation current follows the slope of the fuel diffusion flow rate closely. The plate temperature has only a small influence on the diffusion because the reduction in the diffusion rate with $1/T^{1/2}$ is overcompensated by the steep increase of the flow rate with the vapor pressure.

In addition, a Pt-brazed P-1 emitter was tested. This emitter showed an ion current of 600 uA when the fuel temperature was well below the corresponding vapor pressure, and even below the Cs melting point, indicating that cesium was not contributing appreciably to the current readings. After approximately three hours of operation, the Faraday cage current slowly decreased and, after six hours of operation, was less than 10 uA saturation current. Comparison of the above measured values with data published by W. C. Rutledge and E. S. Rittner (Ref. 68) showed that only 39% of the expected current was achieved when the measured current was a maximum. The reduction in the flow rate cannot be attributed to lack of fuel. Contribution of other alkali materials to the measured flow rate could not be analyzed because the mass spectrometer was not ready for use. A diffusion test with helium after the experimentation with cesium showed that the plate was clogged. An attempt to clean up by heating

Emitter P-1, Mechanically - bonded
 1.138 cm² area,
 surface temperature 1600°K



DEPENDENCE OF ION
 CURRENT ON FUEL VAPOR PRESSURE (TEMPERATURE)

FIGURE V-8

to 1500°K did not alter this affect. Microscopic inspection indicated that the Pt-braze apparently did not clog the pores, as discussed later in Section VI. Further testing of the P-1 emitter was postponed pending study of the emitter material.

Emitter F-1 Test Results

The mechanically-bonded P-1 emitter previously cited was in operation for approximately fifty hours, the Pt-brazed P-1 emitter and the moly screen emitter for about ten hours each, and the F-1 emitter described herein for approximately thirty hours. For the F-1 emitter (0.4 cm² area) at cesium fuel temperatures less than 500°K, the slope of the space-charge-limited current closely followed the $U^{3/2}$ law up to 200 volts acceleration potential; above this potential, SE increased the readings. The F-cage saturation current increased in accordance with the predicted value based upon diffusion measurements (see Figure V-6). A range between 50uA/cm² and 3 mA/cm² showed excellent correlation between the predicted and the measured current values. A maximum ion current density of 3 mA/cm² was measured at an emitter temperature slightly above 1500°K.

After 25 hours of operation as described above, the emitter temperature was increased to 1800°K. An increasing ion current was observed at constant fuel temperature. The increase in the readings were not constant and exceeded the computed flow rate measured over a range of fuel temperatures. It was presumed that the plate had failed and the test was concluded. Microscopic examination confirmed that the emitter was cracked, as discussed further in Section VI.

Conclusions From Emitter Tests

The measurements discussed in this report should be considered as the initial stage of investigation of various emitters.

- 1) The moly screen may have been covered with the Pt, which had been used as a braze, resulting in a higher work function than that of molybdenum. For comparison, therefore, measurements with a pure Pt screen with holes of the same dimension and distribution should be conducted. As a next step, screens with various smaller hole sizes will be investigated if ionization efficiencies below 95% are of interest. Based upon the investigations described herein, ionization efficiencies close to 100% do not appear attainable with a moly screen, but the screen may be preferable from a mechanical viewpoint.
- 2) In the case of the P-1 emitter bonded with platinum, it is not certain that the measured current was due entirely to cesium. Potassium or rubidium in combination with the electron work function of tungsten would result in over 60% ionization efficiency; the measured ion current for several hours' operation corresponded to only a few milligram of fuel. In the case of the mechanically-bonded P-1 emitter, it appears, from the current readings, that the fuel bypassed the porous plate, but the current follows that for Rb in the space charge range approximately.
- 3) The P-1 plate showed excellent results from the ionization viewpoint and followed exactly the predicted value based on diffusion data. Operation was satisfactory for 25 hours at operating temperatures below the emitter sintering temperature; at higher temperatures the emitter failed structurally. It is intended to continue investigation of this type of emitter, using spherical powders and a higher sintering temperature.

C. Mass Spectrometer

A magnetic mass-separator offers several advantages for the investigation of ion beams. The effect of ions coming from oil, grease, residual gases and from traces of other alkali metals can be eliminated by deflection in a magnetic field. Secondary electrons are trapped in the deflecting field and as a result the ion current measurement is not affected. In the previously described ion gun the magnetic field is used only when neutrals are to be detected, whereas in the mass spectrometer continuous measurements can be made.

Figure V-9 is a sketch of the mass spectrometer. Briefly, the ion source is located at the lower left extremity of the beam tube. The beam tube is split within the magnet, the neutrals flowing in a straight line to the Langmuir probe at the upper right of the sketch. The ion beam is deflected by the magnetic field and is measured in a Faraday cage at the right. Figure V-10 is a photograph of the spectrometer during assembly. The tube is internally gold-plated to provide an equal potential distribution. A hot oil system is used to heat the beam tube to prevent cesium vapor condensation.

With the known ion mass, a direct determination of the pulse ($H \cdot \rho$) is obtained, and thus an independent method for thrust measurement, where H is the magnetic field strength in gauss and ρ is the radius of curvature in the field. Investigation of the ionization efficiency at various operation conditions is possible with this equipment, in particular because the partial neutral ratio can be measured continuously independent of ion current, and the total neutral ratio can be computed.

The unit will be operated with small-area emitters. The emitter design resembles that of the ion gun with regard to the arrangement of the fuel system, the porous plate set-up, and Pierce electrodes.

In connection with the high mass of the ions and acceleration voltage up to 20 kv a field strength up to 9k gauss in the gap is required. A 60° type spectrometer was designed, where

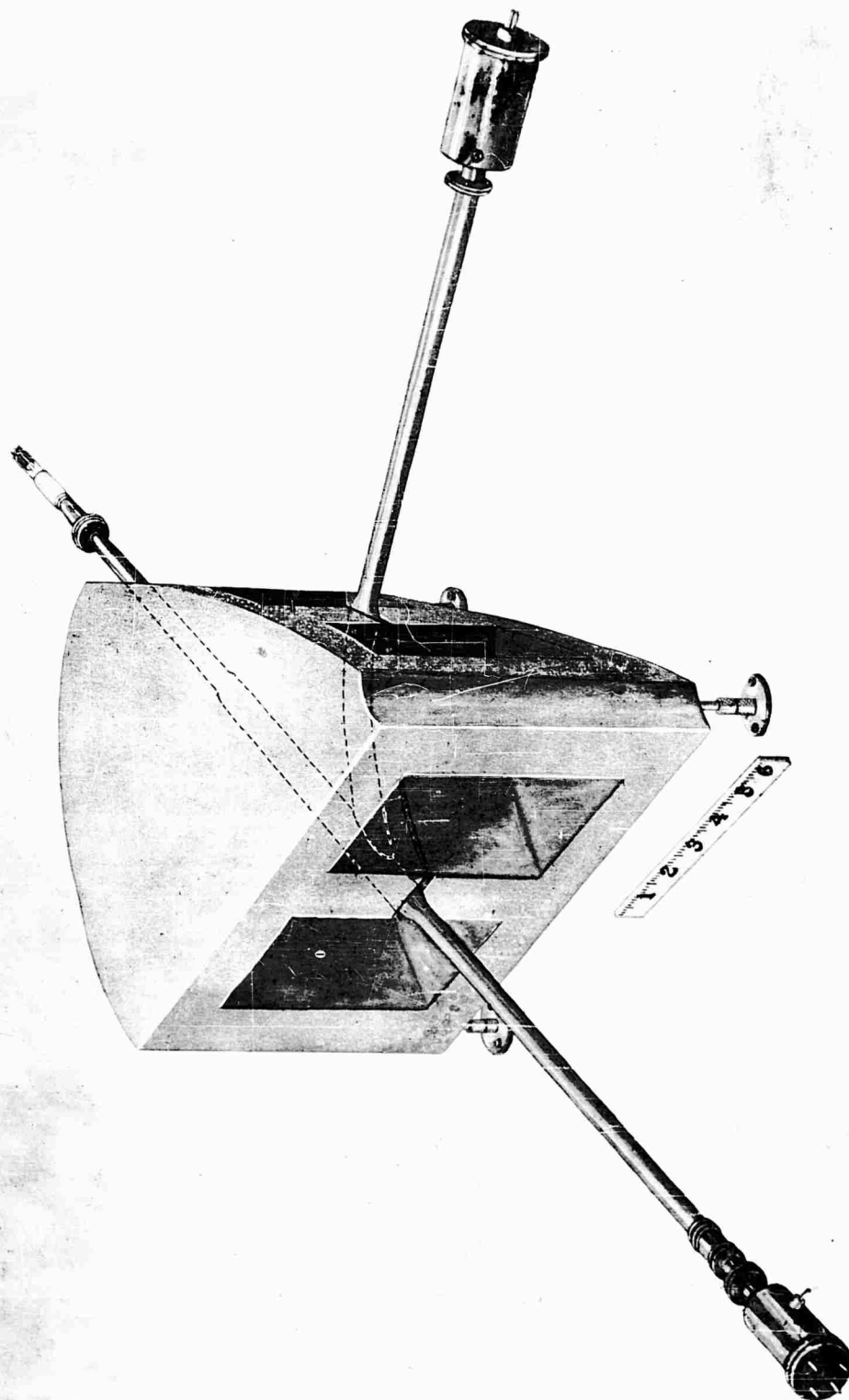
$$\rho = 144 (M_i U_B)^{\frac{1}{2}} / H$$

and

$$\sin \alpha = 6.95 (10^{-3}) (H) (L) / (M_i U_B)^{\frac{1}{2}}$$

where

$$\begin{aligned} \rho &= \text{radius of curvature, cm} \\ M_i &= \text{fuel atomic weight} \\ U_B &= \text{acceleration potential, volts} \end{aligned}$$



Sketch of Mass Spectrometer

FIGURE V-9
1944

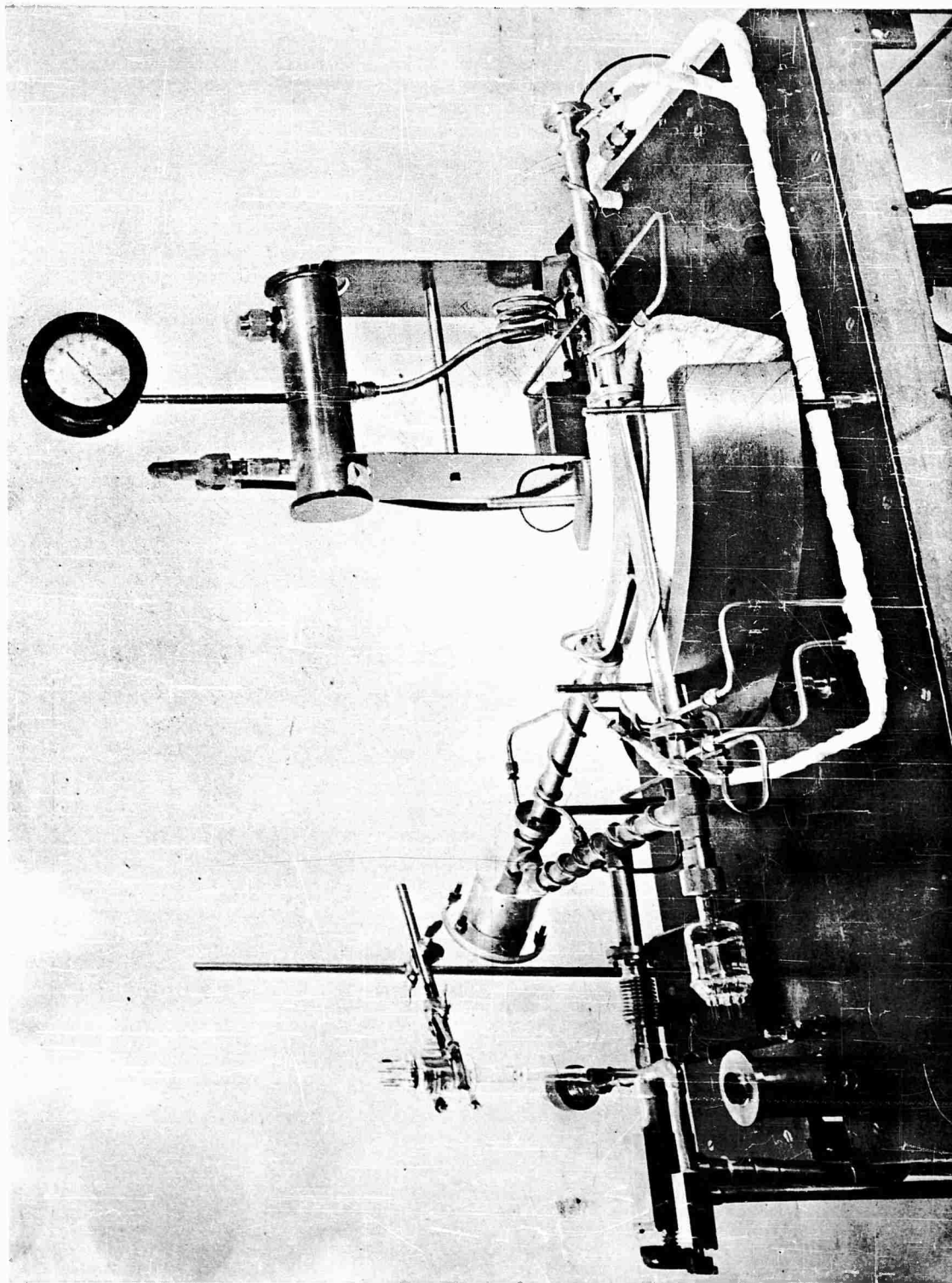


Fig. V-10 Photograph Of Mass Spectrometer

H = magnetic field strength in the gap, oersted
 L = length of deflection, cm

To provide high saturation magnetization, the metal block is made of annealed Armco Ingot Iron. Figure V-11 shows the dependence of the gap-field strength on the product of current in amperes times the number of coil turns. The slight deviation in measured value as compared to the predicted can be attributed to the annealing process. The coil is made from copper wire with 1 mm² cross-section, thus allowing a maximum current of 1 amp without block heating. For investigation of emitters with larger surface area, it is possible to enlarge the gap height to 20 mm, in which case the number of turns of the coil will be reduced from the present 6100 (both coils) to about 4500. Herzog correction and a correction of second order are included for proper focusing of the ion beam.

Beam spreading due to space charge occurs at vacua lower than 10⁻⁷ mm Hg, and limits the beam current in the mass spectrometer. The beam spreading equation is given by:

$$r_2/r_1 = [4.1 (10^6) (M_i)^{1/2} (jL/U^{3/2})]^{1/2}$$

where

r₂ = beam radius at distance L, cm
 r₁ = beam radius leaving the Pierce gun, cm
 j = current density, amp cm⁻²
 U = accelerating potential, volts
 L = distance from Pierce gun, cm
 M_i = atomic weight

The space charge can be compensated by neutralization of the beam with slow electrons, produced by collision of beam ions with residual gas atoms (gas pressures down to about 10⁻⁴ mm Hg) and by secondary electrons from the tube walls. To avoid any reaction of the fuel with the residual gas, an inert gas will be used in the tube.

The ion space charge in the uncompensated beam is given by:

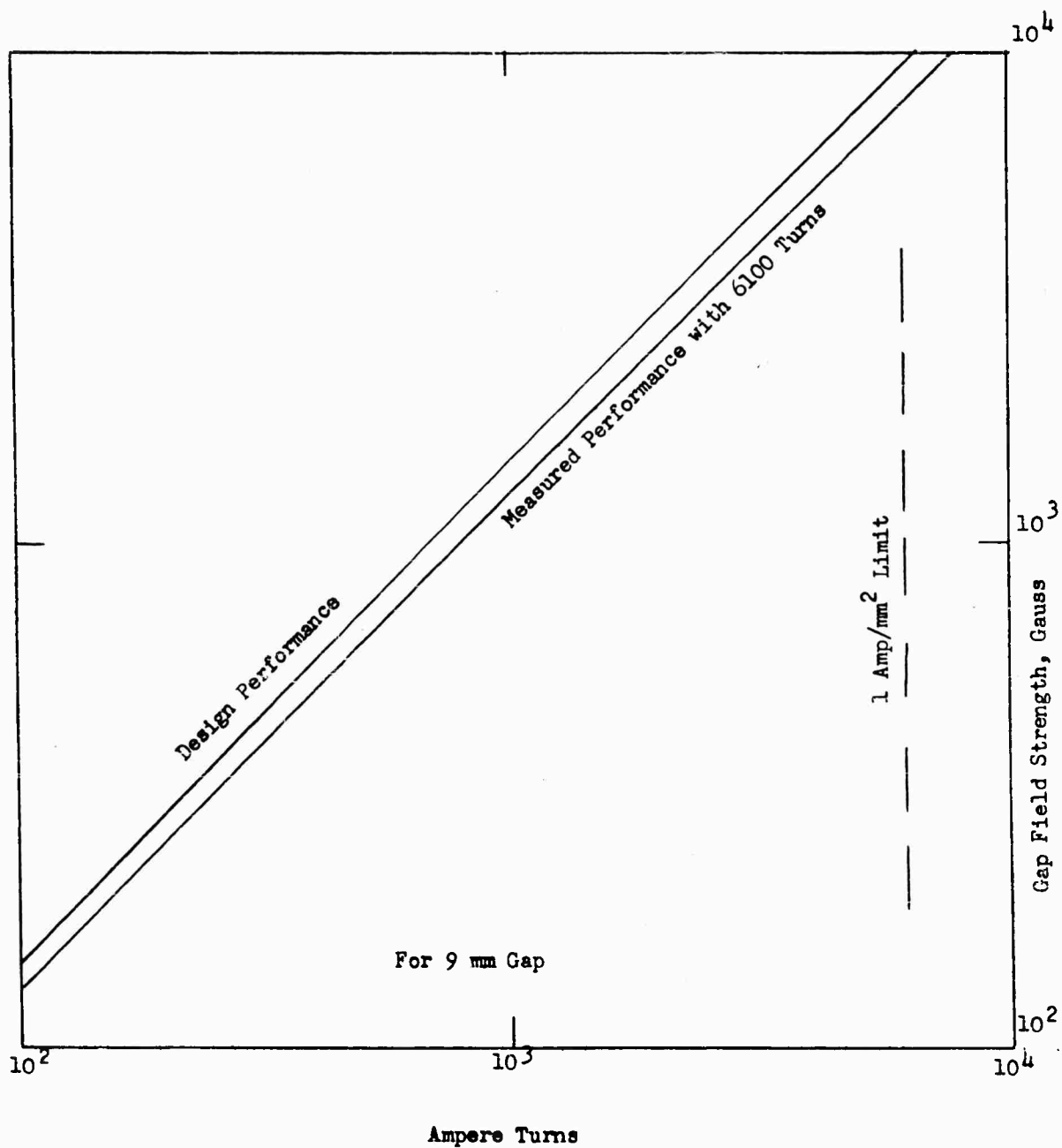
$$q_i = 6.3 (10^{18}) (j_i)/v_i$$

and the space charge compensation time is:

$$t_x = 0.73 (Q_i) (p/p^*) (M_i/U_B)^{1/2} (10^{-6})$$

where

q_i = space charge, coul cm⁻³
 v_i = ion velocity, cm sec⁻¹
 t_x = time, sec



FIELD STRENGTH IN MASS SPECTROMETER

FIGURE V-11

Q_I = differential ionization, depending on ions
and rest gas
 p/p^* = ratio of rest gas pressure to 1mm Hg.

At higher gas pressures compensation times in the order of 10^{-6} sec are possible. Investigations on the neutralization of ion beams has been published, including Bernas and Sarrouy (Ref. 72) Bernas, Kaluszyner, and Arnaud (Ref. 73), and Walcher (Ref. 75).

The mass spectrometer apparatus shown in Figure V-10 has been assembled, but was not ready for use during this first contract period.

VI. BONDING THE EMITTER

A significant effort was made in this program to provide reliable ion source data by eliminating by-pass flow around the edges of the emitter. It was the objective to have all of the fuel pass through the emitter and not around it in order to provide a true evaluation of emitter performance. In addition, although a minimal leakage can be acceptable and may not adversely affect the operation of the emitter (within the limitations described previously in Section II of this report), fuel wastage is not desirable in an engine application. This phase of the investigation on bonding methods, therefore, was given considerable engineering attention.

A method of brazing with platinum gave promising results; information is included herein on a platinum-bonded emitter which operated for 25 hours at temperatures up to 1700°K without failure and without adverse effects on ionization characteristics. Further investigation using pure refractory metals as bonding agents is recommended for higher temperature applications. Sintering the emitter directly into a holder also gave promising results and is recommended for further engineering study.

Mr. H. Szymanowski and Dr. E. Petrick conducted this phase of the work, assisted by Mr. R. Hughes, metallurgist, and Mr. L. Cowder, metallurgical technician. Mr. W. Coons performed the metallographic studies. Prof. E. Mueller suggested the technique of brazing with platinum, niobium, and iridium.

VI. BONDING THE EMITTER

Investigations have been made of methods of holding a porous sintered tungsten plate in such a manner that it can be heated to 2000 K without by-pass flow of cesium vapor around the edges of the holding arrangement. Different expansion coefficients for the materials, together with the necessity for preventing contamination of the porous media itself, complicate the problem. Four principal methods of bonding have been investigated:

- (a) mechanical joints,
- (b) brazing,
- (c) welding, and
- (d) sintering in place

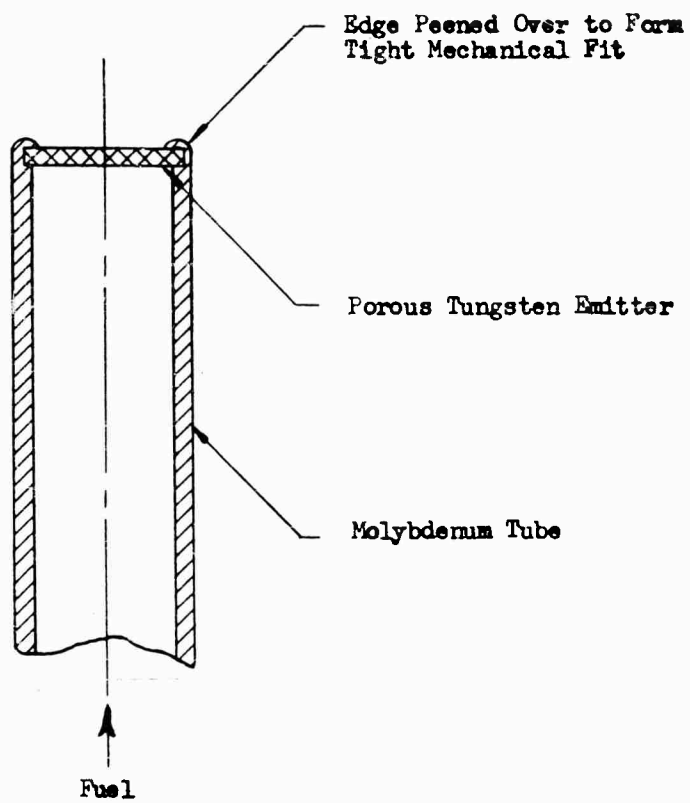
Each of the above methods is described below. At the present time, brazing with pure metals has provided the best results, although the method of sintering in place holds promise and is being further investigated.

A. Mechanical Joints

An obvious method of holding a porous tungsten plate is by means of a clamping device. Early experiments at the Quehanna Laboratories on the resistance heating of a tungsten emitter made use of a clamping method. The results indicated that if the plate is clamped tightly around the edges, in most cases cracks occur due to differential expansion. Furthermore, the rough surface of the tungsten plate is not a flat contact surface, even when tightly pressed against a completely flat mating surface. As a result, by-pass flow occurs.

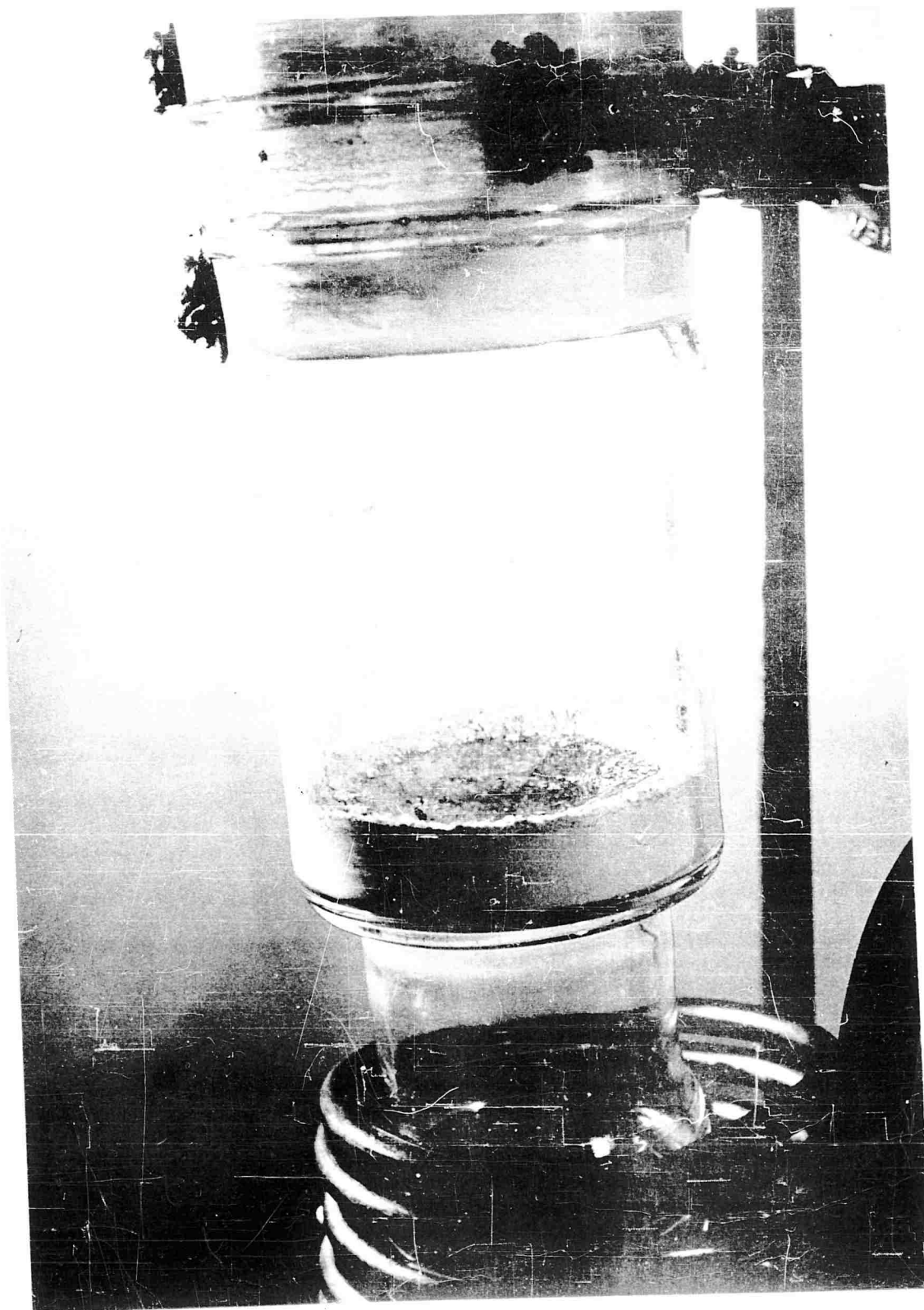
A variation of the above method of holding the porous plate is used in the commercially available "L" cathode, illustrated in Figure VI-1. The holding effect is obtained by pressing in the rim of the holding tube to obtain a pinch effect around the plate. It was noted in testing this type of emitter that by-pass occurred due to differential expansion. Furthermore, longitudinal cracks in the molybdenum holder (near the porous plate) were observed after approximately ten hours of emitter operation at temperature.

Another mechanical method is the use of a powder seal, wherein the plate is retained in a fine powder edge seal, as shown in Figure VI-2. The powder used for this test was tungsten oxide. The seal worked moderately well at room temperatures, but upon heating proved to be unsatisfactory.



"L" CATHODE

Figure VI-1



Powder Seal

FIGURE VI-2

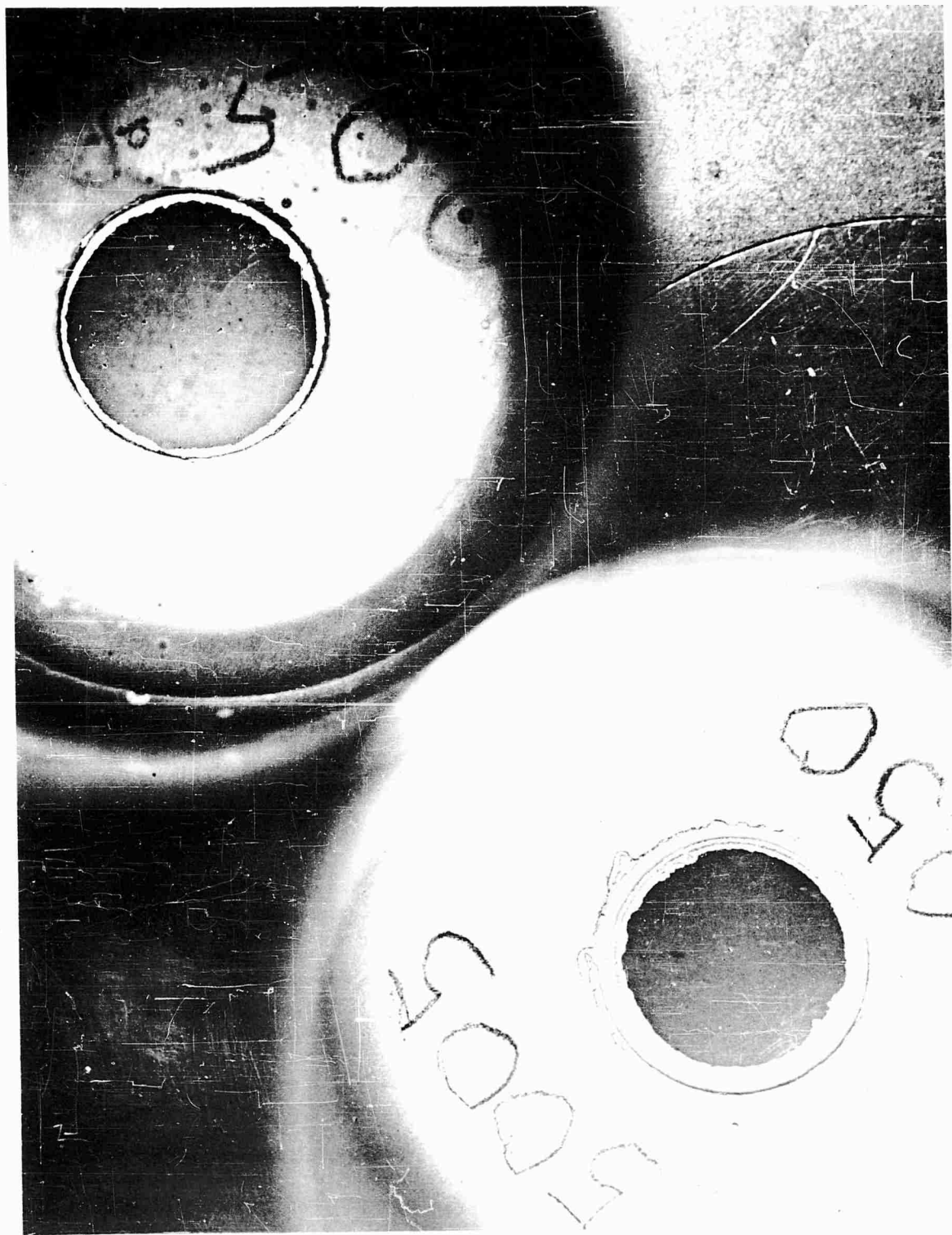
None of the above mechanical joints exhibited the desired sealing; therefore the next step was to investigate brazed joints.

B. Brazing

The drawback to any type of braze joining sintered porous tungsten to a solid material is the possible penetration of the braze material into the pores, and the possible contamination which could reduce the work function of the emitter. If such effects can be eliminated, however, a good braze joint made under controlled conditions would appear to give a measure of ductility at high temperatures between the emitter plate and the holding fixture, which is particularly advantageous when dissimilar materials with different expansion coefficients (or similar materials at different temperatures) are being used. The experiments conducted to provide an acceptable brazing technique are described below in their chronological development.

Nickel Braze: Molybdenum cups, three inches long and one and one-half inches in diameter, were used as the holders to which the porous tungsten plates were first attached. In the closed end of the cup a hole of one-half-inch diameter was bored. The normally open end of the cup was closed and attached to a quarter-inch nickel tube for pressure checking and diffusion experiments. First brazing tests were carried out with a commercial nickel compound as the braze material. The brazing set-up consisted of a Vycor tube, stoppered at each end and connected to a mechanical vacuum pump capable of pumping the system to approximately 1 micron. The braze material was applied as a powder at the edge of the hole in the top of the molybdenum cup and a porous plate (three-quarters of an inch in diameter) was placed over the hole. RF coils around the Vycor tube provided heating by induction. Power was applied slowly over a period of five to ten minutes until the nickel braze flowed, bonding the tungsten plate to the cup. In making the described brazes, three different thicknesses of porous tungsten plate were used (.030 in., .050., and 0.104 in.). The thin plates proved to be the most difficult, due to their tendency to crack, despite the fact that a very slow, controlled cooling cycle was applied over a period varying up to one hour. Another difficulty encountered was warpage in the tungsten plates, resulting in uneven brazing around the edges. In some cases at certain points the braze failed to join the two metals. The penetration, however, was not excessive, and could be controlled by the quantity of braze material used. Figure VI-3 is a close-up view of the bonded plates (.030-inch-thick plate at top left, 0.050-inch-thick plate at lower right), showing the limited spread of the braze material into the emitter surface area.

The experimental bonding technique showed promise; therefore, the next step was to use a higher temperature braze material. The nickel braze described above has a melting point of 1050°C and would unduly limit



Nickel-Brazed Porous Tungsten Plate

FIGURE VI-3

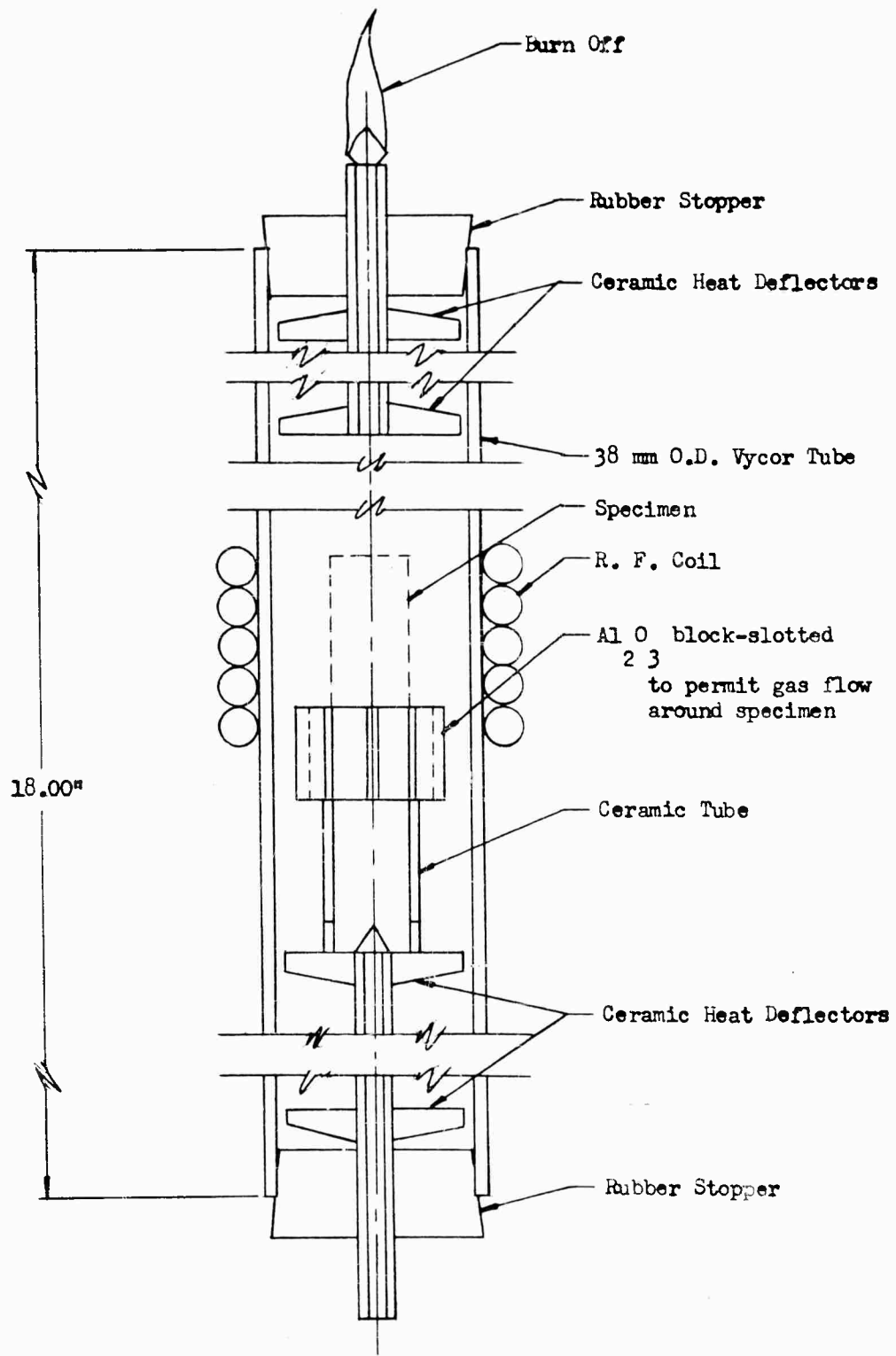
the operating temperature of the emitter, as well as increase the possibility of emitter poisoning.

Molybdenum Braze: A commercial molybdenum-boron braze material was investigated next. The material was found to be very sensitive to surface cleanliness, and frequently did not flow readily. More important, however, was the possibility that the compound would poison the emitter. It was decided that only pure metallic substances of high work function would be used for further bonding experiments; therefore, platinum was investigated next.

Platinum Braze: The inductive heating set-up for platinum brazing is shown in Figure VI-4. Before heating, the complete assembly was purged with argon gas; the heating and braze operation was conducted under a hydrogen atmosphere. The brazing temperature was between 1775°C and 1800°C, at which point the platinum flowed freely. Figure VI-5 illustrates the first configuration of emitter tube which was fabricated and joined. Better results subsequently were obtained with a somewhat modified design.

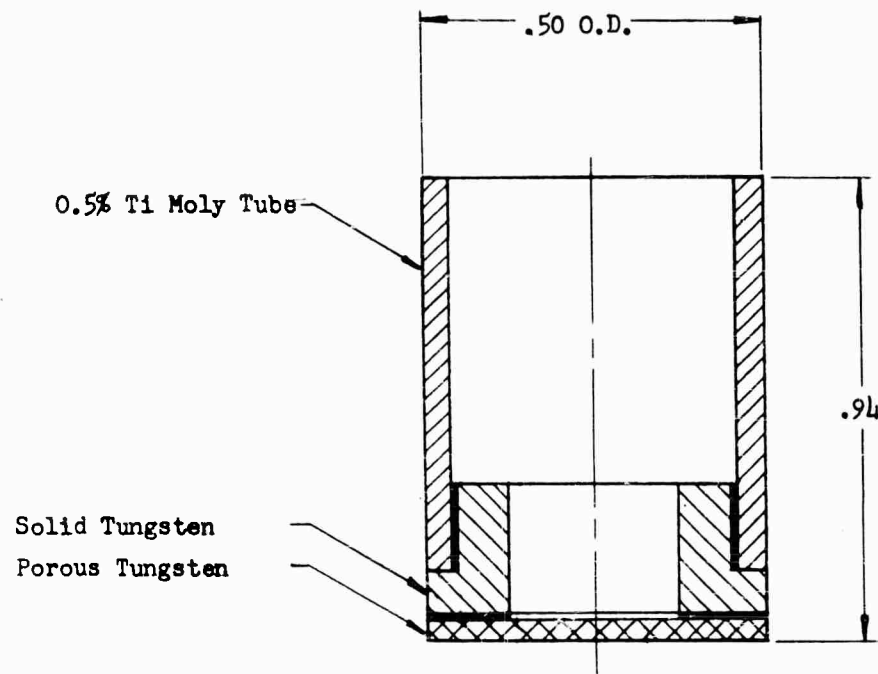
As can be seen from Figure VI-6 (before emitter tests), the porous tungsten plate was placed between two molybdenum washers. Great care was applied to ensure that the surfaces to be brazed were free from contamination by degreasing and cleaning. The platinum was applied as a thin foil, in the form of two "gaskets" on each side of the porous tungsten plate, and a thicker layer between the sides of the molybdenum washer, tungsten plate, and the sides of the molybdenum tube. After completing the braze, the specimen was subjected to a heat/cool recycling test in a hydrogen atmosphere to determine if the porous tungsten plate would crack due to differences in expansion rates, and also to determine if there would be further penetration of the brazing agent toward the center of the plate. After completion of five cycles up to 1600°C, both visual inspection and a pressure check revealed that the bond had been satisfactory. In order to measure the penetration of the platinum during the bonding process, the sample was sectioned and a longitudinal surface through the center was prepared for microscopic examination. The composite photomicrograph reproduced as Figure VI-6 shows that the bonding and the limitation of penetration were excellent. The section is taken at the edge of the plate, and includes the 0.030-inch-thick F-2 porous plate, washers, and tube. Penetration toward the center of the tube, past the inside diameter of the molybdenum washers, did not exceed the maximum penetration visible in Figure VI-6.

The problem of bonding with a braze material is a function also of the corrosion properties of the braze material in cesium. Corrosion of pure metals, including platinum, tungsten, and molybdenum is described further in Section VII of the present report but it is pertinent here to describe the results of experiments to determine the effect



TYPICAL BRAZING SET-UP

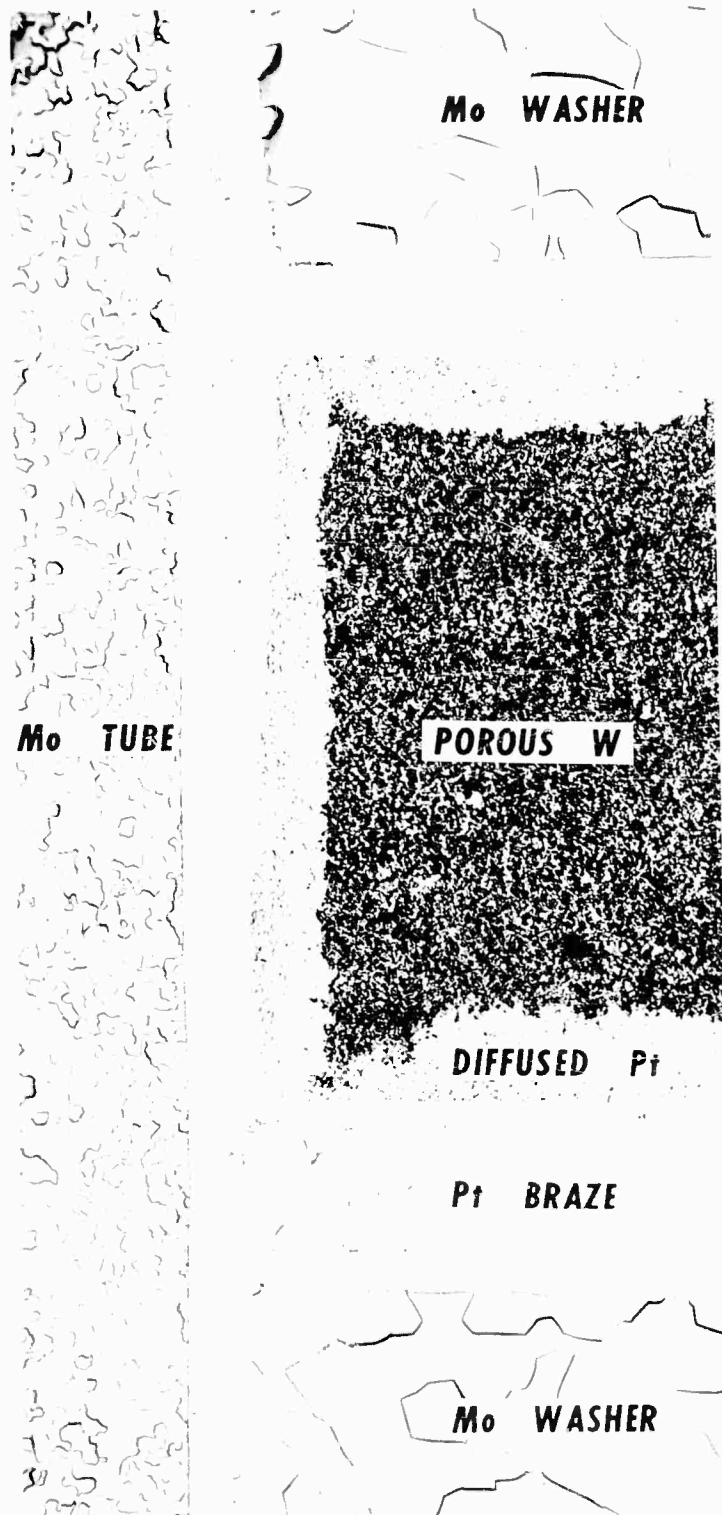
Figure VI-4
-106-



Black areas are Platinum Braze

FIRST PLATINUM BRAZE CONFIGURATION

Figure VI-5



Photomicrograph of Brazed Emitter Before Test

FIGURE VI-6

**THIS
PAGE
IS
MISSING
IN
ORIGINAL
DOCUMENT**

ORIGINAL VOIDS IN BRAZE

POROUS TUNGSTEN

CRACKS

PLATINUM BRAZE

MOLY HOLDER

EMITTER F-1 AFTER 30 - HOUR TEST

FIGURE VI - 7

naked eye. The integrity of the platinum braze material per se also is obvious. The (black) voids in the braze material are pores developed during the brazing operation and are seen also in Figure VI-6 (before emitter tests). The braze material had not diffused through the porous plate, and there is no evidence of corrosion or alloying by cesium, even at the elevated operational temperatures. The platinum did not flow over the plate surface beyond the original boundary of the brazed bond. Figure VI-8 is an overall photograph of the emitter after the test, taken from the cesium vapor side where the maximum corrosion would normally be expected. Radial cracks in the braze are evident, also a circumferential crack in the emitter at the internal diameter of the braze.

Inasmuch as the emitter operated satisfactorily until the sintering temperature was exceeded, the method of bonding with a precious metal braze material appeared to be satisfactory for 25 hours. The subsequent failure is attributed to continued sintering and shrinkage of the emitter, with failure initiated at the edge of the brazed joint.

Emitter P-1, for which ion current data are given in Section V, was operated for a total of 5 hours, in individual periods of approximately two, two, and one hour. Fuel temperature was varied up to 530K and emitter temperature up to 1650K, well below the sintering temperature of 2675K (see Section III-A). The test was terminated after 5 hours as a continuous decrease in ion emission characteristics was noted. The emitter was sectioned and studied microscopically. There was no apparent evidence of diffusion of platinum either into the pores or over the emitter surface. Since the reduced flow effect was noted in both the mechanically-bonded and platinum-bonded P-1 and P-2 plates (see Section IV) and not in the P-3 plate, the cause may in some way have been due to the plate manufacturing process. In order to definitely establish the cause, the tested P-1 emitter has been forwarded to another laboratory for X-ray and other examinations. Results will be published as a letter addendum to the present report.

It would hardly be correct to assess the bonding method as a complete success on the basis of the tests to date, although the results are promising. From the positive viewpoint, it is significant for the P-1 emitter that at operational temperatures the platinum braze apparently (1) was not affected by the cesium environment, (2) did not fill the pores of the porous emitter and (3) did not flow over the surface of the plate. On the other hand, in the platinum-bonded P-1 and mechanically-bonded P-2 emitter tests reported previously in Sections IV and V, a continuous decrease in emission characteristics was noted. A microscopic examination of P-1 did not identify platinum spreading as the cause; a further study of the emitter is being made. It is concluded on the basis of results to date that a continued investigation of bonding by means of a braze technique is warranted, and that the use of higher temperature bonding agents (such as niobium and iridium) in conjunction with sintered plates of various porosities should be included.

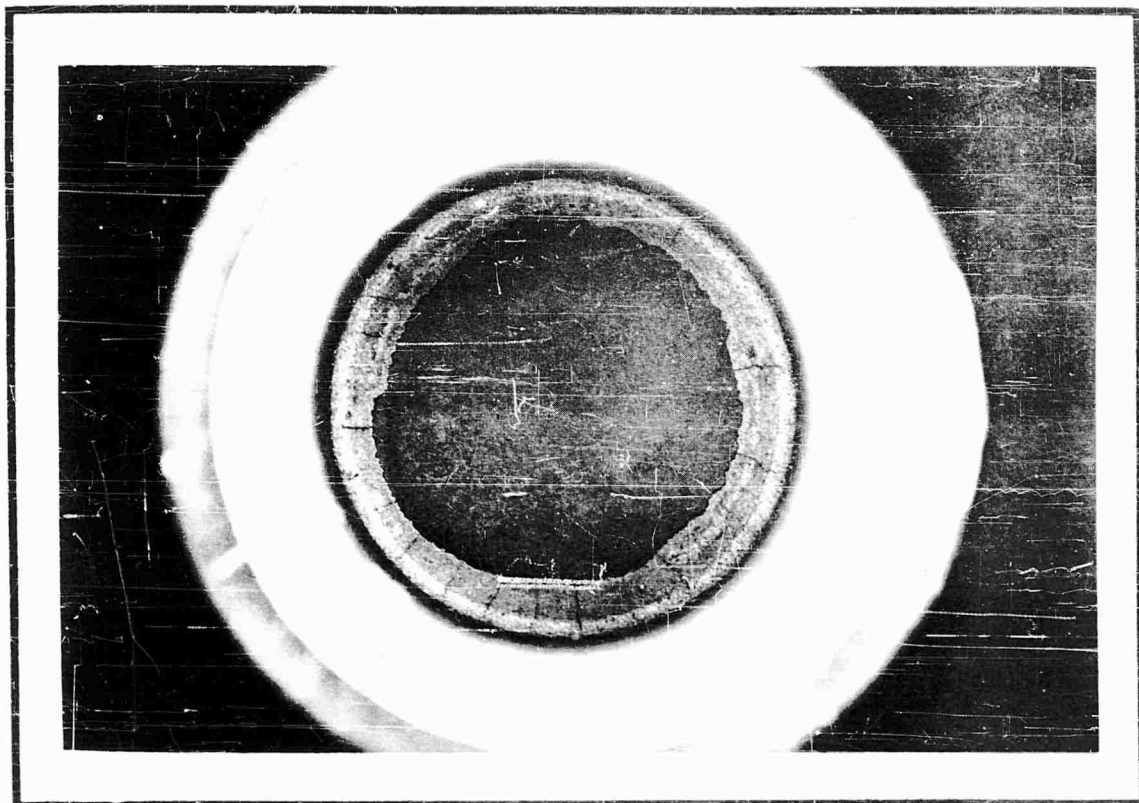


Fig. VI-8

**Photograph Of
Platinum Bonded Emitter F-1
After Test (Cesium Vapor Side)**

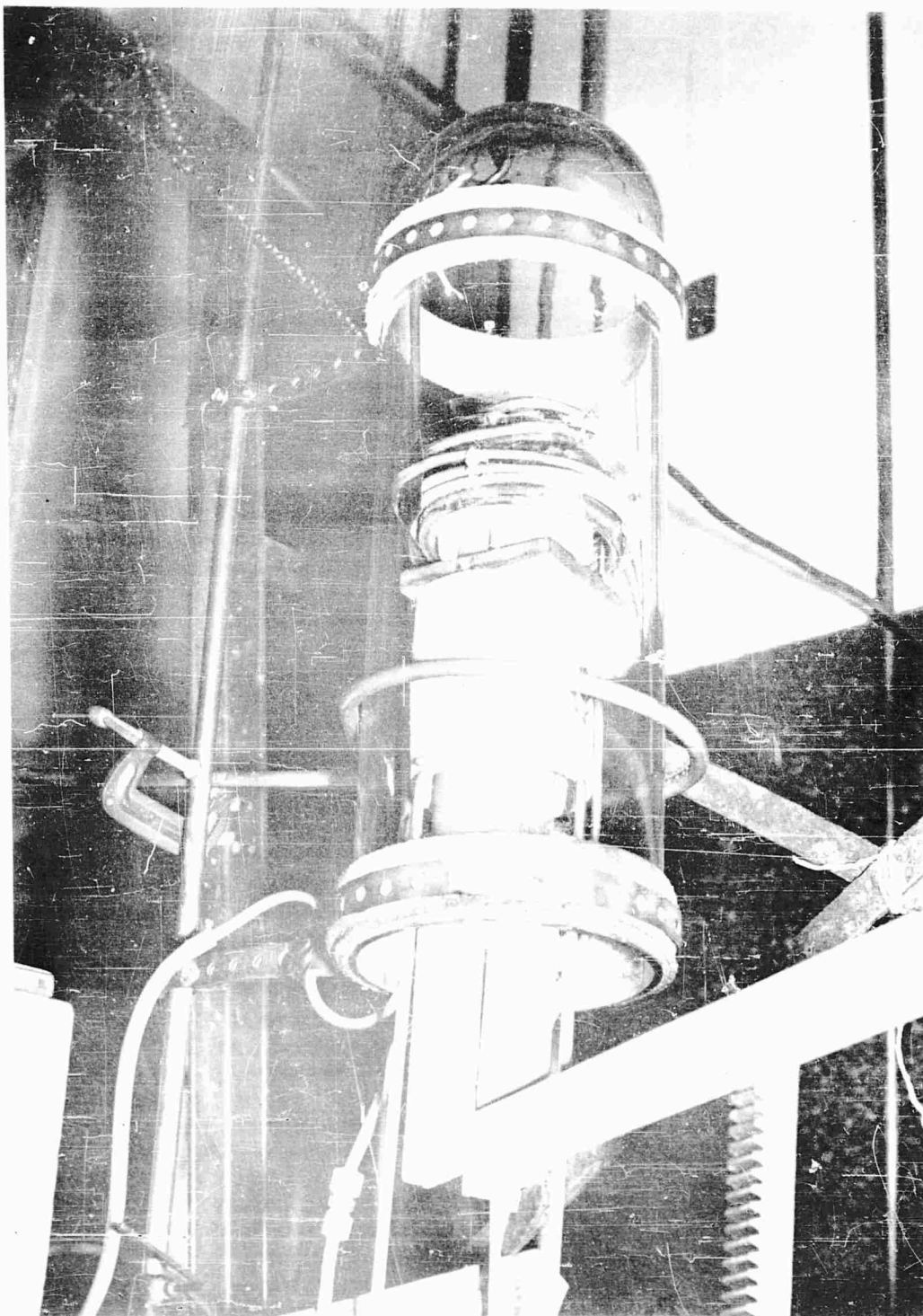
The molybdenum screen emitter described in Section III was bonded with platinum using a similar technique. No difficulties were encountered during the tests.

Ceramic Bond: In the early stages of the effort to obtain a good bonding technique to hold the porous tungsten plates, it was readily apparent that if a bond of the tungsten to a non-inductive material such as glass or ceramic could be made, a reduction in RF heating power would be possible. The investigation was undertaken by an outside vendor who had considerable experience in prototype experimental work of this nature, primarily as applied to electronic tubes.

Glass, even in the Vycor ranges, was quickly ruled out due to the considerable differences in expansion rates from that of the porous tungsten. The choice was for a joint to be attempted between a high temperature ceramic with suitable expansion coefficient, and the porous tungsten emitter. A survey of the ceramic field yielded the result that the ceramic "Triangle H.5 - Mullite" might suit the purpose. The objective was to metallize the edge of a ceramic tube to which the porous plate would then be bonded. The specified softening point of the mullite was in the order of 1700°C. During the initial metallizing process, however, it became apparent that this specification was not correct; softening occurred at 1350 to 1400°C. Despite this restriction, a number of samples were successfully metallized with a molybdenum-manganese alloy in preparation for the braze. For the purpose of the braze, a gold-palladium alloy, Permabraz #201, was selected. The alloy liquifies at 1410 C and solidifies at 1380 C.

Brazing took place in an inert atmosphere of hydrogen using RF, with a block of carbon serving as the furnace. The complete assembly of ceramic and tungsten could be lifted or lowered in respect to the RF heating coils, as shown in Figure VI-9. Although care was taken to ensure that the assembly was brought slowly up to temperature and then slowly lowered, the thermal shock proved too great for the ceramic and immediate cracking occurred. In many of the ceramic samples it was found that frequently the ceramic itself contained faults and voids. It thus became quite apparent that little could be accomplished by the further use of this type ceramic.

Preliminary tests with the ceramic material "Diamonite" offered better promise of success. The material is an impervious alumina with a softening point above 1650°C, and has been used successfully in high-power radio tubes where ceramic to metal bonding is required. Experiments on a ceramic bond, however, have been discontinued because of the inherent fragility, the possibility of emitter poisoning, and the better success obtained with the platinum braze.



RF Heating Assembly for Joining Ceramic Tube to Porous Tungsten Plate

FIGURE VI-9

1-4

C. Welding

One of the principal difficulties in welding a porous tungsten plate to a holder tube is the extreme temperature distribution encountered in the welding operation itself which, in the majority of cases, causes failure of the tungsten even before the weld is completed. This is particularly true for plates of larger diameter, in the range of one-half inch and above, and for plates of large porous volume. As an initial experiment, a small disc of porous tungsten was welded to the top of a molybdenum cup under normal atmospheric conditions, using a heli-arc weld. As expected, some oxidation took place upon the tungsten surface and edge. The cracking effects previously mentioned occurred even before completion of the weld.

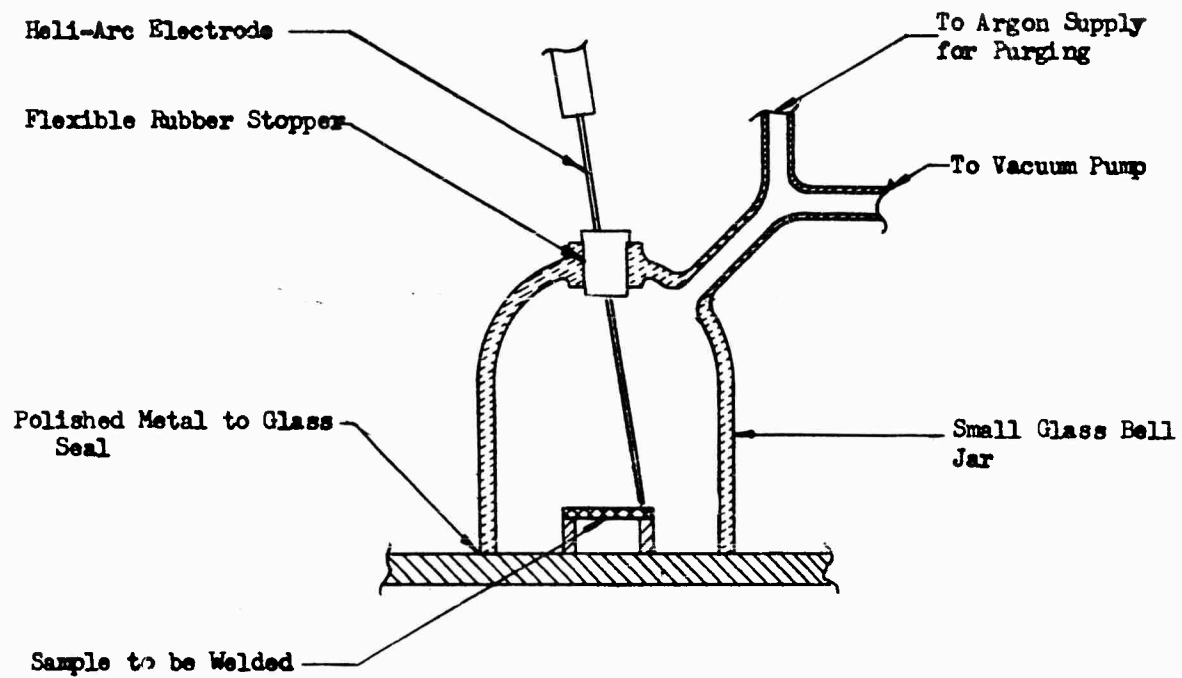
In order to reduce oxidation, a follow-up experiment was conducted by welding with a heli-arc electrode under vacuum conditions. A sketch of the apparatus is given as Figure VI-10. Due to the high temperature, the vacuum seal was not sufficient to enable the operator to successfully carry out the welding operation.

As a next step, the design was completed of a small welding rig which can be operated within the confines of a dry box containing an inert atmosphere such as argon. The welding electrode is held in a fixed position and the work piece can be rotated slowly at a predetermined speed. It is intended to investigate the welding of the porous plates (and the molybdenum screens) into a molybdenum holder, in order to fabricate a complete emitter assembly. However, the large thermal stresses during the welding operation are expected to continue to be the principal restriction to this method of bonding.

D. Sintering in Place

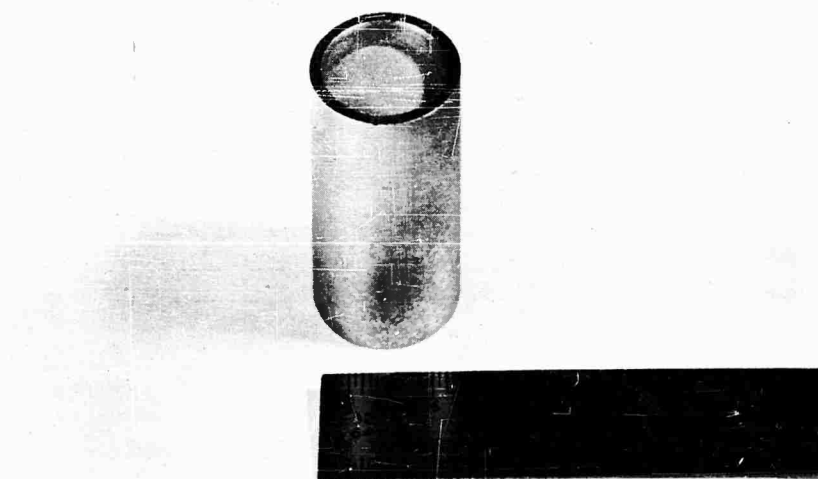
In order to eliminate the requirement for bonding, with the attendant difficulties described previously, a unique method is being investigated of sintering the porous tungsten emitter plate directly into the holder tube. To describe the technique briefly, a groove is machined on the inside wall of a tungsten tube, following which the tube is placed into a suitable die wherein tungsten powder is compacted and sintered to form a porous plate at the groove location. The fabrication technique is being investigated in conjunction with a refractory metal company which has suitable facilities. One of the emitters is shown in Figure VI-11.

In order to be acceptable, it was decided to subject the emitter assembly to five temperature cycling tests in which the temperature is raised rapidly to 1600°C, held for five minutes, and then removed. To date, promising results have been obtained; expiration of the contract period has not permitted continuation of this engineering development.



VACUUM ARC WELD APPARATUS

Figure VI-10



Porous Tungsten Plate Sintered Directly into Tungsten Tube

FIGURE VI-11

VII. CORROSION OF MATERIALS BY CESIUM

A series of tests was conducted to determine the effect of cesium on various emitter, insulator, and structural materials. Testing techniques and corrosion data are presented.

Dr. E. Petrick supervised this phase of the investigation, assisted by Messrs. H. Szymanowski, R. Hughes and W. Coons.

VII. CORROSION OF MATERIALS BY CESIUM

A. Introduction

One of the most significant problem areas in considering a cesium ion source is the compatibility with cesium of various structural materials including the ion source itself, insulators, electrodes, and conductors. Operating conditions include hundreds of hours at temperature ranges in the order of 500°K at the cesium boiler to above 1400°K at the emitter.

A literature survey failed to disclose information on the effect of cesium on various materials operating under conditions similar to those described above. A program, therefore, was undertaken to provide data which would be beneficial in the selection of materials to be used for construction of a cesium ion source.

The following sections include a discussion of the materials tested, the test methods, and the results. Three types of tests have been completed.

B. Materials

The objective of corrosion testing is to screen various materials from a compatibility viewpoint, and ultimately to establish experimentally the best materials from a durability and fabrication viewpoint. Some of the materials of initial interest included the following:

<u>Emitter</u>	<u>Insulator</u>	<u>Structure (Including Electrical Conductors)</u>
Tungsten	Aluminum Oxide	Stainless Steel
Molybdenum	Boron Nitride	Nickel
Platinum	Borosilicate Glass	Copper
	Pyrex Glass	Aluminum

In the first test series, a larger number of materials than listed above were included, as described later. The tests served to screen some of the materials; the most promising were included in the second test series. The refractory metals such as tungsten, molybdenum, and platinum were selected because of their work functions for ionization purposes, as well as for their melting points, which are above the anticipated operating temperatures and, therefore, permit their use also as structural materials. The metals may be used in the sintered porous condition, or as screens, for

ionization grids, and in solid form for structural members. Since the sintered form is composed of small particles, any detrimental effect which manifests itself at surfaces, such as corrosion, could seriously affect the strength of the emitter component. Inter-granular attack in sintered joints would make the already-brittle porous emitter even more sensitive to thermal shock. It is essential, therefore, that the effect of cesium upon the refractory metals be accurately known for high temperatures and long time periods.

The stainless steels and nickel are applicable for use as structural materials in areas of moderate temperature and will be exposed to liquid cesium or cesium vapor. The use of materials which will not be actively attacked by the cesium is desirable for long-term operation; proper selection must be made also to prevent contamination of the vapor with corrosion products which could subsequently poison the emitter and, hence, reduce the ionization efficiency.

The materials being considered for electrical conductors include aluminum, copper, and platinum, which may in some areas be exposed to cesium vapor. Aluminum is also of interest for structural members because of its light weight. Both aluminum and copper, however, are susceptible to galvanic corrosion which, added to cesium corrosion, is an obvious detriment. The use of a corrosion resistant protective coating may be mandatory if the design requires the use of these materials.

The non-metals are required for use as electrical insulators; voltages in the kilovolt range are required for ion acceleration.

C. Test Procedure

Three corrosion studies have been performed to date, using a pyrex container for the first test, a stainless steel container for the second, and fused quartz for the third. The selection of a pyrex system for the first corrosion container was made for the following reasons:

- (a) visual observation of cesium metal and specimen conditions
- (b) excellent vacuum tightness

The limiting factor in the pyrex system is the melting point, and for this reason only low temperature (500°K) corrosion tests were performed in the first test series.

For higher temperature corrosion tests, a stainless steel container was used to enclose the specimens, but this procedure had several drawbacks, namely:

- (a) visual observation could not be made of the condition of the specimens and the presence of cesium, and
- (b) exact vacuum conditions at the operating temperature were difficult to determine.

In the high temperature test, several specimens were mounted in the stainless steel corrosion chamber in order to permit the testing of a larger number of samples. At the higher temperatures, a cross-contamination effect between samples was observed; therefore in the third test series the samples were investigated on an individual basis.

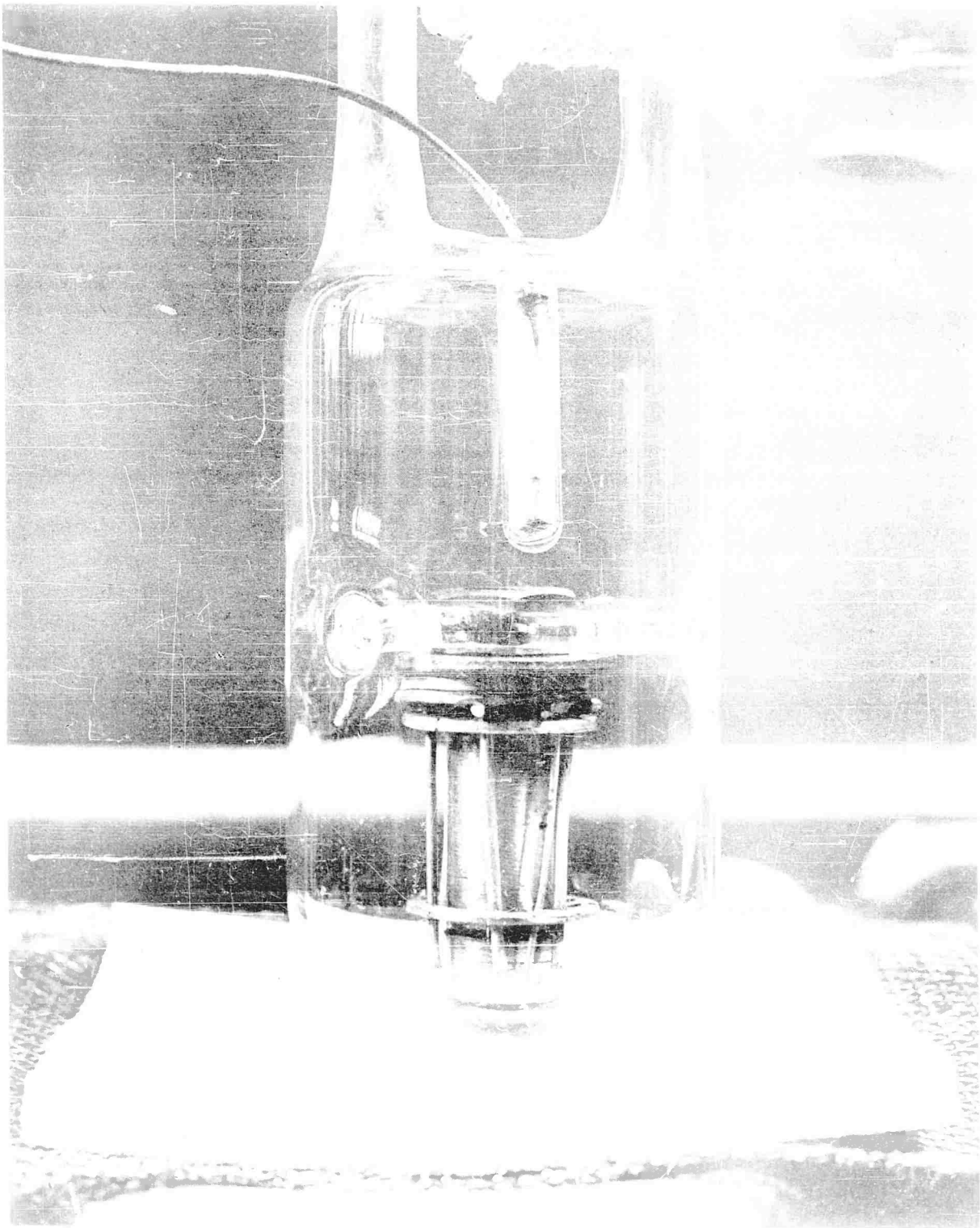
The procedure for the first two tests was as follows. The various specimens, in the form of wire or rods, were mounted on a central holder. Figure VII-1 illustrates the metallic samples mounted in a pyrex container for low temperature testing. A similar arrangement in stainless steel was used for the high temperature test. The well above the holder contains a thermocouple for internal temperature measurement during tests.

The complete apparatus for loading the pyrex container with cesium is shown in Figure VII-2. The following loading and testing procedure was used for both the pyrex and the metal containers.

The liquid-nitrogen cold trap on the right of Figure VII-2 is connected to the vacuum pump; the left cold trap is connected to an argon cylinder. The following steps are used for loading the specimen container with cesium.

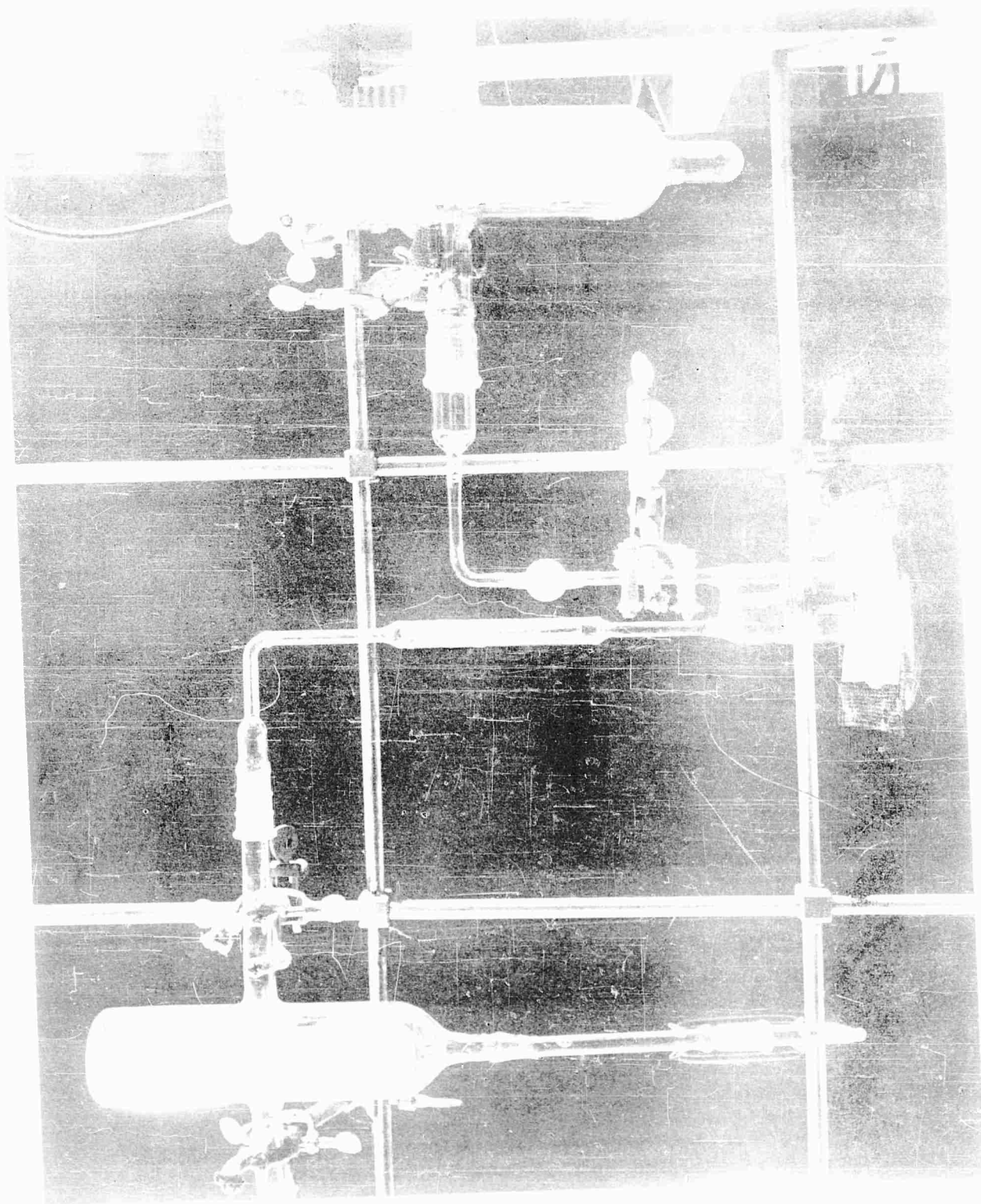
- (a) The system is alternately flushed with argon and evacuated to remove oxygen.
- (b) At the last flushing, the argon side is sealed and the system is evacuated to approximately 10^{-6} mm Hg. During this step, the apparatus is heated externally until thoroughly outgassed.
- (c) The sample container is then charged with cesium metal by fracturing the cesium ampule with an external RF field. (The cesium ampule is visible in the upper left leg of Figure VII-2 directly above the container.) Evacuation is continued to maintain a low pressure.
- (d) Finally, the container is closed by sealing the legs directly above the container. For the pyrex container, the sealing is accomplished by torch. In the case of the metallic container, the legs are metallic tubes which are forged with heat and pressure to provide a vacuum tight closure.

The evacuated sample container (with the sealed-in liquid cesium) is then placed into a controlled temperature furnace.



Metallic Sample in Glass Vacuum Chamber

FIGURE VII-1



Rate of reaction between sodium thiosulfate and hydrochloric acid

Experiment 1

1

After exposure at a given temperature for a stipulated time, the samples are removed, weighed to determine weight change, and sectioned for metallographic examination.

D. Results of First and Second Test Series

The results of the tests at low temperature conditions in a pyrex are given for metals in TABLE VII-A and for non-metals in TABLE VII-B. Exposure was for 100 hours. Referring to TABLE VII-A, nichrome, nickel, stainless steel, and tungsten were not greatly affected. The severe effect on aluminum is shown in Figure VII-3. The effect of cesium on non-metallics as shown in TABLE VII-B, indicates that the glasses could suit as low-temperature insulators, although the use of a ceramic such as aluminum oxide may be preferred from a structural consideration. The various other materials such as teflon and rubber, were included as part of the original possibilities for system gasketing. Since that time the use of such materials has not been considered further for a long-life application. The results with non-metallics, however, are of interest, although more tests would be required to confirm the data.

Certain metallic materials were next tested at a higher temperature for a longer period of time, using a stainless steel container as described previously. In some cases, as shown in TABLE VII-C, the available samples were too small in diameter for good testing and could not be evaluated. Nevertheless, the results are of interest, and served as the screening test for the third series of corrosion experiments. The test results of TABLE VII-C were further masked by various side-effects such as formation of low melting point alloys, relatively high vapor pressure of some of the elements, and oxygen contained as oxides within the specimens. Since the specimens were in close proximity to each other, these effects obscured the effect of cesium on the individual materials. As described later, the next test series was on an individual basis, but the cross-contamination effect nevertheless can be a serious one in an ion source, and requires further investigation. After the most promising individual materials are selected from the results of the next (third) test, it will be necessary to conduct a subsequent test using a technique similar to that of TABLE VII-C, wherein cross-contamination effects in a cesium environment again can be ascertained.

As an illustration of the results of the second corrosion test (Table VII-C), photomicrographs of the more interesting materials are given in Figures VII-4 through VII-8.

All of the figures pertain to 450 hour exposure at 1275°K. Molybdenum, shown in Figure VII-4, indicates no apparent change due to corrosion, but long-time exposure at temperature has caused approximately fifty

percent recrystallization. The effect on niobium is shown in Figure VII-5. The dark gray area near the specimen edge is copper contamination. There is a distinct spongy effect caused by corrosion and alloying.

The result with Inconel X is given in Figure VII-6. The corrosion attack on the surface and the spongy condition are apparent. The grey particles indicate a new phase.

For stainless steel (SS 308), the photomicrographs are reproduced in Figure VII-7. The high carbon content in the untested specimen is indicated by the black spots. After testing, oxides are present at the surface and carbide is reprecipitated at the grain boundaries. These carbides will remain at grain boundaries through the 800°-1300°F range. At this temperature, this would cause the stainless to be subjected to increased intergranular corrosion in this area.

Perhaps the most dramatic result was obtained with iridium, as shown in Figure VII-8. The black area indicates porosity, the darker gray areas are copper-gold alloying, and the light gray area is iridium.

Since the experimental results were obscured by cross-contamination, a third test series was conducted.

TABLE VII-A. EFFECT OF A CESIUM ATMOSPHERE ON VARIOUS METALS*

<u>Materials</u>	<u>Weight Change</u>	<u>Results of Surface and Photomicrographic Examination</u>
Nickel	0.10% loss	No apparent effect except loss of luster.
18/8 Stainless	0.25% loss	No apparent effect. Loss of luster and some surface staining.
Porous Sintered Tungsten	0.34% gain	Slight discoloration & staining.
Nichrome	0.12% loss	No apparent effect except loss of luster.
Mild Steel	0.04% loss	Some surface pitting.
Aluminum	0.76% loss	Localized erosion and corrosion. Metal removal & intergranular corrosion. Surface pitting.
Copper	2.10% loss	Small layer of scale on surface.
Silver Solder	0.32% loss	Slight surface pitting. Single phase layer at surface increased in thickness.
Brass	0.13% gain	Surface pitting.

* Conditions: 100 hours exposure at 575°K; vapor pressure 2mm Hg.

TABLE VII-B. EFFECT OF CESIUM ATMOSPHERE ON VARIOUS NON-METALLIC MATERIALS
(Conditions 100 hr. exposure at 480°K)

<u>Material</u>	<u>Weight Change</u>	<u>Remarks</u>
Teflon	9.7% loss	Color change from white to black
Graphite-Teflon Compound	0.1% gain	Slight darkening from gray to black
Duroid	3.2% gain	Color change from buff to black
Rubber, Type 18007	1.1% loss	No apparent change
Rubber, Type 66-018	5.7% loss	Color change from green to green-white
Asbestos Cloth	15.7% loss	Color change from white to black
Al Oxide Insulator	2.6% gain	No apparent change
Nylon Cloth	27.8% loss	Color change from white to brown
Pyrex Glass	0.2% gain	No apparent change
Vycor Glass	8.9% loss	No apparent change. Weight change result appears to be questionable
Tungsten Glass	0.2% loss	No apparent change
Soft Glass	0.1% loss	No apparent change
Natural Rubber	1.8% loss	No apparent change
Zr Oxide Ceramic	0.5% gain	No apparent change
Technical G Cement (Copper Base)		Reduced to copper. Disintegrated when tube opened to atmosphere
Sauereisen Cement (Zirconium Oxide)		No apparent change in tube, but disintegrated when tube opened to atmosphere

TABLE VII-C. SECOND CESIUM CORROSION TEST WITH METALS
(450 hours at 1275°K)

<u>Material</u>	<u>Sample Diameter (Inches)</u>	<u>Gram Wt. Before Test</u>	<u>Gram Wt. After Test</u>	<u>Gram Wt. After Wash and Dry</u>
Copper	.048	0.3333	Disappeared	
Gold	.030	0.2759	*	
Platinum	.032	0.3541	*	
Tungsten	.010	0.0370	*	
Niobium	.061	0.4491	.5194	.5188
Tantalum	.010	0.0242	*	
Molybdenum	.125	2.4031	2.4041	2.4089
Titanium	.030	0.0685	*	
Nickel	.062	0.5718	.5927	.5928
Inconel "X"	.062	0.5260	.5333	.5332
Stellite 25	.069	0.5299	.5295	.5296
Iron	.063	0.5259	.5259	.5257
Mild Steel	.093	1.0556	1.0579	1.0578
SS 308	.062	0.4781	.4802	.4801
SS 410	.198	3.2113	3.2120	3.2119
Iridium	.0605	0.1677	.2545	.2546

* Denotes samples which could not be evaluated due to small diameter.



Before



After

Photomicrograph of Aluminum Sample Exposed to
Cesium Vapor at 575°K for 100 Hours (500X)

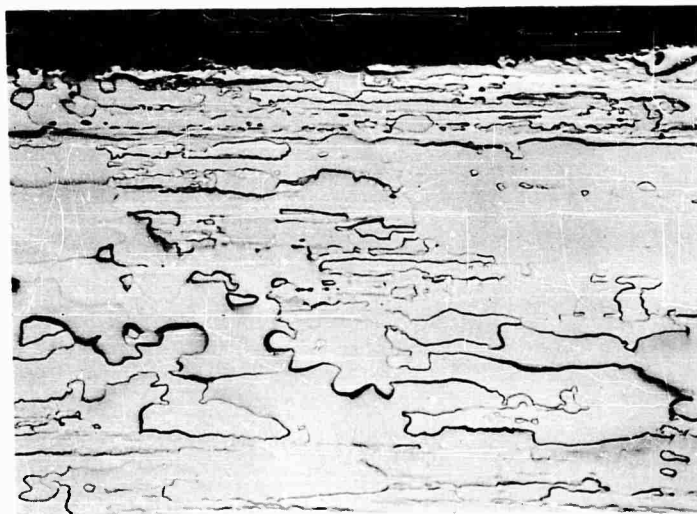
FIGURE VII-3



M-877

(a) Before

250X



M-878

(b) After

250X

Molybdenum Before and After Second Cesium Corrosion Test

FIGURE VII-4

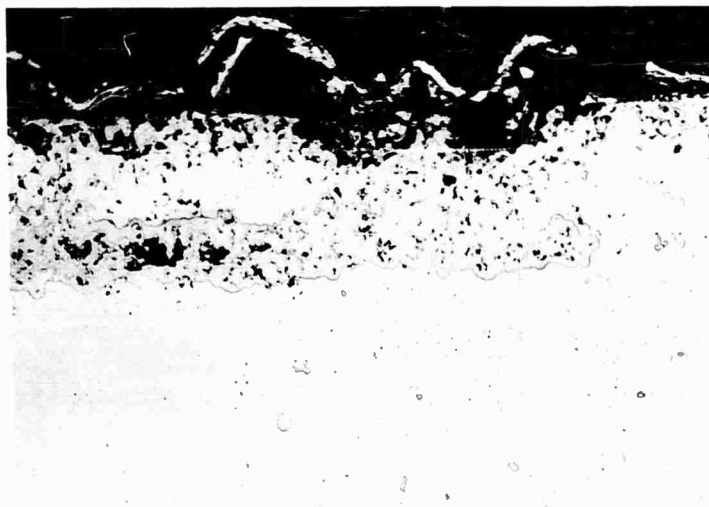
-130-



M-661

(a) Before

250X



M-871

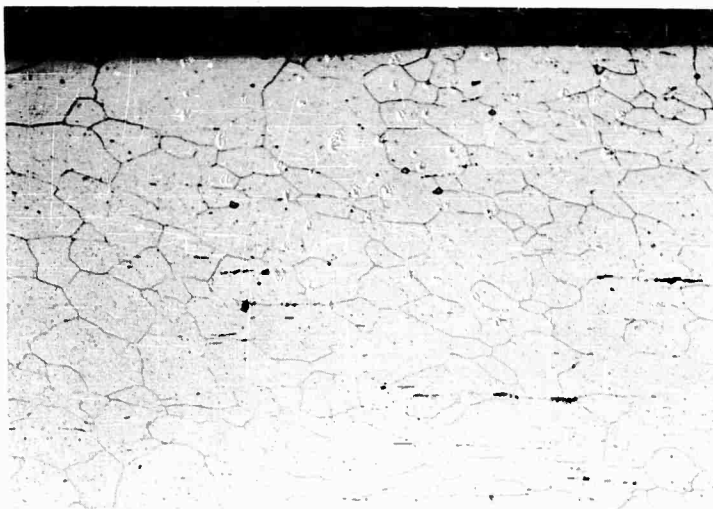
(b) After

250X

Niobium Before and After Second Cesium Corrosion Test

FIGURE VII-5

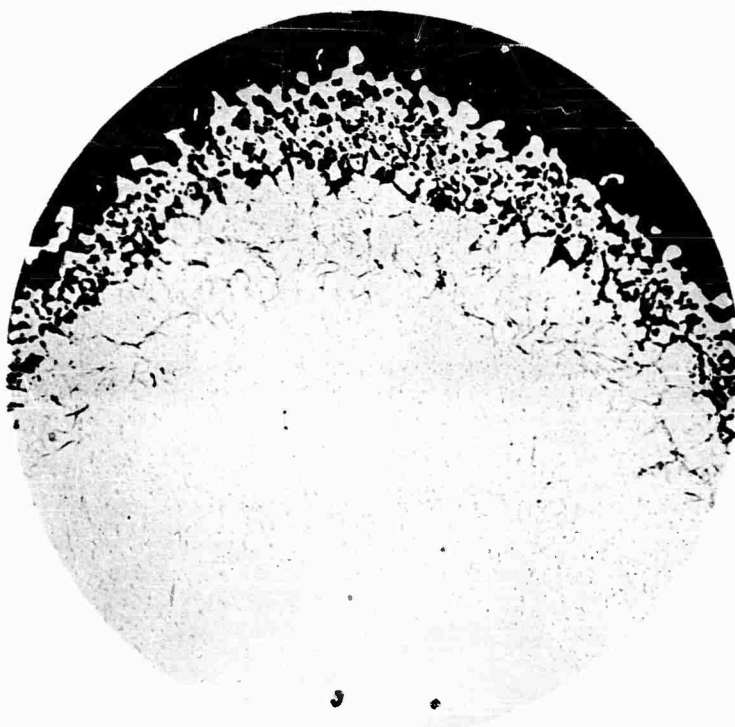
-131-



M-883

(a) Untested, Etched

250X



M-851 Inconel X Before and After Second Cesium Corrosion Test 250X

(b) After Test

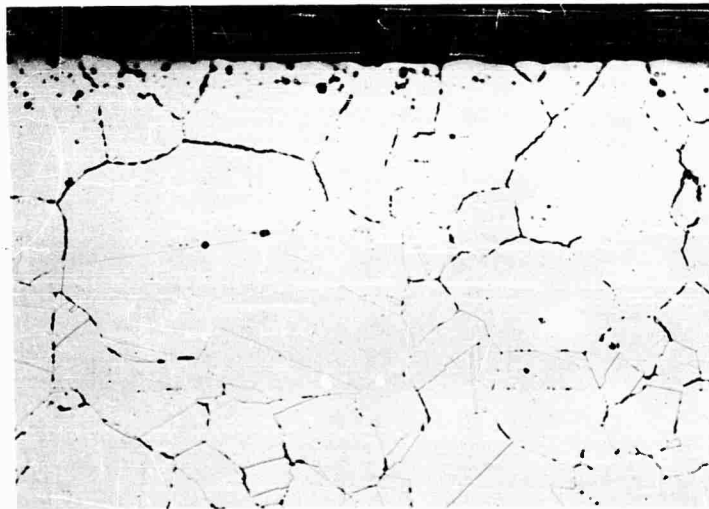
FIGURE VII-6



M-882

(a) Before Test, Etched

250X



M-884

(b) After Test

250X

Stainless Steel 308 Before and After Second Cesium Corrosion Test

FIGURE VII-7

-133-



M-861

(a) Before

250X



M-858

(b) After

300X

Iridium Before and After Second Cesium Corrosion Test

FIGURE VII-8

E. Third Test Phase

Based on the previous test results, and considering the requirements for the ion source, the materials chosen for further corrosion testing included the following:

<u>Emitters</u>	<u>Structure</u>	<u>Electrical Conductor</u>	<u>Insulator</u>
Tungsten Molybdenum Platinum	Nickel Stainless Steel 410	Copper	Aluminum Oxide

Copper didn't appear to be particularly promising for the conductor (based on previous results in the cesium environment) but platinum served here as a possible back-up for high-temperature applications.

Four specimens of each of the above materials were prepared, cleaned, measured, and accurately weighed. One specimen was mounted in a metallographic mount for study and photographing in the untested condition. The remaining three specimens were loaded into individual clear fused quartz vials, charged with cesium metal (97% purity) and vacuum-sealed. The charged vials were then divided into three groups for heating (200 hours at 520°K, 770°K, 1270°K, respectively). After test, the vials were unloaded and the samples accurately weighed and measured, followed by photomicrographic examination. Results are given in TABLE VII-D.

The results of the third test series indicate that tungsten, molybdenum, and aluminum oxide stood up well, as in previous tests. In each case Specimen "3" could not be used due to failure of the fused-quartz containers. The Specimen "2" containers showed evidence of crazing, therefore the surface discoloration for platinum, nickel, and stainless steel may be due to oxidation from the atmosphere. In the case of platinum, the extreme weight loss and surface effect was not evident in the emitter test results reported previously in Section VI and shown in Figures VI-7 and VI-8.

For the tests at 530K all specimens gave satisfactory results with no evidence of corrosion.

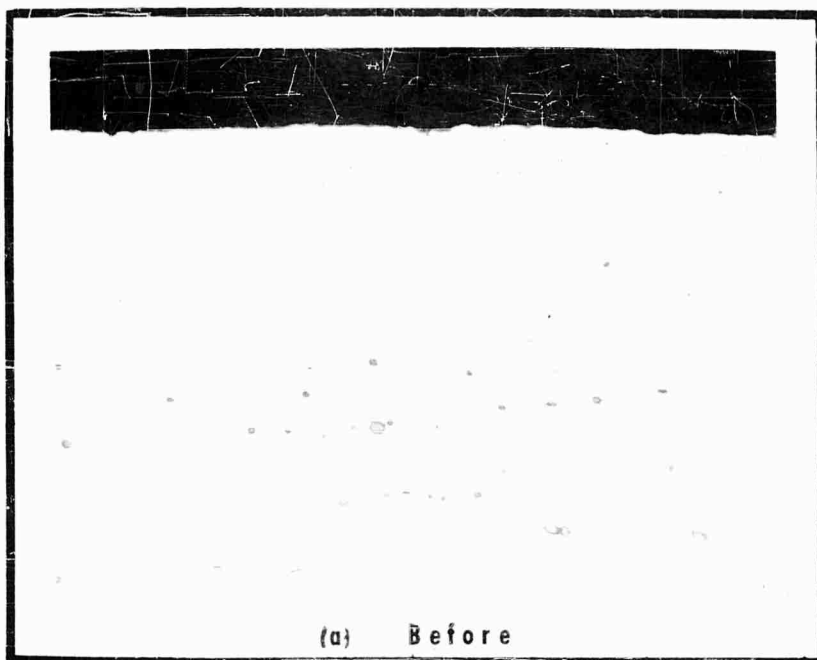
TABLE VII-D
RESULTS OF THIRD CORROSION TEST

Conditions: (a) Specimens sealed in individual clear quartz vials with liquid cesium.
(b) Specimen 1 exposed at 520K for 200 hours.
(c) Specimen 2 exposed at 770K for 200 hours.
(d) Specimen 3 exposed at 1270K for 200 hours.
(e) See comments in text for interpretation of these results.

Specimen	Original Wt., gms	Orig. Surface Area, cm ²	Weight Change, Mg	Mg/cm ²	Remarks After Test	
					Visual Inspection	Metallographic Inspection
Copper 1						Original specimen showed oxide inclusions (Fig. VII-9(a)).
Copper 1	3.8062	5.816	40.70	40.12	Specimen coated	Coating on surface apparent. No porosity in copper. Oxides still present (Fig. VII-9(b)).
Copper 2	3.6553	5.671	42.50	40.44	Surface dull	No oxides. Porosity in copper apparent. (Fig. VII-10).
Copper 3	3.8958	5.918	-----	-----	Vial broken	No result.
Platinum 1	0.6891	1.395	40.40	40.29	No change	No change. Same as Fig. VII-11(a).
Platinum 2	0.7193	1.456	45.30	38.66	Surface dull	Surface spongy (0.0008" thick). No intergranular corrosion (Fig. VII-11(b)).
Platinum 3	0.7362	1.456	-----	-----	Vial broken	No results.

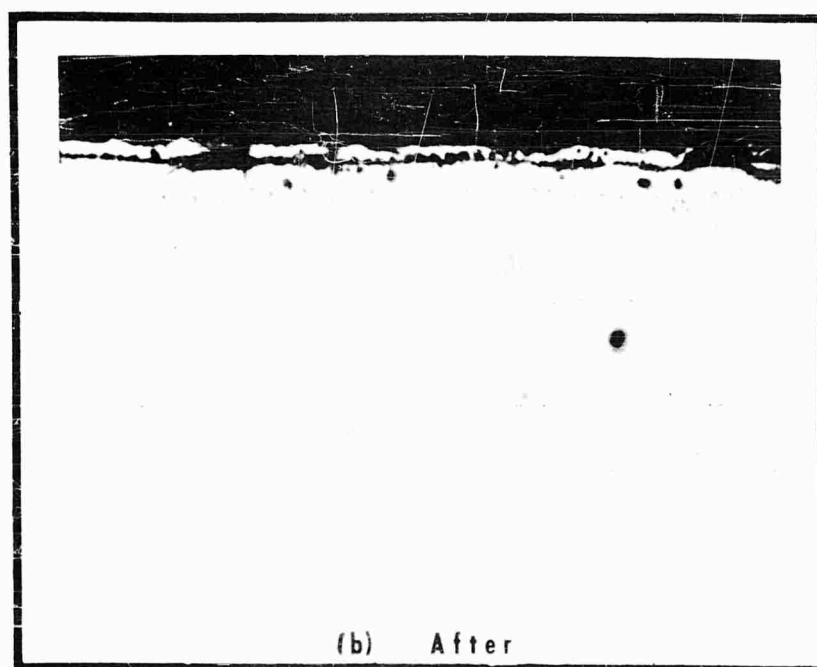
TABLE VII-D (cont)

Specimen	Original Wt., gms	Orig. Surface Area, cm ²	Weight Change Mg	Mg/cm ²	Remarks After Test	
					Visual Inspection	Metallographic Inspection
Tungsten 1	6.2622	6.520	-1.50	-0.23	No change.	No change.
Tungsten 2	5.7669	5.816	-0.30	-0.05	Surface discolored.	No change (Fig. VII-12).
Tungsten 3	5.6110	5.689	----	----	Vial broken.	No results.
Moly 1	0.7949	4.516	0	0	No change.	No change.
Moly 2	0.8090	4.615	+0.30	+0.07	No change.	No change (Fig. VII-13).
Moly 3	0.7561	4.740	----	----	Vial broken.	No results.
Nickel 1	1.4138	3.418	+0.20	+0.06	No change.	No change.
Nickel 2	1.2620	3.207	+0.38	+0.12	Black discoloration.	Nickel oxide coating presumed. No intergranular corrosion. (Fig. VII-14).
Nickel 3	1.5490	3.642	----	----	Vial broken.	No results.
SS410-1	2.4609	5.366	-0.40	-0.07	No change.	No change.
SS410-2	2.5527	5.525	+9.70	+1.76	Brown discoloration.	Oxide coating. No intergranular corrosion (Fig. VII-15).
SS410-3	2.5320	5.497	----	----	Vial broken.	No results.
Al ₂ O ₃ -1	2.9900	6.984	-0.40	-0.06	No change.	No change.
Al ₂ O ₃ -2	2.7408	6.430	+0.10	+0.02	Spotted discoloration.	No change.
Al ₂ O ₃ -3	2.7221	6.355	----	----	Vial broken.	No results.



M-1217

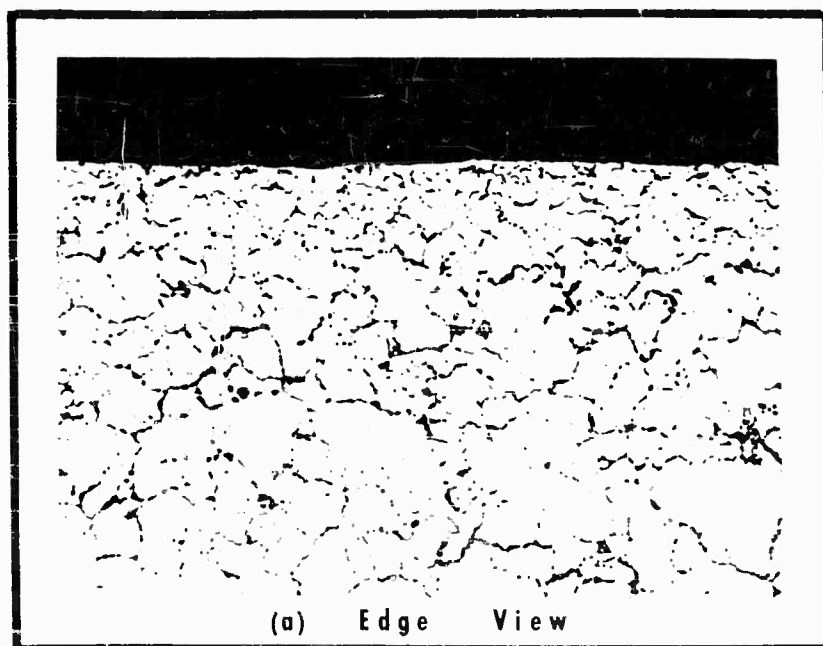
600X



M-1220

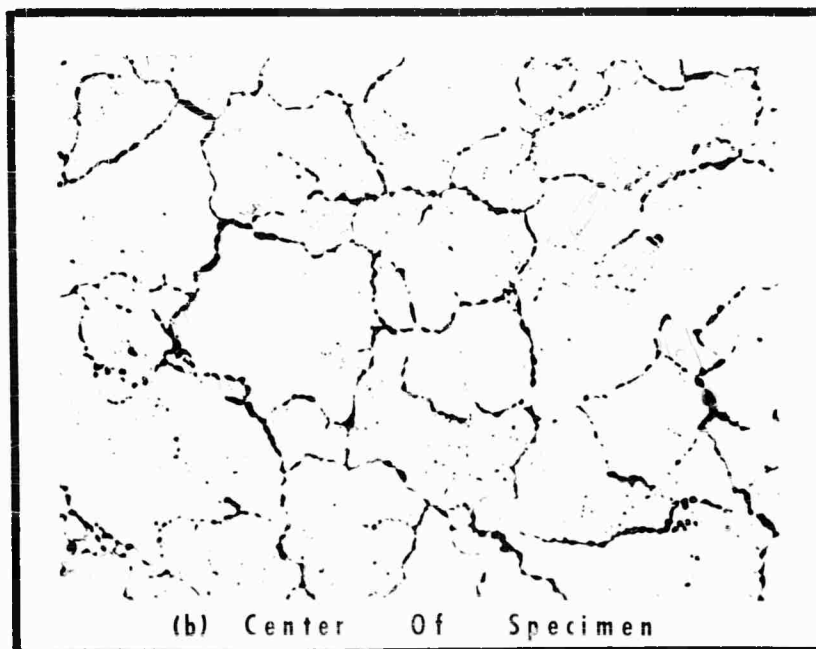
600X

Copper 1
Before And After Third Cesium Test
 Fig. VII-9 (200 Hours At 520K)



M-1222

100X



M-1221

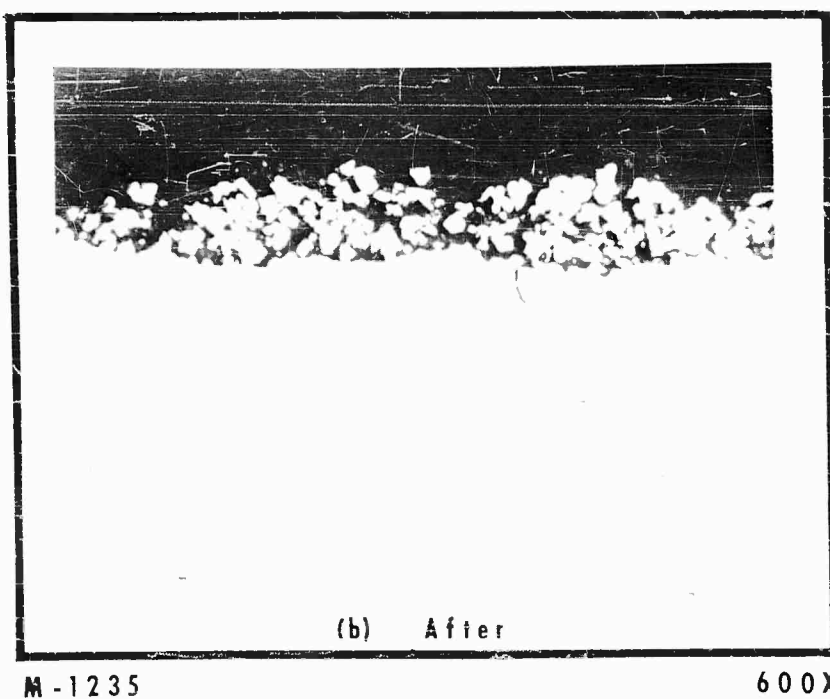
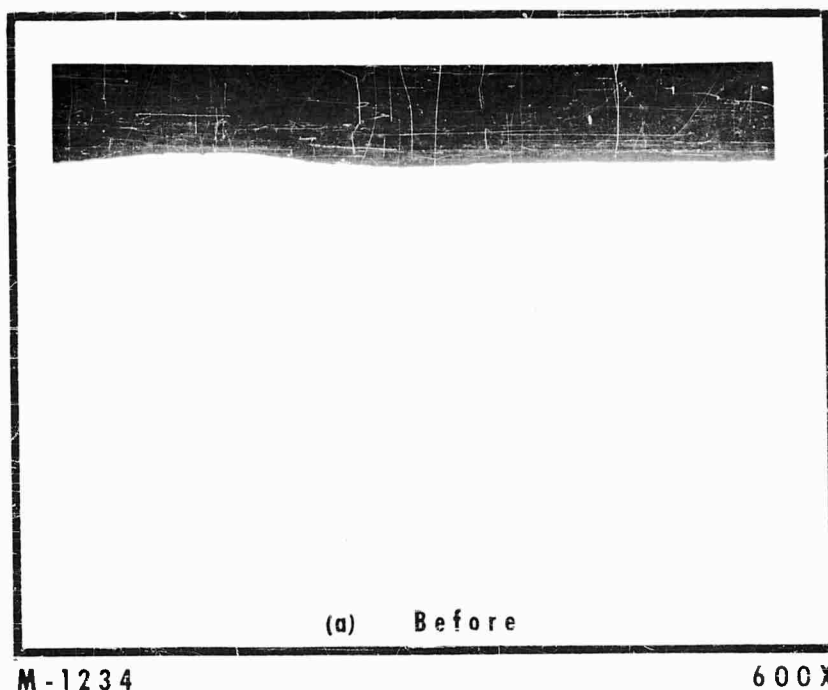
100X

Copper 2

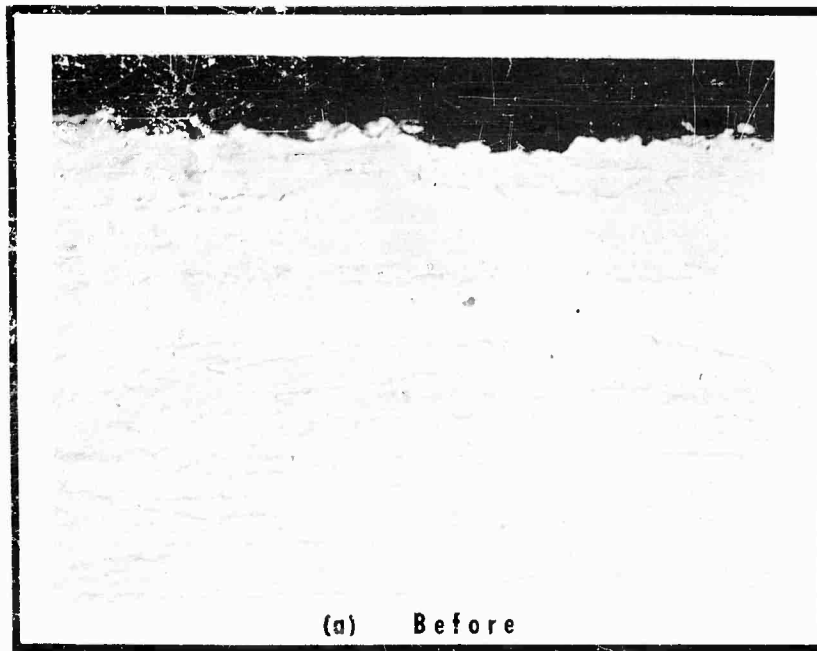
After Third Cesium Corrosion Test

Fig. VII-10 (200 Hours At 770K)

Page 139



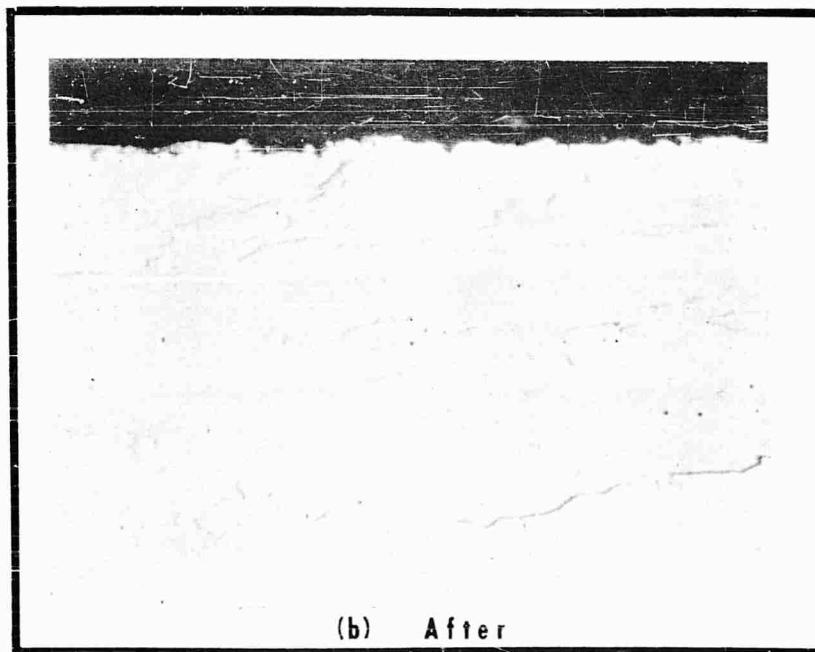
Platinum 2 Before And After Third Cesium Corrosion Test



(a) Before

M-1215

600X

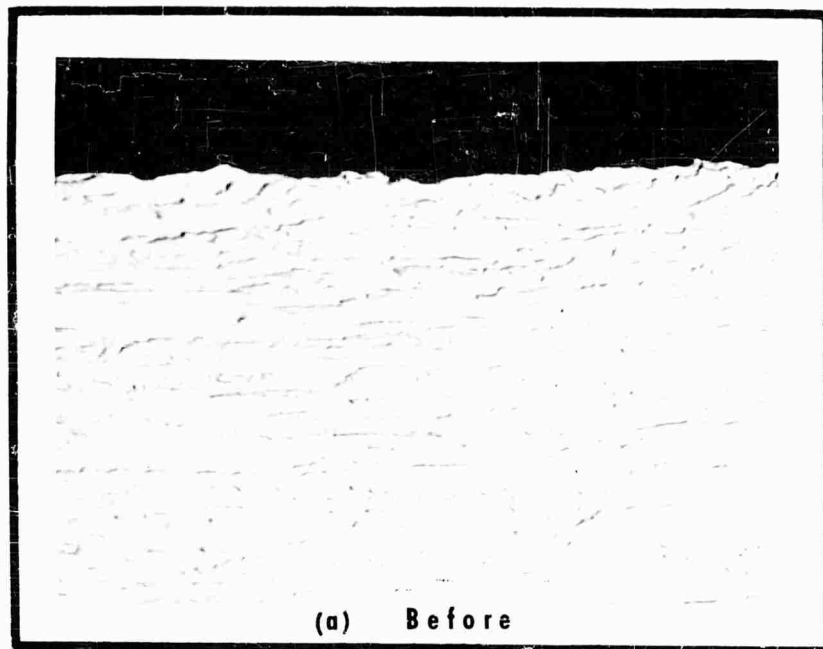


(b) After

M-1216

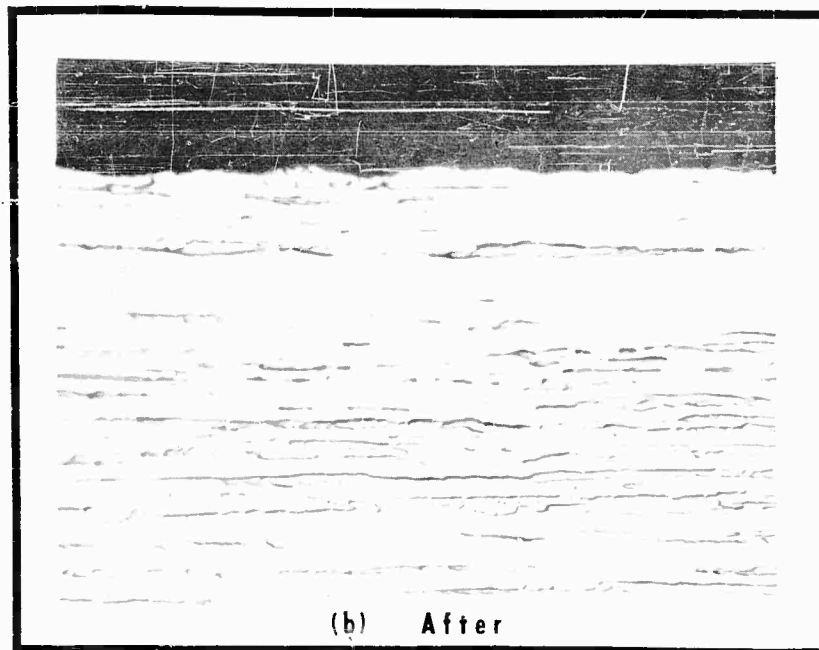
600X

Tungsten 2 Before And After Third Cesium Corrosion Test



M-1213

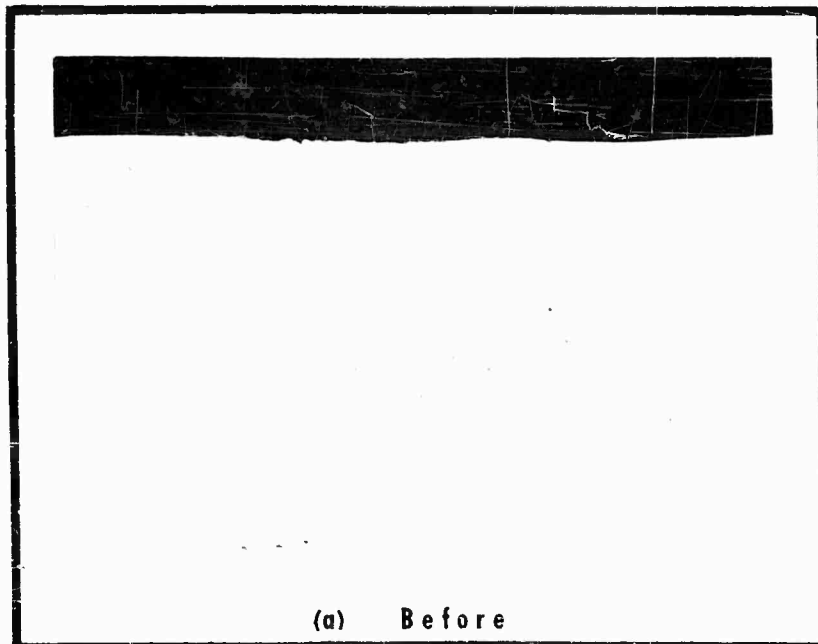
600X



M-1214

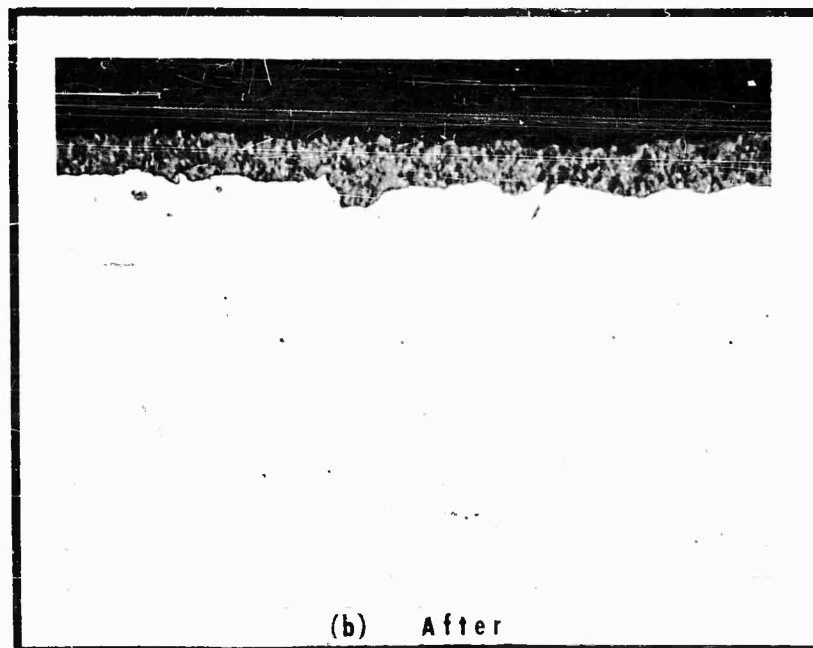
600X

Molybdenum 2 Before And After Third Cesium Corrosion Test



M-1225

600X



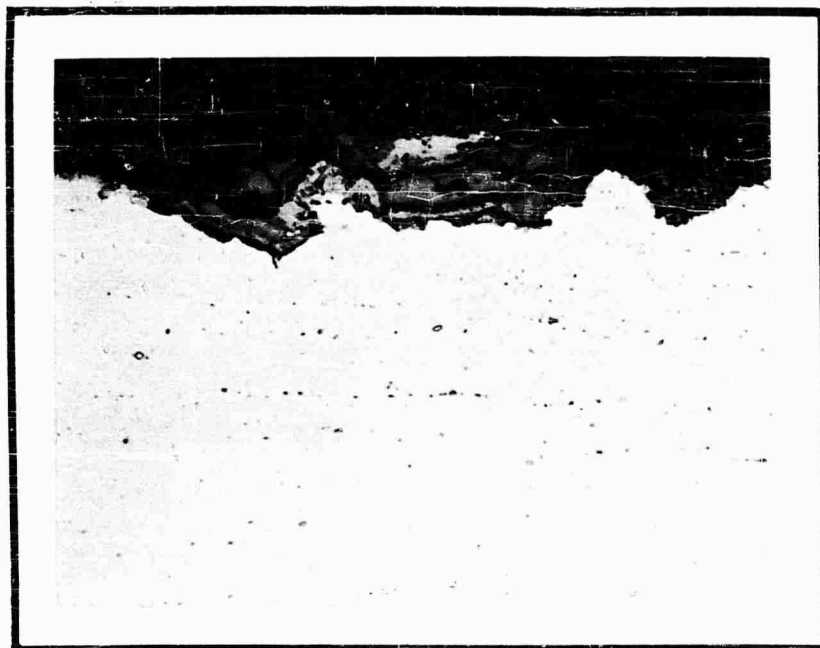
M-1226

600X

**Nickel 2 Before And After
Third Cesium Corrosion Test**

Fig. VII-14 (200 Hours At 770K)

Page 143



M-1224

600X

Stainless Steel 410-2
After Third Cesium Corrosion Test
(200 Hours At 770K)

Fig. VII-15

Page 144

F. Conclusions from Corrosion Tests

In reviewing the results of this series of corrosion tests, and the pertinent results of the emitter tests which affect the choice of materials, the following conclusions can be drawn:

- (1) In all cases, tungsten and molybdenum were excellent. At higher temperatures, however, the recrystallization effect must be noted, which can seriously reduce the structural strength of the material. Material which has recrystallized is less tolerant to severe loads, such as could be encountered in a vehicle launch. It may well be that an ion source should not be subjected to high temperature tests before use in an operating engine application.
- (2) Copper and aluminum are not recommended for use unless the surface is protected.
- (3) Metals and alloys should be free of oxide inclusions.
- (4) Platinum tolerated a cesium atmosphere when it was used as a bonding agent for a high-temperature emitter. In a separate corrosion test, however, a severe weight loss was suffered which may have been due to an extraneous oxidation effect. Definite conclusions, therefore cannot be drawn without further tests. Nickel and stainless steel 410 are in a similar category. It should be noted, however, that nickel, stainless steel, and commercial Microbrazed were used in emitter tests without difficulty (as components of the fuel system) where the temperature did not exceed 600°K. Components were, of course, thoroughly cleaned before use.
- (5) Aluminum oxide appears to be suitable for a cesium atmosphere up to 770K. Normal precautions to prevent cesium deposition on the surface necessarily are required when used as an electrical insulator.
- (6) The tests conducted to date are not considered to be final; further tests are recommended. The difficulty of conducting such tests has been demonstrated (due to the extreme reactivity of cesium, particularly at the higher temperatures) therefore the following procedure is suggested:
 - (a) In tests of individual materials, frozen cesium is placed in a container (tube) made of the material which is being evaluated. The tube is then forged closed (or welded closed if possible) in a vacuum or oxygen-free inert atmosphere. The tube should then be held at temperature for a given length of time in an oxygen-free inert atmosphere furnace.

- (b) To determine the effect of cross-contamination, specimens of all materials (which are to be used in the same fuel and emitter system) should be placed in a container which is not affected by cesium(e.g., tungsten and molybdenum are suitable), then, as described in Item (a) above, loaded with cesium, sealed, and tested.
- (c) Data acquired should include weight change, photomicrographic results, and x-ray diffraction studies.

VIII. CESIUM GENERATION IN SITU

For an ultimate application in a long term space mission, it is desirable to develop a fuel system with a minimum of handling and storage problems.

As an initial approach, an experimental program to generate cesium from its salts is described in this section. The objective is to eliminate the necessity of handling liquid cesium, which requires careful loading and storage procedures, by generating cesium as it is required.

The results of the cesium chloride plus calcium reaction indicate that 70.2% by weight of cesium theoretically can be generated from the total weight of the initial ingredients. In an experiment with this combination, 39% of the theoretical recovery was obtained, or 62.5% of the initial total weight. Other cesium salt reactions with higher theoretical recoveries are cited and are recommended for further investigation.

Mr. W. Aker, chemist, conducted this phase of the investigations under the supervision of Dr. Petrick.

VIII. CESIUM GENERATION IN SITU

The use of cesium in its metallic form requires specialized handling techniques. The metal is shipped in glass ampoules, usually sealed under a vacuum of about 10^{-3} mm Hg. For use in an ion source, it is necessary to thoroughly clean the ampoule, place in the system, evacuate, then break the ampoule and release the cesium metal under vacuum conditions. Although not particularly difficult, the procedure is somewhat time-consuming; but more important, the cesium must be handled with extreme care at all times. Cesium is reactive in air, rapidly forming oxides and subsequently a hydroxide; with other substances, the reaction can be violent.

In order to reduce the handling, loading, and storage problems with cesium metal, an experimental program has been undertaken to investigate the generation of cesium in situ. Various cesium salts, when properly mixed with a reductant and heated to a specified temperature, will release cesium as a product of the reaction. This is, in fact, the commercial method of producing cesium. If the other products have a suitably low vapor pressure, the cesium metal produced in the ion source "boiler" subsequently could be used as required in the ion source without contaminating effects. An endothermic reaction would be preferable, with cesium generated as needed by controlling the temperature of the mixture.

For application in space, the use of ampoules from which liquid cesium is released as necessary hardly appears to be desirable, particularly for long term missions. Storage in sealed metallic containers which also form the "boiler" is possible, but the problems of removal of oxygen at ground level and of container corrosion with long duration storage also can be drawbacks. In the laboratory, one unique method (74) proposed to alleviate some conditions of design is to freeze the cesium in liquid nitrogen, then break the ampoule and rapidly insert the solid cesium into the apparatus. The cesium reacts with oxygen from the air and with moisture to form a film of oxide and hydroxide on the surface; the coldness of the cesium metal absorbs the heat of reaction preventing rapid buildup of heat, stopping the reaction at the surface. The cesium is now contaminated, however, limiting its use.

A method of obtaining uncontaminated cesium vapor directly is to chemically reduce a cesium salt within the apparatus using a suitable reducing agent. Care must be made in the choice of materials to insure that (a) the vapor pressure of the cesium salt, reducing agent and reaction products (excepting cesium) are sufficiently low at operating temperature so that any contaminating influence would be negligible, (b) no oxygen or moisture is present, and (c) there is no deleterious effect on the apparatus materials (e.g., evolved hydrogen gas would

cause embrittlement of some materials). Should a relatively large amount of cesium vapor be needed over a short period of time, an exothermic reaction would be chosen. For a long term application, an endothermic reaction would permit the slow generation of cesium vapor controlled by duration of heating.

Several feasible chemical reactions are listed below:

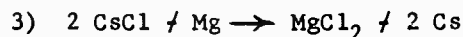


The reaction is endothermic with a calculated heat of formation of 59.7 K cal/mole. The ratio of cesium to initial reactant weight is approximately 7 to 9. An exothermic reaction with the same reactants



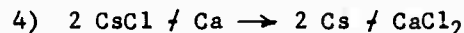
has a heat of formation of ca -30K cal/mole (heat data are not available for $\text{Cs}_3(\text{AlF}_6)$, hence this value was extrapolated from similar reactions with sodium and potassium). The ratio of cesium to initial reactant weight is 7 to 18.

A reduction reaction with magnesium and cesium chloride is given by



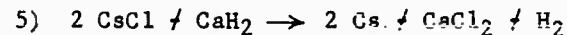
and is endothermic ($\Delta H_f = 53.6$ K cal/mole). The weight of cesium to initial reactants is approximately 6 to 8.

A calcium reduction of cesium chloride



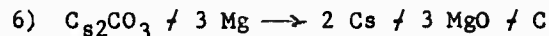
has a weight ratio of 3 to 5 and a heat of formation of -17.0 K cal/mole.

A similar reaction with calcium hydride as reductant as given below produces approximately the same weight ratio.



The weight ratio is 3 to 5 and the reaction is exothermic ($\Delta H_f = -62.1$), however the evolved hydrogen gas presents several problems (e.g., embrittlement of some metals) which may limit the use of this reaction.

An exothermic reaction with $\Delta H_f = -164.1$ K cal/mole using cesium carbonate and magnesium.



as reactants also is plausible, but the possibility of forming cesium oxide(s) during the reaction must be considered even though the amount would not appear to be immediately appreciable. All the above reactions should be conducted in a vacuum of at least 10^{-5} mm of Hg. The reactants are finely-ground powders intimately mixed by milling. Heat is applied according to the type of reaction calculated for the reactants. Properties of various reactants and products are given in TABLE VIII-A.

As an introductory experiment to establish feasibility, the cesium chloride plus calcium reaction was tested. As shown in TABLE VIII-B, theoretically 70.2% of the initial total reactant weight can be recovered as cesium.

Granular metallic calcium and cesium chloride powder were mixed and placed in a nickel crucible. The crucible was placed inside a vacuum chamber; 110 volt power leads were attached to the crucible to provide resistance heating. An inverted cold trap was suspended above the tube so that the open end of the nickel crucible was opposite and adjacent to the open end of the cold trap (but not within the cold trap). A thermocouple was attached to the crucible to measure temperature. The experiment was begun at 10^{-4} mm Hg by applying heat. At 620°C the reaction became exothermic and emitted vapors which coated the sides of the vacuum chamber and the surfaces of the cold trap. The temperature rose sharply to 650°C and held for a minute then dropped to 630°C, thus giving further indication of an exothermic reaction. Continued heating was applied until 820°C was reached; however, little or no further vaporization of Cs occurred. A thin blue deposit was coated on the sides of the bell jar, with thicker silvery deposits. (The bell jar is shown in Figure VIII-1) The deposit on the inside of the cold trap was blue-black with sections of silver. On the outside of the cold trap the deposit was colored violet-red. The inside of the nickel crucible was coated with a white material, the outside of the tube was silvery. The heat was turned off and the experiment held overnight at 5×10^{-2} mm Hg. White deposits were seen to have formed in the cold trap. The blue deposits on the sides of the vacuum chamber had become grayish. Moist air was then admitted slowly into the vacuum chamber causing the silver deposits to turn black-brown and then to turn white. Puffs of white smoke were emitted from the cold trap as the cesium reacted with the moist air.

The initial experiment described above indicated that the reaction occurred as predicted, therefore a second cesium generation experiment was undertaken using the same reactants with the aim of measuring the amount of cesium generated. The apparatus was adjusted so the nickel crucible extended into the cold trap to obtain complete recovery. During the evacuation process the vacuum chamber was alternately flushed three times with argon gas and evacuated to eliminate air.

The reaction started at 630°C; this was seen as a blue deposit in the cold trap. Vacuum at this time was 0.9×10^{-4} mm Hg. The coating became thicker and more metallic-appearing as the heating

TABLE VIII-A
PHYSICAL PROPERTIES
OF REACTANTS AND PRODUCTS CONSIDERED
FOR CESIUM GENERATION STUDY

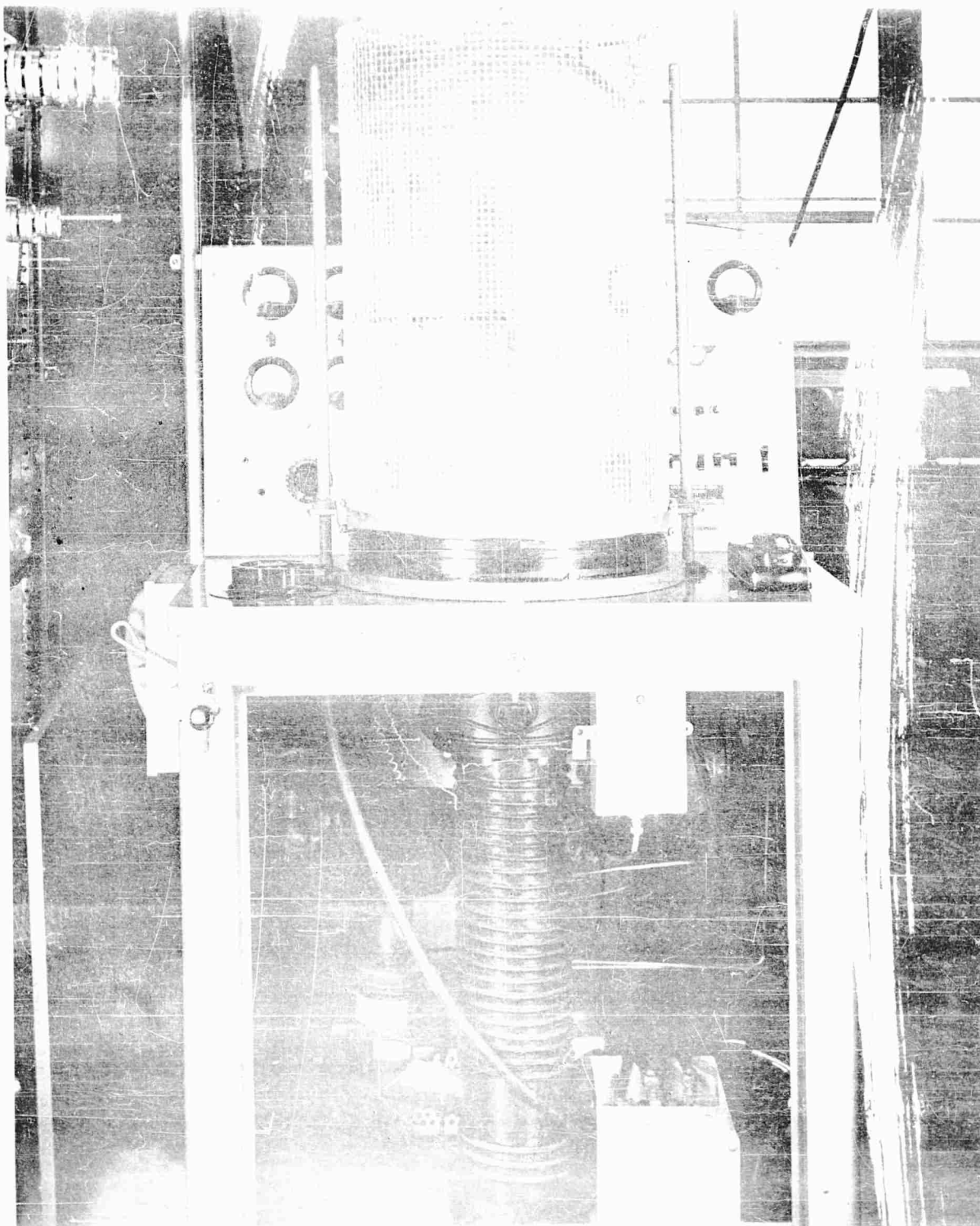
<u>Material</u>	<u>Symbol</u>	<u>Mole Wt.</u>	<u>(°C) Mp</u>	<u>(°C) Bp</u>	<u>g/cc Sp. Gr.</u>
Cesium	Cs	132.91	28.5	670	1.873
Cesium Chloride	CsCl	168.37	646	1290	3.97
Cesium Carbonate	Cs ₂ CO ₃	325.83	.610	---	----
Cesium Fluoride	CsF	151.91	684	1250	3.586
Aluminum	Al	26.97	659.7	2057	2.702
Aluminum Fluoride	AlF ₃	83.97	1040	---	3.07
Magnesium	Mg	24.32	651	1107	1.74
Magnesium Chloride	MgCl ₂	95.23	708	1412	2.316
Magnesium Oxide	MgO	40.32	2800	---	3.58
Calcium	Ca	40.08	842-8	1240	1.55
Calcium Chloride	CaCl ₂	110.99	772	>1600	2.512
Calcium Hydride	CaH ₂	42.10	ca600	---	1.7
Carbon (amorphous)	C	12.01	2550	---	4.78

TABLE VIII-B

REACTANTS AND PRODUCTS FOR CESIUM CHLORIDE - CALCIUM REACTION

					Theoretical	
			Equiv. Wts.	Wt. Percent of		
			To Form	Cesium to Total		
			2.5 g Cs	Reactant Weight		
Symbol	Molecular Weight	Number of Moles	Formula Weight			
Reactants						
Cesium Chloride	CsCl	2	336.74	3.37		
Calcium	Ca	1	40.08	.42*		
Products						
Calcium Chloride	CaCl ₂	1	110.98	1.11		
Cesium	Cs	2	265.81	2.66	70.2%	

* Slight excess of calcium used.



Vacuum Chamber for Cesium Generation Experiments

FIGURE VIII-1

continued. Heat was applied until the temperature reached 915°C at which point the heating process was stopped and the crucible was permitted to cool. The experiment was held 17 hours at 0.2mm Hg vacuum.

All of the deposit remained inside the cold trap; none was visible elsewhere in the apparatus. Seventeen hours after the apparatus was cool, a broad band of gray appeared three-fourths of the way up the inverted cold trap. The rest of the deposit maintained a silver color. Moist air was admitted to the vacuum chamber in small increments. The gray portion of this deposit gradually turned white; the silver portion gradually turned brown, then yellow and orange-red. After the vacuum chamber reached atmospheric pressure, the cold trap was removed and inspected. Continuous rings of deposits were found inside the cold trap. Starting from the open end and progressing to the closed end of the trap, the rings were colored white (deliquescent), blue, gray, orange, gray, blue, orange, gray, gray-white with orange tint, gray, blue, gray and at the closed end a combination of gray-blue-brown and orange. The various hues of the cesium oxides are given in TABLE VIII-C. The nickel crucible was removed and found to contain gray-white and gray deposits.

The cold trap was permitted to stand in the open air (very humid day with rain and fog). The deposit, as water was picked up, became white, peeled from the sides of the cold trap and fell to the bottom. Within 6 hours all of the solid material became liquid. This liquid, cesium hydroxide solution, was washed into a volumetric flask and made to 1000 cc. Aliquots of the liquid were then titrated versus a primary standard acid (potassium acid phthalate) to determine the amount of cesium present. Titrations found 2.358 grams of cesium actually deposited from the predicted 2.66 grams shown in TABLE VIII-B. The efficiency of the reaction therefore was 89%. In terms of cesium generated to initial reactant weight, the ratio was 62.5%.

The next logical experiment would be to construct an apparatus to recover cesium in the metallic form and measure the efficiency of the reaction. In addition, the other cesium salts previously cited also should be investigated. However, for a more pertinent immediate experiment, the reduction reaction should be tested as the fuel supply in an ion source to establish feasibility of this unique concept.

TABLE VIII-C
THE COLORS OF CESIUM OXIDES

<u>Compound</u>	<u>Oxygen/Cesium Ratio</u>	<u>Cesium Valence</u>	<u>Color</u>
Cs ₂ O - mono	$\frac{1}{2}$	+ 1	or.-red cr.
Cs ₂ O ₂ - per	1	+ 2	pa.-yel.need.
Cs ₂ O ₃ - tri (sesqui)	$\frac{3}{2}$	+ 3	cub.choc.br.cr.
CsO ₂ - super	2	+ 4	yel. cr.
CsOH	1	+ 1	col.-yelsh.v.deliq.

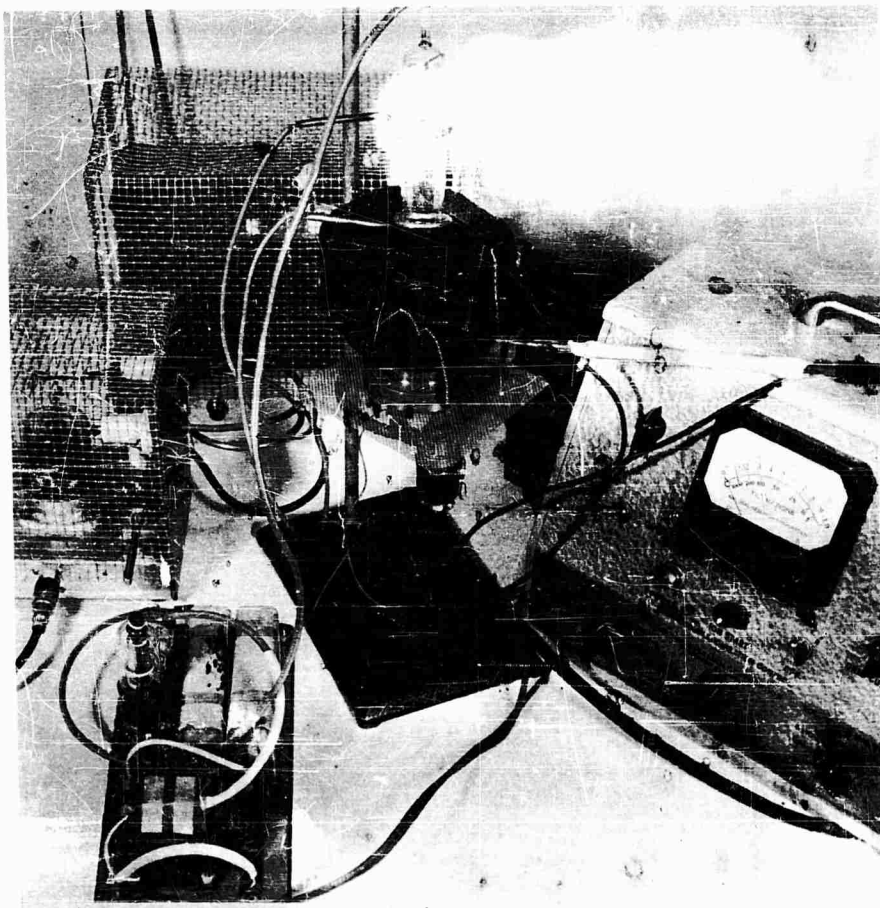
IX. THE RF ION SOURCE APPARATUS

A brief description is given of the apparatus proposed for experiments on RF ionization. Dr. O. K. Husmann supervised the analytical design, with Mr. Wm. Smith responsible for the mechanical design.

IX. THE RF ION SOURCE APPARATUS

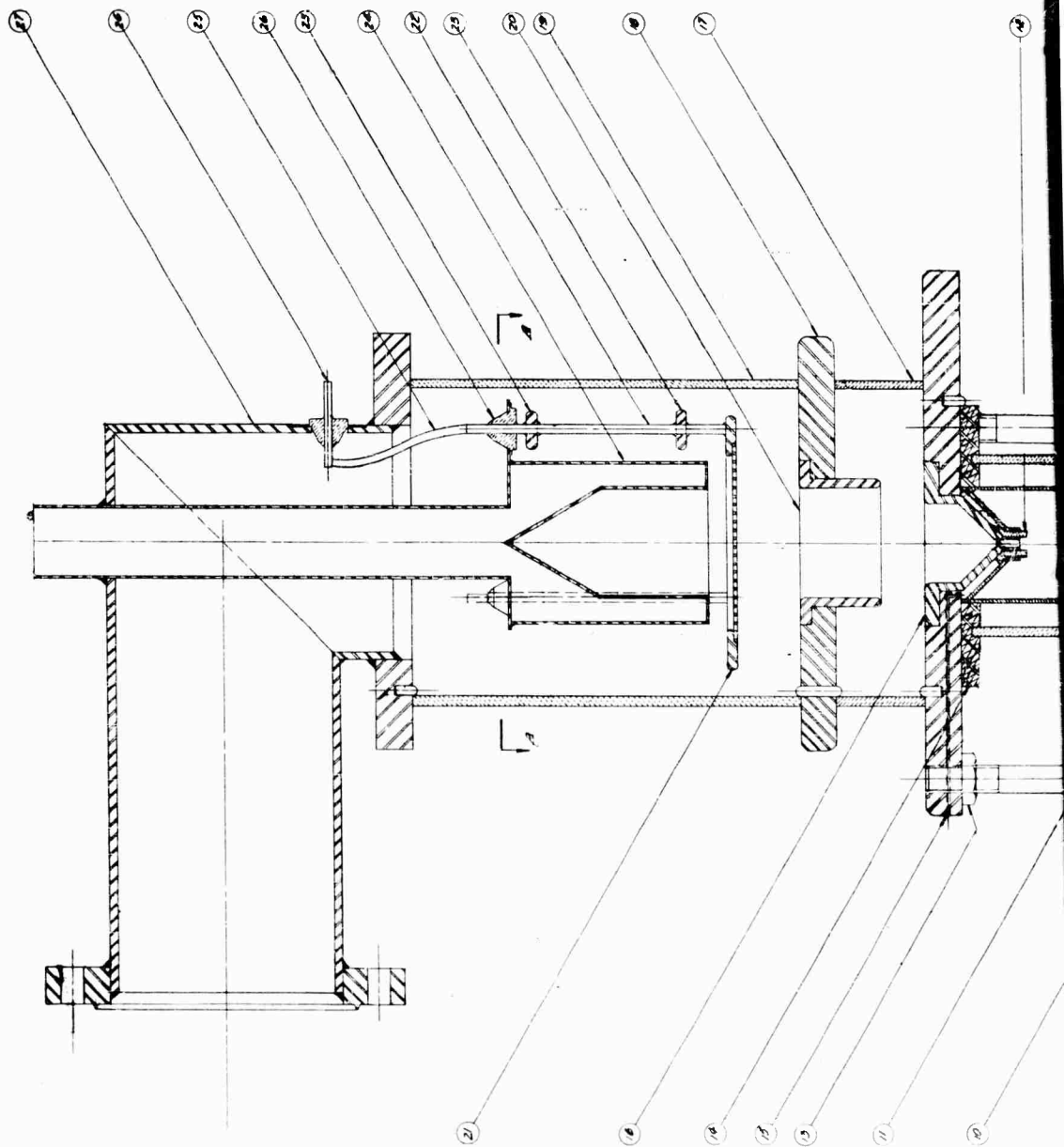
A brief description of the RF ion source was presented previously in Section II-B of this report. Figure IX-1 shows a hydrogen ion source which was set up prior to this program in the manner of Moak, et al (l.c.), to confirm previously published results. In considering an RF source for alkali metals, a new design has been formulated, using in part the techniques described by Reifenschweiler (l.c.) and, in particular, the ion condenser described by Neuert (l.c.). The experimental device is shown in Figure IX-2. The fuel is stored in the lower portion of the Pyrex plasma tube 8, separated by an aperture from the plasma tube. (The underlined numbers in the text correspond to the detail numbers shown in Figure IX-2) An external supply of hot air contained within the heat shields 7 and 11 regulates the fuel temperature and thus the vapor pressure in the plasma tube. The RF ionization coil 10 surrounds the tube and the heat shield. The ion-focusing electrode 16 and the extraction channel are located at the top of the plasma tube. Electrodes 16 and 20 form the ion condenser, the components of which are easily modified. The extraction channel is surrounded by a quartz tube 12, and is relatively large in diameter because with the low gas pressures the loss by diffusion is relatively small. The ratio of ions to neutrals should be correspondingly large. The accelerator electrode 20 is insulated by Pyrex 17 from the focusing electrode. The ion beam is collected in a Faraday cage contained within the cold trap 24. A grid 21 to suppress secondary electron emission from the Faraday cage is positioned between the accelerator electrode and the Faraday cage. The large elbow at the top of the apparatus is connected to the vacuum pumping system.

The glass portion of the apparatus has been constructed, but further procurement during this first contract period was suspended due to primary emphasis on the surface ionization studies. It should be noted that ion deflection in the ion lens is independent of the mass; therefore, the same lens system can be used for various types of fuels.

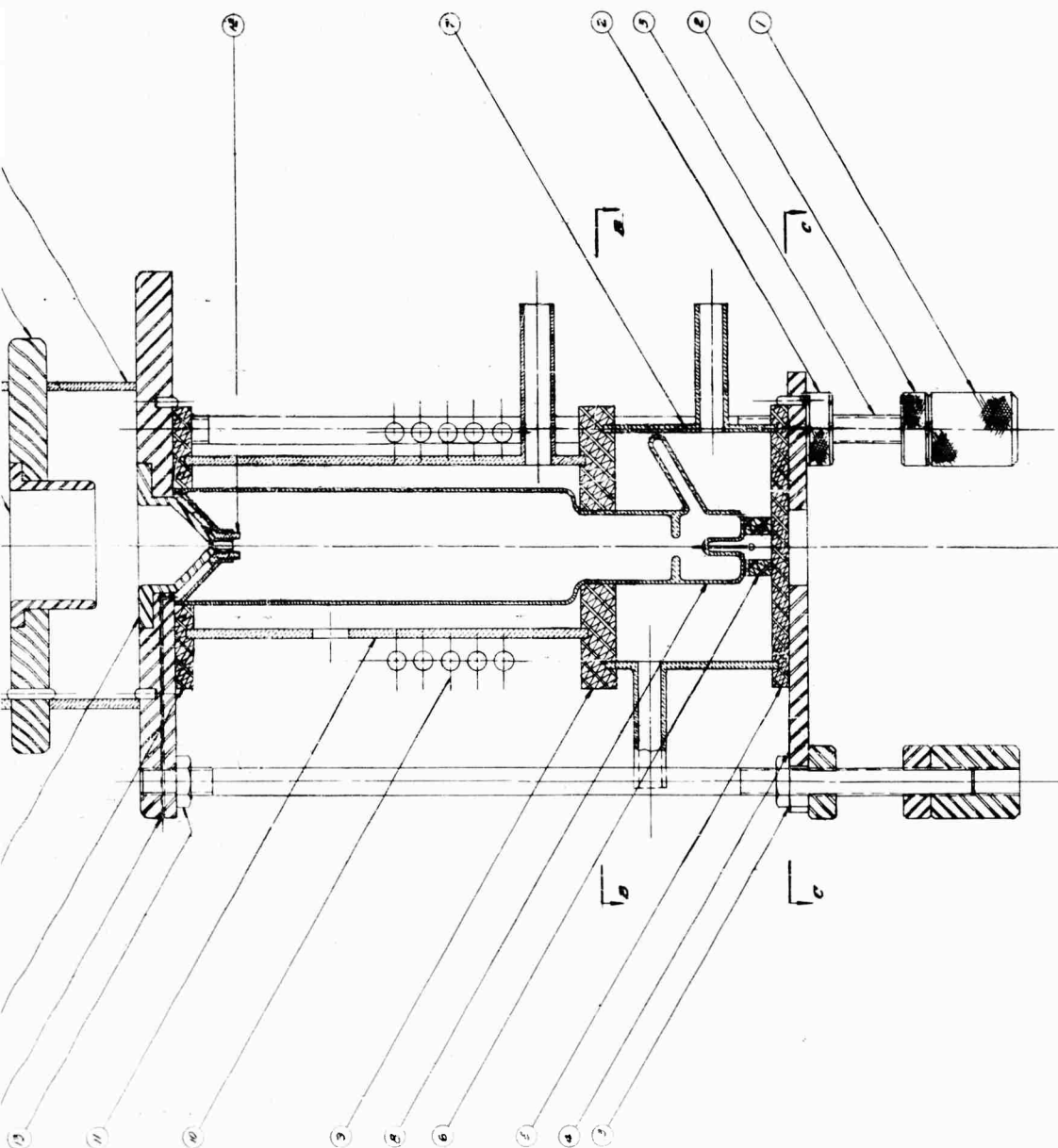


RF Hydrogen Ion Source in the Manner of Moak, et.al.

FIGURE IX-1



1



RF ION SOURCE

2

X. THE PLASMA ARC SOURCE

The discussion of the plasma arc as an ion source presented in this section was prepared by Dr. C. Burnett, Physics Department, Pennsylvania State University.

X. THE PLASMA ARC SOURCE, PROPOSED EXPERIMENTS

In the original scope of work statement for this program, it had been proposed to conduct cesium-seeding experiments in the existing plasma-arc rig, with the objective of obtaining data for comparison with the charge exchange (contact) and RF ion sources. In Section II-C of the present report, the extensive efforts by AEC Laboratories on plasma sources has been discussed, and some of their results have been presented. In view of the difficult diagnostics problem and the questionable data which would be obtained using our existing rig, it was judged unwise to divert effort from our main problem (i.e., charge exchange ionization) to accomplish the plasma seeding experiments. For that reason the plasma work in this program has been devoted to a study of diagnostic techniques and of the specialized experimental devices which could provide acceptable data. The large current densities obtainable in plasma devices have already been cited in Section II-C, indicating that further experimental investigations on plasma sources would be warranted although not proposed in the present program.

A flexible experimental device would be of most value, since the various features suggested by existing arcs might be compared. A complete study is clearly a major undertaking, but it is recommended that the source be designed to allow for some changes in electrode geometry and magnetic field configuration. The following indicate the types of arcs considered in the order of their current interest.

- A. Thermionic or self-heated hollow cathode with mirror-type fields and cathode extraction; high arc current.
- B. Source A modified for Duoplasmatron operation and anode extraction.
- C. Source A with uniform magnetic field and cyclotron extraction.

A. Diagnostics

The evaluation of an arc ion source and the extraction procedure should be carried out using known techniques in plasma study and ion optics. Particular attention should be given to comparing the results of operation with cesium vapor with the results of the charge exchange process using a hot tungsten plate. However, an arc source might be expected to operate with practically the same efficiency using other elements (fuels) without the possible difficulties associated with the chemical activity of cesium.

A convenient and dependable plasma diagnostic to be used in studying the arc is optical spectroscopy. Provided the ion density exceeds about $10^{16}/\text{cm}^3$, kinetic equilibrium can be assumed and the Saha equation, relating the ion and neutral densities with the "plasma temperature" is applicable (Ref. 54). The subject of spectroscopic diagnostics has been recently reviewed by Margenau and Lewis. The following equations have been taken from that review (Ref. 55). The Saha equation is written

$$\frac{n_i n_e}{n_0} = \frac{2 z_i}{z_0} \frac{(2\pi m_e kT)^{3/2}}{h^3} \exp - \frac{(X - \Delta X)}{kT} \quad (\text{Eq. X-1})$$

where z_0 and z_i are the partition functions for neutral atoms and ions and n_0 and n_i for their concentrations. Since the Saha equation involves both temperature and electron density, it is desirable to get an independent measure of one of these quantities. Electron densities have classically been determined from the Stark profiles of hydrogen-like spectra. First-order Stark lines are generally used with conditions of rather high density ($10^{16}/\text{cm}^3$) in order to minimize other effects which complicate the theory. For the Balmer line $H\beta$, Margenau writes (Ref. 56)

$$w_{1/2} \approx 7.8 r_2 (2n)^{2/3} \quad (\text{Eq. X-2})$$

where $r_2 = 10.35$ for $H\beta$.

Recent experimental studies have been made which utilized these and additional phenomena. In particular, Wulf has studied an arc discharge in helium using first and second order Stark effects and the Inglis-Teller "Drowning" of high energy states (Ref. 57). Davies has made a study of cesium discharges in a magnetic field (Ref. 58) making particular use of the distribution in intensity in the 6p recombination radiation as suggested by Moehler (Ref. 59) to determine the distribution of electron velocities in the discharge.

Absolute line intensities may also be used to obtain a relationship between radiator density and temperature provided the plasma is optically thin and the oscillator strengths, f , are known.

$$I = \frac{2\pi e^2 h f n^2}{m_e \lambda^3} n_0 \exp - \left(\frac{E_n - E_0}{kT} \right) \quad (\text{Eq. X-3})$$

A temperature can also be derived from the relative intensity of lines in a spectral series such as the Balmer series of hydrogen.

$$\frac{I_n}{I_{n'}} = \frac{n^2}{n'^2} = \frac{\sum n}{\sum n'} \frac{A_n}{A_{n'}} \exp \frac{E_{n'} - E_n}{kT} \quad (\text{Eq. X-4})$$

The use of a small amount of hydrogen as a spectroscopic probe is desirable. However, transition probabilities for cesium are also known (Ref. 60).

The Saha equation would be useful with the cesium spectrum or it might be applied to observations on the spectrum of helium or argon used as a carrier gas in the discharge. Argon would be of additional use since transition probabilities in A 1 and A 11 have recently been determined by Olsen (Ref. 61). Relative measurements on the Cs 1 and Cs 11 spectrum of interest can be made as a function of position in the arc and as a function of changes in applied voltage, rate of cesium injection, carrier gas pressure, etc. A particularly useful measurement which can be made when a small amount of cesium is added to a plasma of helium ions is the decrease of intensity of the helium ion light ($\lambda 4686 \text{ \AA}$). The measurement is directly related to the number of helium ions which must decrease as the electron density is increased by the ionization of cesium. This is because the Saha equation refers to the partial pressures of a given ion and all of the electrons. Incidentally, the Saha equation predicts that at a density of $10^{16}/\text{cm}^3$ and a temperature of 5000°K the cesium will be more than 90% ionized.

The use of a Langmuir probe is also a standard technique in dense plasmas. Several circumstances indicate, however, that this diagnostic may be somewhat unreliable. There is always some effect of a probe on the behavior of the discharge, and its use in a magnetic field is more difficult to interpret. Finally, the bombardment by cesium neutrals may give rise to spurious currents requiring corrections. In view of the precautionary remarks expressed by Loeb (Ref. 62) and by Francis (Ref. 63), it does not seem advisable to depend entirely on probe measurements, although some use should be made of this technique. Following the notation of Bohm, Burhop, and Massey, the expressions of electron temperature T_e and positive ion density n_0 are:

$$T_e = \left[\frac{d}{dv} \ln (-J - J_f) \right]^{-1} \quad (\text{Eq. X-5})$$

$$J_f = 0.4 n_0 \sqrt{\frac{2 k T_e}{m_f}} A \quad (\text{Eq. X-6})$$

where J_f is the ion saturation current, V is the probe voltage, and A is the probe area. The validity of the expression for T_e in a magnetic field is somewhat questionable, but the ion saturation current is expected to be a good diagnostic if the probe dimensions are small compared to the Larmor radius for the ions.

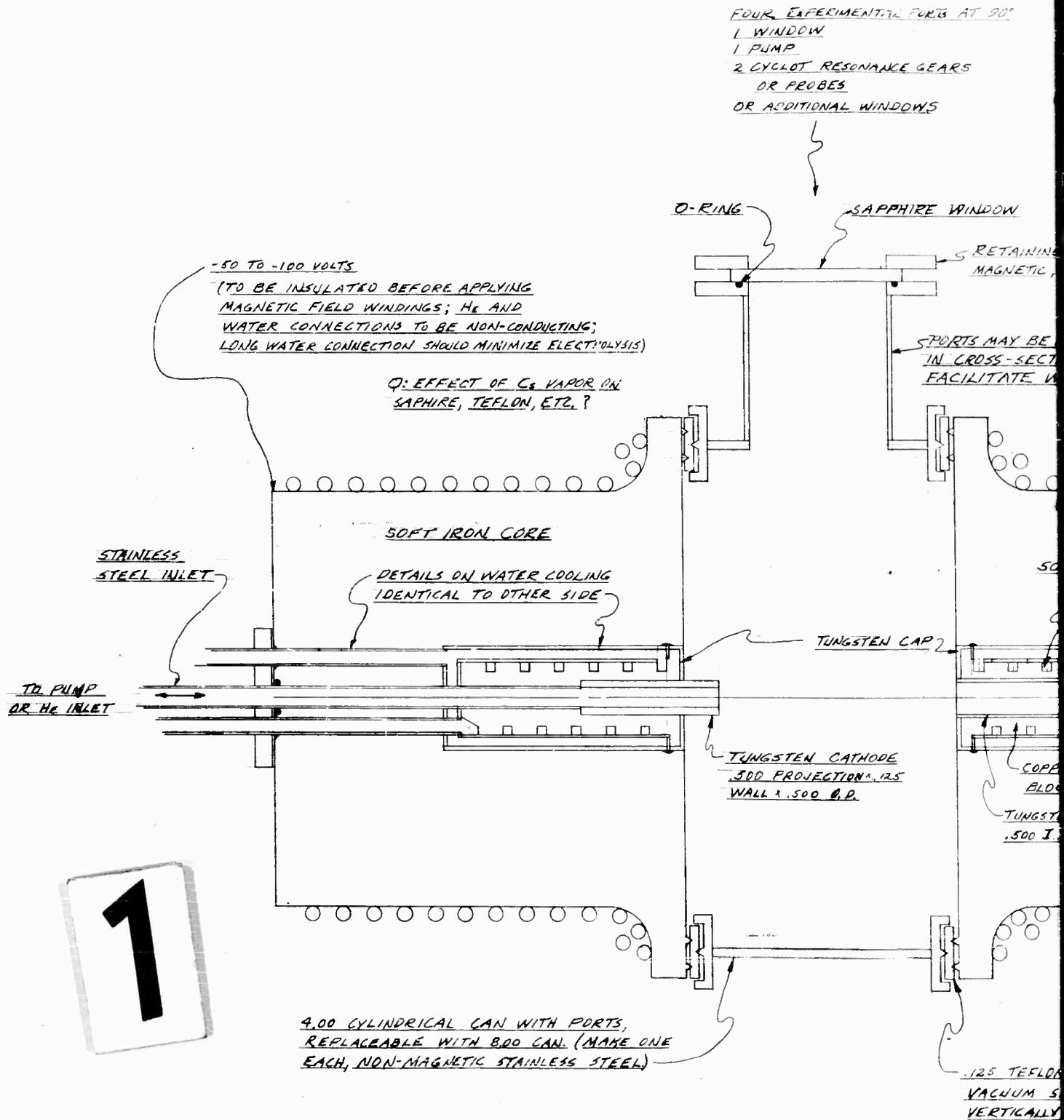
Optical refractivity measurements have been suggested by Alpher and White for electric discharges (Ref. 64). In any major plasma study such a possibility should be exploited. However, the optical problems involved with this diagnostic are sufficient to postpone its use for the immediate future.

B. Ion Extraction

The success of any ion source, regardless of its production of large ion densities, hinges on the ability to extract large ion currents. A straightforward testing procedure here is the collection of the ions in a Faraday cage after extraction and analyzing magnetically in a manner similar to that accomplished in the previously-discussed charge exchange experiment. A particular difficulty to be avoided in the extraction procedure is the production of electrons and possibly a plasma in the accelerating region. It is expected that the electrons, but probably not the negative ions, can be magnetically deflected from the accelerating field. It may thus develop that an upper limit on the escape of neutrals from the source must be imposed in order to guarantee the success of ion extraction.

Those devices relying on an accelerating grid may be experimentally of interest, but will probably have to be ruled out on the basis of long-term reliability. The filament type cathode suggested in Source A may suffer in this regard also. However, the use of D.C. filament power may prevent a considerable amount of sputtering due to the azimuthal magnetic field produced about each conductor. Also, the alignment of the filaments parallel to the exterior magnetic field should eliminate the usual sagging of such a filament. The particular merit of this type of cathode is based on the supposition that an independently-heated cathode will produce a more stable arc, and that a larger ion current may result from the ion backstreaming caused by the existence in the plasma of a fraction of the impressed arc field. This accelerates the ions toward the cathode sheath from a region which is space-charge-neutralized.

A final possibility for ion extraction and acceleration is the classic cyclotron resonance phenomenon for single ions. The sketch of a suggested apparatus is shown in Figure X-1. Such a process lends itself nicely to the selective acceleration of a particular type of ion in a magnetic field. It is expected that an electric field oscillating at the cyclotron frequency for cesium ions (about 50 kc for 5000 gauss) and directed at right angles to the magnetic field can penetrate the plasma sufficiently to extract a small fraction of cesium ions present in a plasma of another carrier gas. After being removed from the plasma column and its partial shielding effect, the ions will be less subject to recombination and can be given further energy for propulsion purposes by continued cyclotron acceleration, which is possible if the region is a reasonably high vacuum. This is also one of the attractive features of the DCX type arc. It is clear that the accelerating frequency ought to be comparable to or greater than the collision frequency of the ions. The latter may be estimated from the expression derived by Spitzer (Ref. 65). The frequency of 50 kc corresponds to a density of $10^{12}/\text{cm}^3$, roughly comparable to that surrounding the DCX arc. The period of oscillation will have to be somewhat less than the transit time in the arc if several accelerations are to be made, which



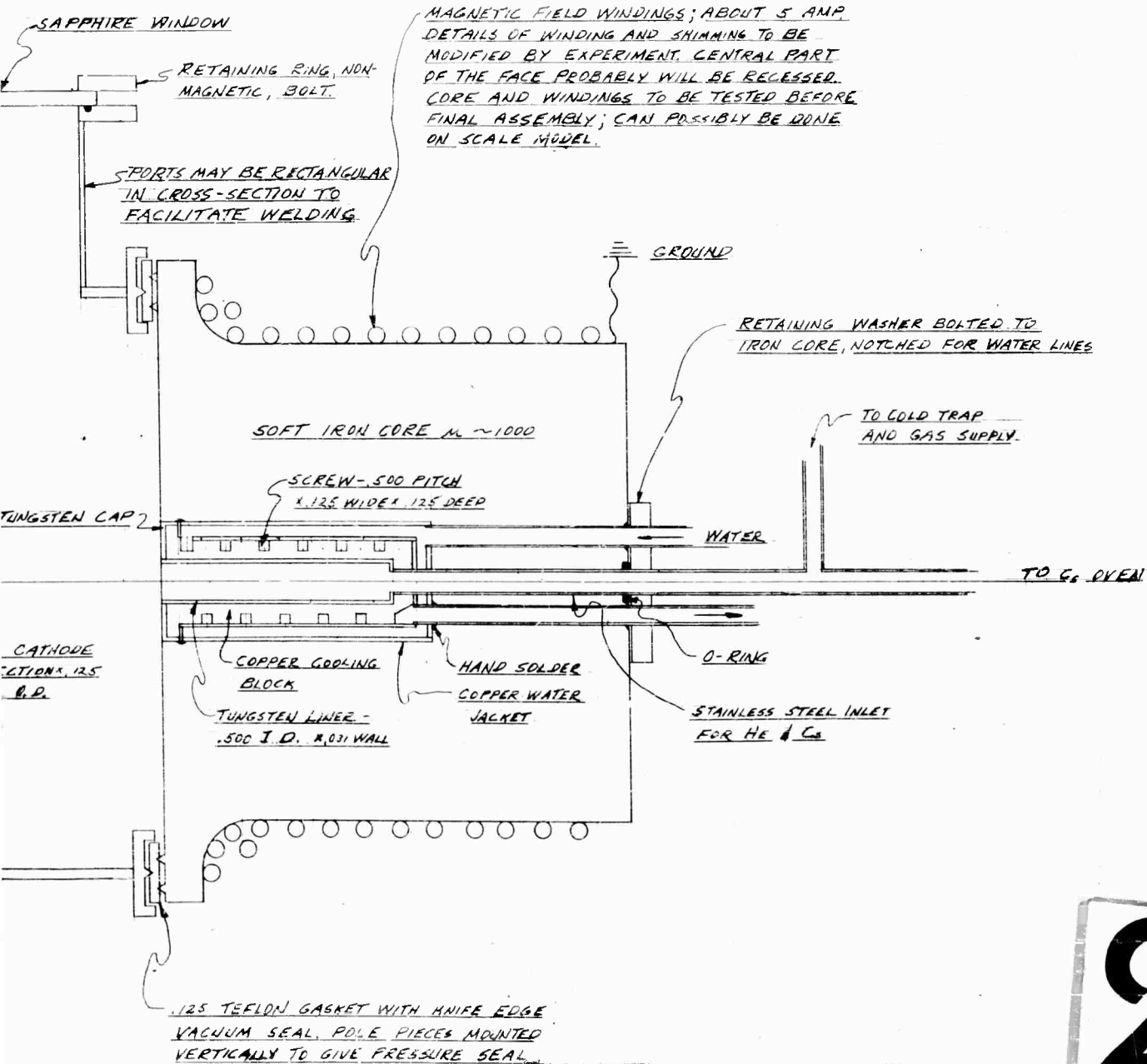
1

EXPERIMENTAL PORTS AT 90°

RESONANCE GEARS

GES

NAL WINDOWS



2

may require an arc on the order of one meter in length. Also, a 10 kev cesium ion in a magnetic field of 5000 gauss would travel in a 30 cm radius arc. Apparently, this would be a rather large device, although the magnetic field and frequency can be increased somewhat in order to decrease the space required. There will undoubtedly be considerable power transferred to the plasma electrons by the cyclotron acceleration field and the possibility of extracting a large ion current may be rather remote. The unique feature allowing very large final ion velocities using relatively small accelerating fields is believed to merit further theoretical and possibly experimental study, although no further studies are anticipated in the present program.

XI. RESULTS AND RECOMMENDATIONS

A brief summary of the results and recommendations for continued investigations are presented in this section.

XI. RESULTS AND RECOMMENDATIONS

The results of each phase of the investigation have been presented at the conclusion of each section in the present report. It is pertinent, however, to summarize these results briefly and to indicate the areas in which continued research is contemplated.

- a) Diffusion flow rate experiments using inert gases with emitters of (1) porous sintered tungsten (2) molybdenum screen and (3) punched platinum screen have provided data on the mechanism of flow and dependence on plate temperature. At high temperature operation with porous emitters, an aging effect is observed which appears to be a function of sintering temperature.
- b) Ionization experiments provided excellent correlation of measured ion current with predicted values based on diffusion flow data. An exception was in the case of clogging of the emitter from other causes. The effect of surface diffusion flow has been shown to be negligible for the conditions of the tests. A mass spectrometer was constructed and is scheduled for use in further experiments. Continued experiments are proposed, using both finer screens and also emitters made of spherical powders in the 0.1 to 10.0 μ range, including tungsten and rhenium.
- c) From a theoretical standpoint, the charge exchange (contact) emitter can provide a high current density with excellent ionization efficiency. Theoretical considerations reported herein have included diffusion flow rates, atom and ion lifetimes, emitter temperature effects, and other means of ionization such as RF and plasma techniques.
- d) Various methods of bonding the emitter into a holder have been investigated to prevent by-pass flow of fuel vapor around the emitter. Best success to date has been with a platinum brazing technique. The use of other high-temperature braze materials such as niobium and iridium is recommended for further bonding experiments.
- e) Corrosion tests of various materials in cesium indicate a high-temperature long-term suitability of such materials as tungsten, molybdenum, and aluminum oxide. Numerous emitters, structural, and insulation materials were tested. A cross-contamination effect between several materials was noted. Continued testing is recommended at higher temperatures.
- f) Cesium was successfully generated from cesium chloride salt with a recovery of 39% of theoretical. Other reactions are cited and it is proposed to evaluate this unique technique

in an ion source as a means of minimizing the fuel handling and storage problem.

REFERENCES

1. "Supplemental Information for Proposed Joint ARPA-ONR Program on Compact Charge-Exchange Ionization." CW Research Division Report submitted to ONR, Power Branch.
2. A. Eucken, Lehrbuch der Chemischen Physik Volume II, 2.p1320. 1944.
3. J. Zemel, J. Chem. Phys. 28. 410. 1958.
4. S. Datz and E. H. Taylor, J. Chem. Phys. 25. 389. 1956 and J. Chem. Phys. 23. 1711. 1955.
5. T. J. Killian, Phys. Rev. 27. 578. 1926.
6. J. B. Taylor and I. Langmuir, Phys. Rev. 44. 423. 1933.
7. M. J. Copley and T. E. Phipps, Phys. Rev. 48. 960. 1935.
8. P. Keuk and L. B. Loeb, Rev. Sci. Instr. 4.486-490. 1933.
9. J. B. Taylor and I. Langmuir, Phys. Rev. 51. 753. 1937.
10. M. Nordmeyer, Ann. d. Phys. 16. 697. 1933.
11. J. B. Koch, Z.f. Phys. 100. 669. 1936.
12. E. Stuhlinger, "Electrical Propulsion Systems for Space Ships with Nuclear Power Source." J. Astronautics, 1955. 149-152 and 11-14. 1956.
13. M. J. Willinsky and E. C. Orr, "Project Snooper," ARS Preprint 419-57. April 1957.
14. D. B. Langmuir, Feb. 17, 1958, ERL-116, ERL-119 and ERL-121.
15. R. H. Boden, R 1455, May 1955, R-645.
16. A. T. Forrester and R. C. Speiser, Conference on Ion and Plasma Research, 30 September - 2 October 1958.
17. F. L. Hughes, H. Levinstein, and R. Kaplan, Phys. Rev. 113. 1023. 1959.
18. E. Mueller, Z.f. Phys. 108. 668. 1938, and Z.f. Phys. 120. 261. 1943.
19. F. Knauer, Z.f. Phys. 125. 278. 1948 and 126. 319. 1949.
20. T. H. Bull and J. G. Marshall, Nature, London, 167. 478, 1951.
21. R. D. Evans, Proc. Roy. Soc. A 139. 604, 1932.
22. J. A. Becker, Ann. N.Y. Acad. Sci. 58. 723-740, 1954.
23. M. Benjamin and R. O. Jenkins, Proc. Roy. Soc. Ldn. A 180. 225. 1942.
24. L. Frank, Trans. Faraday Soc. 32. 1003-14. 1936.
25. R. W. Ditchburn and J. C. Gilmour, Rev. Mod. Phys. 13. 310. 1941.
26. A. Eucken, Metallwirtschaft 15. 27. 1936.
27. E. Stuhlinger and R. Seitz, Astronautics, V4, No. 11, p.37.
28. G. K. Wehner, J. Appl. Phys. 30. 1762. 1959, also Phys. Rev. 108. 35-45. 1957, also Advances in Electronics and Electron Physics, Vol. VII. 239-298. 1955.
29. D. T. Goldman et. al., Phys. Rev. Vol. No. 2, 1958 July.
30. R. Bruenne, Z.f. Phys. 147. 165-183. 1957.
31. P. M. Waters, Phys. Rev. 109. 1466. 1958.
32. J. R. Pierce, J. Appl. Phys. 11. 548-54. 1940.
33. M. E. Hines, Proc. IRE 40. 60. 1952.
34. T. VanDuzer and G. R. Brewer, J. Appl. Phys. 30. 291. 1959.
35. R. Fox, ARS 927-59.
36. J. B. Langmuir and R. B. Cooper ARS 929-59.

UNCLASSIFIED

UNCLASSIFIED